Stony Brook University

A first-principles study of structural, electronic and optical properties of GaN, ZnO and $(GaN)_{1-x}(ZnO)_x$

A Dissertation presented

by

Jian Liu

to

The Graduate School

in Partial Fulfillment of the

Requirements

for the Degree of

Doctor of Philosophy

in

Physics

Stony Brook University

December 2015

Stony Brook University

The Graduate School

Jian Liu

We, the dissertation committee for the above candidate for the

Doctor of Philosophy degree, hereby recommend

acceptance of this dissertation

Philip B. Allen - Dissertation Advisor
Professor, Department of Physics and Astronomy

Maria V. Fernández-Serra - Chairperson of Defense
Associate Professor, Department of Physics and Astronomy

Matthew Dawber
Associate Professor, Department of Physics and Astronomy

Mark S. Hybertsen
Group Leader (Theory and Computation)
Center for Functional Nanomaterials, Brookhaven National Laboratory

This dissertation is accepted by the Graduate School

Charles Taber
Dean of the Graduate School

Abstract of the Dissertation

A first-principles study of structural, electronic and optical properties of GaN, ZnO and $(GaN)_{1-x}(ZnO)_x$

by

Jian Liu

Doctor of Philosophy

in

Physics

Stony Brook University

2015

The pseudobinary $(GaN)_{1-x}(ZnO)_x$ alloy is attractive for its high efficiency in photocatalytic water splitting[1]. Its reduced band gap is a main advantage for harvesting solar energy. Short-range order (SRO) dramatically affect the atomic and electronic structures due to the non-isovalent nature of the alloy. In this thesis, I perform Monte-Carlo simulations on a first-principles-based cluster-expansion model[2, 3, 4, 5] to show the existence of SRO in $(GaN)_{1-x}(ZnO)_x$ alloy. I also construct the special quasi-ordered structures to faithfully include SRO in a computationally affordable supercell. Subsequent density-functional theory (DFT) calculations reveal significant influence of SRO on the structural, electronic and optical properties of $(GaN)_{1-x}(ZnO)_x$ alloy. The short-range ordered alloys experience smaller lattice bowing as well as band gap bowing than the disordered alloys. The role of SRO in the band-gap reduction is dominated by the Zn3d-N2p repulsion. SRO inhibits the nearest-neighbor Zn-N pairs, which affects the strength of the Zn3d-N2p repulsion and consequently the top of the valence band.

Electronic structure method can now handle fairly large supercells (e.g., over 100 atoms). For the study of non-isovalent semiconductor alloys, a large supercell is generally favored in order to average out the fluctuation error due to the nite size of the supercell. As large structural relaxations are expected, DFT total energy and force calculations have the merit of rigor, but are computationally expensive. Therefore it is desirable to pre-relax the internal atomic positions in an economical way. In this thesis, the bond valence method[6] (BVM) and its application in $(GaN)_{1-x}(ZnO)_x$ alloy is studied. Particular attention is paid to the role of SRO. A physical interpretation based on atomic orbital interaction is proposed and examined by DFT calculations. Bond-length distribution and bond-angle variation are predicted by parameter-fitting BVM empirical correlations to reliable DFT-calculated structural data. The correlation between bond valence and bond stiffness is revealed. The concept of bond valence is extended into the modelling of an atomistic potential.

The pure end-member semiconductors of $(GaN)_{1-x}(ZnO)_x$ alloy, GaN and ZnO, have spontaneous polarizations comparable with those of ferroelectric materials. Nowadays spontaneous polarization can be predicted at the first-principles level[7]. However, pyroelectricity, namely the temperature dependence of the spontaneous polarization, has not been investigated at the first-principles level. In this thesis, I discuss the pyroelectric theory of Born[8] in detail. Through first-principles calculations, the primary pyroelectricity is calculated according to the anharmonic internal displacements of the Born effective charges on the cations and anions. While the primary (anharmonic internal displacement) pyroelectricity contributes the major part of the total pyroelectricity at low temperatures, the secondary (thermal expansion) pyroelectricity becomes comparable with the primary pyroelectricity at high temperatures. An efficient way of calculating third-order force constants at zone-center using the dynamical matrix is proposed.

In this thesis, I also include a chapter on a preliminary study of combining Allen-Heine-Cardona (AHC) theory with the Virtual Crystal Approximation (VCA) in order to obtain the temperature dependence of the band gap of isovalent semiconductor alloy $Ga_{1-x}In_xN$. I report on the structural, electronic and vibrational properties of the $Ga_{1-x}In_xN$ alloy from first-principles. I show that VCA ignores disorder effect and is therefore unable to describe the

broadening of the phonon spectra upon alloying. The role of electron-phonon interaction in the temperature dependence of the band gap is also studied for GaN, InN and their alloy $Ga_{1-x}In_xN$. The calculated zero-point motion renormalization and the fitted Varshni parameter over the entire composition range are discussed.

Table of Contents

Contents

List of Figures

List of Tables

Acknowledgements

This is possibly the most read, the most fun, and very likely the most understandable part of my thesis. So I would like to take this opportunity to express my deepest appreciation to those who have helped me walk through the most peaceful four years of my life.

I thank my thesis advisor, Prof. Philip B. Allen, for all the guidance he has devoted. I will always admire him for his profound knowledge in theoretical solid state physics. His rigor in research is one invaluable merit that I shall always follow in my future career. It is my great honor to have Phil as not only my advisor in academics, but also my mentor in life. I would forever remember the warmth of Thanksgiving that I embraced at 2013, the effort that Phil and his son Ben put in jump-starting my car battery on that cold winter afternoon, and the wonderful dinner Phil's wife Ellen treated. I thank Phil for making my PhD study a unique life experience which I could tell my son(s) and grandson(s) all about.

I thank Prof. Maria V. Fernández-Serra for the extensive guidance she provided from the perspective of a professional computational physicist. I could always find myself inspired by her energetic and productive attitudes toward research. Not to mention all the useful skills I have learned from her. I am also deeply grateful to her for providing me with the opportunity of enjoying an excellent atmosphere in her group. It is my great pleasure of having Marivi as my co-advisor.

I thank Prof. Matthew Dawber and Dr. Mark Hybertsen for serving on my thesis defense committee.

I thank my fellow graduate students, Adrián Soto, Simon Divilov and Daniel Elton for the fruitful discussions. I thank Dr. Luana Pedroza and Dr. Betül Pamuk for their guidance on SIESTA. I thank Dr. Li Li for his initiative instruction on the cluster expansion method. I thank Dr. Qiang Zhu for his patient instruction on the evolutionary algorithm. I thank the helpful discussions with Dr. Xiangfeng Zhou, Dr. Neerav Kharche and Dr. Sriram Ganeshan. Special thanks to Prof. Xiao Shen for his recommendation on a postdoc position at Vanderbilt University.

Finally, from the bottom of my heart, I thank my wife, Jia Yu, for having more faith in me than I have in myself, for loving my parents as her own,

and for loving me.

The research conducted in this thesis used computational resources (i) at the Center for Functional Nanomaterials (CFN), Brookhaven National Laboratory (BNL);(ii) at the Institute for Advanced Computational Science (IACS), Stony Brook University (SBU). Work at SBU was supported by US DOE Grant No. DE-FG02-08ER46550 (PBA) and DE-FG02-09ER16052 (MFS). Jian Liu was also sponsored by the China Scholarship Council (CSC).

Chapter 1

1 Background

1.1 $(GaN)_{1-x}(ZnO)_x$: Short-range Order

Relative to pure end-member materials, the non-isovalent pseudobinary semiconductor alloy $(GaN)_{1-x}(ZnO)_x$ shows improved efficiency as a photocatalyst in splitting water into hydrogen and oxygen under visible light illumination[1]. High efficiency is partly attributed to the band-gap reduction which can be tuned by varying the ZnO content x of the alloy. First-principles calculations show that including short-range order (SRO) could dramatically affect the band gaps of the heterovalent semiconductor alloys[9, 10]. Experiments on different $(GaN)_{1-x}(ZnO)_x$ samples also observe large variation in the band gaps, which could be attributed to the different degrees of SRO introduced in growing the samples. For example, the absorption edge shifts monotonically to longer wavelength with increasing x for samples synthesized by nitridation of nanocrystalline $ZnGa_2O_4$ and ZnO precursors[11], while a minimum gap at $x \sim 0.5$ is found for samples synthesized by mixing of GaN and ZnO powders at high pressure and high temperature[12]. Previous theoretical studies assume the $(GaN)_{1-x}(ZnO)_x$ alloy to be completely random, and use the Special Quasirandom Structure (SQS) method to construct supercells mimicking random alloys[13, 14, 15]. However, even for isovalent ternary nitride semiconductor alloys, neglecting SRO introduces non-negligible systematic errors[16]. The situation is compounded for the $(GaN)_{1-x}(ZnO)_x$ alloy whose heterovalent nature favors local charge neutrality and therefore valence-matched nearest-neighbor Ga-N and Zn-O pairs. The aim of this thesis is to construct DFT-affordable supercells whose structural correlations reflect the actual SRO at certain thermodynamic condition (x, T). This will allow us to study with a single DFT calculation the statistical average atomic, electronic and vibrational properties of the $(GaN)_{1-x}(ZnO)_x$ alloy.

1.2 $(GaN)_{1-x}(ZnO)_x$: Bond Valence Method

In order to fulfill the local charge neutrality, the substitutional SRO is accompanied with and compensated by the positional atomic deviation from the ideal lattice sites. Therefore it is imperative to study the large composition-, temperature- and SRO-dependent (x, T, Π) structural relaxations. The bond valence method (BVM) is widely adopted in solid state chemistry for various applications including prediction of the molecular geometry[17], construction of the atomistic potentials for perovskite oxides[18, 19], and calculations of the acidity constant pK_a[20, 21]. Its power in predicting the energetics for non-isovalent semiconductor alloys is recently demonstrated[22, 23]. In inorganic chemistry the BVM is commonly recognized as an empirical tool, the underlying physics of which is not widely discussed. For example, the fact that bond valence correlates strongly with bond length[17] indicates the connection between bond valence and bond-length-dependent transferable force constant[24]. Also the correlation between total energy and bond valence[17] is not fully understood yet. Brown[17] proposed a "more rigorous but less physical" analogy of the Kirchhoff circuit law which treated the bond valence network as a capacitive electric circuit. Burdett[25] derived an interpretation from a molecular orbital basis. There is also some similarity between the bond valence and the Mayer bond order[26]. In this thesis, a physical interpretation of BVM is discussed from the computational perspective. The underlying assumptions within BVM are revealed by DFT calculations on the non-isovalent semiconductor alloy $(GaN)_{1-x}(ZnO)_x$. The aim is a reliable prediction for bond-length distribution and bond-angle variation by parameter-fitting BVM empirical correlations to DFT-calculated structural data.

1.3 Pyroelectricity

Pyroelectricity, defined as the temperature dependence of the spontaneous polarization, is a fundamental and poorly understood property[27]. Among various applications, pyroelectric materials are widely used in thermal infrared (IR) detectors[28] for their sensitivity over a wide range of temperature. Among the non-ferroelectric pyroelectrics, wurtzite crystals exhibit

spontaneous polarization and pyroelectricity comparable with those of ferroelectric pyroelectrics, and are candidates for high-temperature IR detection because they do not lose pyroelectricity at the Curie temperature. Recent developments include the measurement of significant pyroelectricity of c-plane GaN at room temperature[29, 30]. Peng and Cohen[31] studied the origin of pyroelectricity in $LiNbO_3$ using molecular dynamics with a first-principles-based shell model potential. They found that the primary pyroelectric effect is the major part of the pyroelectricity, and comes from the anharmonic atomic displacement of participating ions carrying Born effective charges. This agrees with the estimate of Zook and Liu[32] that the effects of clamping are negligible for the ferroelectric pyroelectrics. However they estimate a more significant secondary effect for the non-ferroelectric wurtzite pyroelectrics. Nowadays spontaneous polarization can be predicted at the first-principles level[7], but corresponding theory for pyroelectricity seems not to exist. In this thesis I give a first-principles quasi-harmonic theory and calculation for pyroelectricity in wurtzite GaN and ZnO.

1.4 $Ga_{1-x}In_xN$: Electron-phonon Interaction

The $Ga_{1-x}In_xN$ alloy has attracted great interest due to its technological importance in optoelectronics and electronics. Direct generation of hydrogen by splitting water using solar energy has also been reported for the $Ga_{1-x}In_xN$ alloy[33]. The band gap of the $Ga_{1-x}In_xN$ alloy can be tuned to cover nearly the entire solar spectrum, from 0.8 eV (InN) to 3.5 eV (GaN), by varying the composition x. Many basic properties of the $Ga_{1-x}In_xN$ alloy are not well known due to the difficulty in growing high quality samples. The composition-dependence of the band gap, also known as the band gap bowing, has been extensively studied in recent years. However, consensus on the band gap bowing of the $Ga_{1-x}In_xN$ alloy has not been reached. A bowing parameter b of 1.43 eV is reported from an early measurement[34], while more recently a considerably larger value of 2.8 eV is experimentally observed[35]. Results from first-principles calculations range from 1.1 eV (HSE06)[36], 1.3 eV (LDA-1/2)[37] and 1.5 eV (mBJ)[38] to 2.1 eV (LDA+C)[39], depending on the exchange-correlation functional used. The enhancing effect of Indium clustering on the band gap bowing has also been examined[39, 40]. Previous first-principles calculations rely on either one reasonably sized special quansirandom structure (SQS) supercell or a statistical ensemble of clusters to

account for the compositional disorder. The virtual crystal approximation (VCA), on the other hand, has the main advantage of simplicity in modelling the disordered alloy. VCA has demonstrated good accuracy for semiconductor alloys and ferroelectric perovskite solid solutions[41, 42]. It offers an efcient way of studying quantities which are computationally more demanding such as vibrational properties and electron-phonon interactions. Indeed it is found that the inclusion of lattice vibrations, which is commonly neglected due to its prohibitive computational cost, could reduce the order-disorder transition temperature by ∼30%[43].

1.5 Outline

The thesis is organized as follows. Chapter 2 introduces the density-functional theory (DFT), the density-functional perturbation theory (DFPT) and the cluster expansion (CE) method. Chapter 3 presents an extensive study on the atomic, electronic and vibrational properties of the $(GaN)_{1-x}(ZnO)_x$ alloy using a modified version of the SQS method — the Special Quasi-ordered Structures (SQoS) method. Chapter 4 focuses on a convenient and accurate prediction of the bond-length distributions and bond-angle variations in the $(GaN)_{1-x}(ZnO)_x$ alloy using the bond valence method (BVM). Chapter 5 is devoted to the theoretical and computational studies of pyroelectricity in wurtzite GaN and ZnO. Chapter 6 reports on the structural, electronic and vibrational properties of the $Ga_{1-x}In_xN$ alloy. Other theories/methods used in this thesis (SQoS in Chapter 3, BVM in Chapter 4 and pyroelectric theory of Born in Chapter 5) are introduced at the beginning of each corresponding chapter respectively.

Chapter 2

2 Methods

2.1 Density Functional Theory

Density functional theory is based upon the Hohenberg-Kohn theorems[44].

Theorem I: For any system consisting of interacting electrons in an external potential $V_{\text{ext}}(r)$, the potential $V_{\text{ext}}(r)$ and hence the Hamiltonian is uniquely determined, except for a constant, by the ground state electron density $n_0(r)$. Theorem II: For any $V_{\text{ext}}(r)$, a universal functional for the total energy $E[n]$ in terms of the density $n(r)$ can be defined, the global minimum value of which is the exact ground state energy, while the density $n(r)$ minimizing the total energy functional $E[n]$ gives the exact ground state density $n_0(r)$. The Hohenberg-Kohn energy functional is

$$E_{\text{HK}}[n] = T[n] + \int d^3r V_{\text{ext}}(r)n(r) + E_{II} + E_{\text{int}}[n] \tag{2.1}$$

where $T[n]$ and $E_{\text{int}}[n]$ are kinetic and potential energies of the interacting electron system, and E_{II} is the interaction energy of the nuclei. While DFT is made possible by the Hohenberg-Kohn theorems, the exact functionals remain unknown. The Kohn-Sham approach replaces the original full interacting many-body system with an auxiliary non-interacting independent-electron system[45]. The Kohn-Sham energy functional is

$$E_{\text{KS}}[n] = T_s[n] + \int d^3r V_{\text{ext}}(r)n(r) + E_{II} + E_{\text{Hartree}}[n] + E_{\text{xc}}[n] \tag{2.2}$$

where $T_s[n]$ is the independent-electron kinetic energy, and the Hartree energy is given by

$$E_{\text{Hartree}}[n] = \frac{1}{2}\int \frac{n(r)n(r')}{|r-r'|}drdr' \tag{2.3}$$

All the complicated many-body exchange and correlation interactions are grouped into the exchange-correlation energy E_{xc}. By applying variation of the Kohn-Sham energy functional E_{KS} with respect to the wavefunctions,

Kohn-Sham approach leads to self-consistent Schrödinger-like independent-electron Kohn-Sham equations with an effective Kohn-Sham potential

$$\begin{aligned} V_{\mathrm{KS}}(r) &= V_{\mathrm{ext}}(r) + \frac{\delta E_{\mathrm{Hartree}}}{\delta n(r)} + \frac{\delta E_{\mathrm{xc}}}{\delta n(r)} \\ &= V_{\mathrm{ext}}(r) + V_{\mathrm{Hartree}}(r) + V_{\mathrm{xc}}(r) \end{aligned} \tag{2.4}$$

Fig. 2.1 shows schematically the flowchart for solving Kohn-Sham equations self-consistently[46].

Although the exact functional $E_{\mathrm{xc}}[n]$ is unknown, approximate functionals are proposed. The most widely used ones include the Local Density Approximation[47, 48] (LDA) and the Generalized Gradient Approximation[49] (GGA). The LDA exchange and correlation potential $V_{\mathrm{xc}}^{\mathrm{LDA}}$ is derived from the homogeneous electron gas model, and is expressed in terms of the local density $n(r)$ as

$$V_{\mathrm{xc}}^{\mathrm{LDA}}(r) = \epsilon_{\mathrm{xc}}^{\mathrm{hom}}(n(r)) + n(r)\frac{\partial \epsilon_{\mathrm{xc}}^{\mathrm{hom}}(n(r))}{\partial n(r)} \tag{2.5}$$

The GGA exchange and correlation potential $V_{\mathrm{xc}}^{\mathrm{GGA}}$ requires the local density and its gradient

$$V_{\mathrm{xc}}^{\mathrm{GGA}}(r) = \epsilon_{\mathrm{xc}}^{\mathrm{hom}}(n(r)) + n(r)\frac{\partial \epsilon_{\mathrm{xc}}^{\mathrm{hom}}(n(r))}{\partial n(r)} - \nabla\left(n(r)\frac{\partial \epsilon_{\mathrm{xc}}^{\mathrm{hom}}(n(r))}{\partial \nabla n(r)}\right) \tag{2.6}$$

2.2 Density Functional Perturbation Theory

While DFT provides the ground state electron density and total energy, the Density Functional Perturbation Theory investigates response functions under external perturbations. DFPT has been particularly successful in predicting many physical properties[50]. Typical perturbations include atomic displacement, strain and external macroscopic electric field. Consider the phonon perturbation $\{R\}$. According to the Hellmann-Feynman theorem, the matrix of interatomic force constants (IFCs) read

$$\frac{\partial^2 E_{\mathrm{KS}}(\{R\})}{\partial R_I R_J} = \int \frac{\partial^2 V_{\mathrm{KS}}(\{R\})}{\partial R_I R_J} n(r) dr + \int \frac{\partial V_{\mathrm{KS}}(\{R\})}{\partial R_I}\frac{\partial n(r)}{\partial R_J} dr \tag{2.7}$$

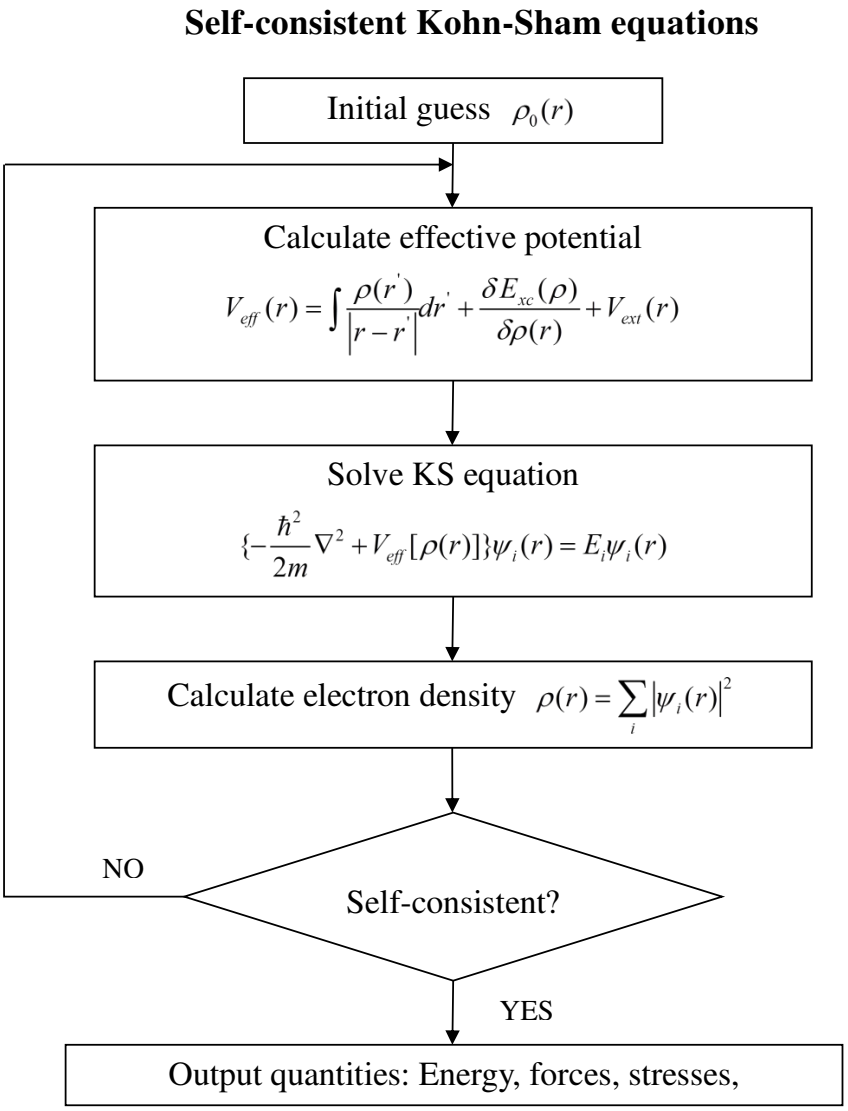

Figure 2.1: Schematic representation of the self-consistent loop for solution of Kohn-Sham equations.

The linear response of the ground state electron density is

$$\frac{\partial n(r)}{\partial R_I} = 4\mathrm{Re}\sum_{\mathrm{m=1}}^{\mathrm{N/2}} \psi^*_{\mathrm{m}}(\mathrm{r})\frac{\partial \psi_{\mathrm{m}}(\mathrm{r})}{\partial \mathrm{R_I}} \tag{2.8}$$

The variation of wavefunctions is obtained by first-order perturbation theory:

$$(H^{(0)}_{\mathrm{KS}} - \epsilon^0_m)|\psi^{(1)}_m\rangle = -(H^{(1)}_{\mathrm{KS}} - \epsilon^1_m)|\psi^{(0)}_m\rangle \tag{2.9}$$

where $H^{(0)}_{\mathrm{KS}} = -\frac{1}{2}\nabla^2 + V_{\mathrm{KS}}$ is the unperturbed Kohn-Sham potential, and $H^{(1)}_{\mathrm{KS}}$ is its first-order variation

$$H^{(1)}_{\mathrm{KS}} = V^{(1)}_{\mathrm{ext}}(r) + \int \frac{n^{(1)}(r')}{|r-r'|}dr' + \int \frac{\delta V_{\mathrm{xc}}}{\delta n(r')} n^{(1)}(r')dr' \tag{2.10}$$

Analogous to the Kohn-Sham equations, equations (2.8)-(2.10) form a set of self-consistent equations, the solution of which readily leads to IFCs in Eqn. (2.7).

2.3 Cluster Expansion Method

In the cluster expansion (CE) method, the energetics of a substitutional alloy is modeled by a generalized Ising-type Hamiltonian. Consider a binary alloy $\mathrm{A}_x\mathrm{B}_{1-x}$, the total energy as a function of volume V is expressed as[4]

$$E(V) = \sum_n v_n(V)\xi_n \tag{2.11}$$

where $v_n(V)$ is the (unknown) many-body interaction potential, also referred to as effective-cluster interactions (ECIs) in some literature. ξ_n is the multi-site correlation of an nth order cluster. The correlation function is written as

$$\xi_n = \frac{1}{N_n}\sum_{\{p\}} \sigma_{p_1}\sigma_{p_2}...\sigma_{p_n} \tag{2.12}$$

where the spin variable σ_p takes the value of $+1$ (if the site is occupied by an A atom) or -1 (if the site is occupied by a B atom). The summation goes over all the N_n number of clusters in a given structure. It can be shown that

Table 2.1: Values of ECIs in meV.

$\{0,0\}$	$\{1,1\}$	$\{2,1\}$	$\{2,2\}$	$\{2,3\}$	$\{2,4\}$	$\{2,5\}$	$\{2,6\}$
495.69	-2.20	-134.19	-112.95	29.29	29.82	31.21	39.25
$\{2,7\}$	$\{2,8\}$	$\{2,9\}$	$\{2,10\}$	$\{2,11\}$	$\{2,12\}$	$\{2,13\}$	$\{2,14\}$
-6.89	-4.96	-4.19	-0.88	-1.55	-3.59	-5.24	-4.88

the expansion is exact if the correlation functions form a complete basis in the configurational space[3, 4, 5]. In practice, it is often sufficient to truncate the correlations to the first few nearest neighbor pair/three-body/four-body interactions. Then the ECIs can be treated as fitting parameters, and the truncated total energies are obtained from first-principles DFT calculations for selected configurations. Since $v_n(V)$ is volume-dependent, it is important that the total energy is minimized at the corresponding equilibrium volume with respect to only the internal atomic coordinates. In the present study we use a previously constructed CE model for the $(GaN)_{1-x}(ZnO)_x$ alloy[2]. Table 2.1 lists the values of the ECIs thus obtained. The geometries of the clusters are enumerated in the inset of Fig. 3.1.

Once constructed, the CE model requires the site occupancy as input and allows one to study the thermodynamic properties of the alloy from Monte-Carlo simulations[51]. For example, in Fig. 2.2 we show for the $(GaN)_{1-x}(ZnO)_x$ alloy the energy distribution of ensembles thermodynamically equilibrated at 1200K and $10,000$K. In Fig. 2.3, we show for the $(GaN)_{1-x}(ZnO)_x$ alloy at x=0.5 the formation energy as a function of temperature. Through the Monte-Carlo simulations combined with the CE method, we are able to predict that the $(GaN)_{1-x}(ZnO)_x$ alloy at x=0.5 orders at low temperatures and undergoes a first-order order-disorder transition at $T \approx 870$K. Other properties, such as the configurational entropy, could also be evaluated in a similar manner (Fig. 2.4).

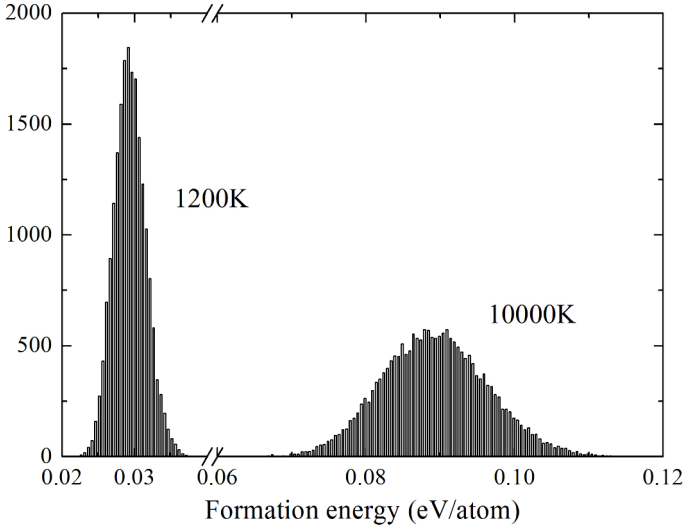

Figure 2.2: Energy distribution $P(E)$ for the $(GaN)_{1-x}(ZnO)_x$ alloy at x=0.5, equilibrated at $T = 1200$K and $T = 10,000$K.

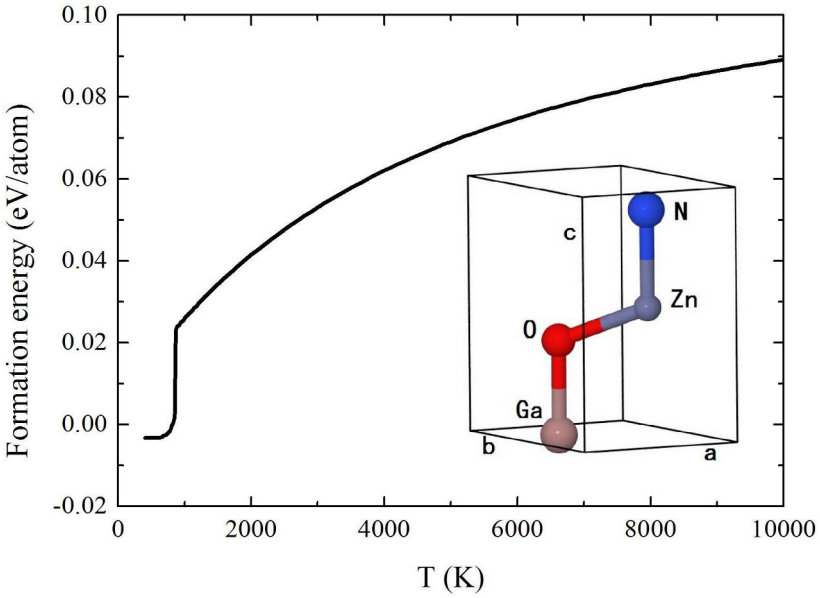

Figure 2.3: Formation energy as a function of temperature at x=0.5. The statistical error is smaller than the width of the line.

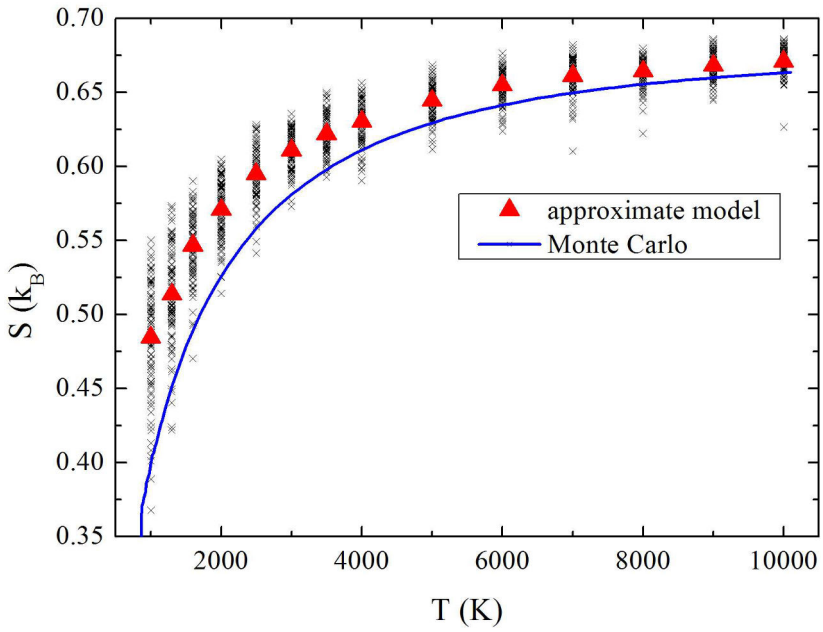

Figure 2.4: Configurational entropy at x=0.5 calculated with the Monte-Carlo simulation and with a SRO-corrected approximate model.

Chapter 3

3 $(GaN)_{1-x}(ZnO)_x$: Short-range Order

3.1 Special Quasi-ordered Structures

Understanding the role of order and disorder in determining physical properties such as bond length is complicated by the difficulty in modeling the numerous local chemical environments of the alloy. The motivation of the SQS approach is to approximate the actual alloy with one representative special structure S whose structural correlation functions $\overline{\Pi}_{k,m}(S)$ best match the corresponding ensemble-averaged $\langle\overline{\Pi}_{k,m}\rangle$ of the realistic alloy. For the structural correlations, the notations are adopted from Ref. [52]. The site occupation is denoted by Ising spin σ_i with $\sigma = 1$ denoting Ga/N and $\sigma = -1$ denoting Zn/O. The total energy of configuration s is expanded in terms of clusters (called "figures" and labeled as $\{k, m\}$). The label $k = 1, 2, ...$ is the number of sites of the cluster. The label $m = 1, 2, ...$ enumerates the distinct cluster geometries. The structural correlation function $\Pi_{k,m}(l, s)$ describes the occupation of the cluster. The label (l, s) indicate that the cluster is located at location l in configuration s. For instance, the notation $\Pi_{2,1}(l, s)$ refers to the spin product $\sigma_i\sigma_j$ for the particular nearest-neighbor pair of sites i and j positioned at location l in configuration s. $\overline{\Pi}_{k,m}(s)$ refers to the average of $\Pi_{k,m}(l, s)$ over all locations l in one configuration s, and $\langle\overline{\Pi}_{k,m}\rangle$ refers to the average of $\overline{\Pi}_{k,m}(s)$ over the ensemble equilibrated at a certain (x, T).

The original SQS approach reproduces the average structural correlation functions of the *random* (R) alloy $\overline{\Pi}_{k,m}(S) \sim \langle\overline{\Pi}_{k,m}\rangle_R$[52]. Therefore the original SQS represent the optimal supercell approximation to the completely disordered alloy with a given computationally affordable number of atoms per supercell. In this study, the SQS approach is extended to approximating the correlation functions of short-range ordered alloys $\langle\overline{\Pi}_{k,m}\rangle_{SRO}$. $\langle\overline{\Pi}_{k,m}\rangle_{SRO}$ is first obtained by performing Monte Carlo simulations on a DFT-based cluster expansion model. Then numerous site occupancies for

a certain composition x are generated and the representative configuration S for which the set of $\overline{\Pi}_{k,m}(S)$ is closest to $\langle\overline{\Pi}_{k,m}\rangle_{SRO}$ is selected by minimizing $\sum_{k,m} g_{k,m}D_{k,m}\left[\overline{\Pi}_{k,m}(s) - \langle\overline{\Pi}_{k,m}\rangle_{SRO}\right]^2$, where $D_{k,m}$ is the degeneracy (number of equivalent figures) and $g_{k,m}$ is the assigned weighting factor. Enumeration of all possible configurations is not possible since the number grows exponentially with the number of atoms in the supercell. However, increasing the size of the supercell allows better flexibility of matching structural correlation functions. The conflict is eased by the short-range nature of the structural correlations of the $(GaN)_{1-x}(ZnO)_x$ alloy. The most relevant physical property of the $(GaN)_{1-x}(ZnO)_x$ alloy is the formation energy, which is dominated by the short-range pair structural correlations[2]. Therefore large weighting factors are assigned to the nearest-neighbor $\{2, 1\text{-}2\}$ and next nearest-neighbor $\{2, 3\text{-}6\}$ figures. At each (x, T), 1×10^5 72-atom supercell ($3 \times 3 \times 2$) candidate structures are generated, among which the best-matching structure S is selected. Notice that the obtained structures are not optimal. However, the contributions to the energetics from longer-range figures $E(s) - \langle E\rangle = \sum_{k,m} D_{k,m}\left[\overline{\Pi}_{k,m}(s) - \langle\overline{\Pi}_{k,m}\rangle_{SRO}\right]\epsilon_{k,m}$ (Eq. (3.1) in Ref. [52]) are reasonably small. To avoid confusion, I name the corresponding special structure for the short-range ordered alloy (equilibrated at the experimental synthesis temperature $T = 1,123$K[1]) as SQoS (Special Quasi-ordered Structure), and for the disordered alloy (equilibrated at an unrealistic high temperature $T = 20,000$K) as SQdS (Special Quasi-disordered Structure), in resemblance to the widely used SQS (Special Quasi-random Structure) formalism introduced by Zunger[52]. A completely random "SQS" at $x = 0.5$ is also studied for reference.

3.2 Structural Correlations

The $(GaN)_{1-x}(ZnO)_x$ alloy was modeled in the wurtzite structure with interpenetrating cation and anion *hcp* sublattices. Ga/Zn can only occupy the cation sublattice, while N/O can only occupy the anion sublattice. A detailed description of the cluster expansion model used in this study can be found in Ref. [2]. Monte Carlo simulations are performed using the *ATAT* package[53, 54, 55] with a $12 \times 12 \times 8$ supercell containing 4608 atoms. For each (x, T), an ensemble of N configurations (labeled by $s = 1, 2, ..., N$) is equilibrated for 1×10^4 MC passes followed by a subsequent 1×10^4 MC

passes sampling.

The $(GaN)_{1-x}(ZnO)_x$ alloy is thermodynamically stable over the full range of compositions for $T > 870$K. The $x = 0.5$ alloy orderes at low temperature and undergoes a first-order order-disorder transition at $T \approx 870$K. The ground state is an ordered 50%-50% superlattice labeled as $(GaN)_1(ZnO)_1$, where GaN and ZnO double layers stack alternately along the hexagonal c-axis ($P6_3mc$). The formation energy for the $(GaN)_1(ZnO)_1$ superlattice is predicted to be small and negative, indicating the stability against phase separation. An analogous superlattice structure is also predicted for $(SiC)_m(AlN)_n$ alloy[9]. Upon alloying, the main effect of SRO is to enhance the statistical presence of the valence-matched nearest-neighbor Ga-N and Zn-O pairs. As shown in Fig. 3.1, the ensemble-averaged pair correlation functions $\langle\overline{\Pi}_{2,m}\rangle$ at $x = 0.5$ reveal a large degree of SRO. The nearest-neighbor $\langle\overline{\Pi}_{2,1-2}\rangle$ deviate significantly from the null value of the random alloy, while the next nearest-neighbor $\langle\overline{\Pi}_{2,3-6}\rangle$ are relatively small, comparable with those found in ternary nitride isovalent semiconductor alloys[16]. Longer-range $\langle\overline{\Pi}_{2,7-14}\rangle$ are not important. The long tail of the $\langle\overline{\Pi}_{k,m}\rangle - T$ curve also indicates that SRO persists to high temperature, and therefore complete randomness may not be achievable under common experimental growth conditions. The positive signs of $\langle\overline{\Pi}_{2,1-2}\rangle$ indicate nearest-neighbor preference for the valence-matched Ga-N and Zn-O pairs, while the positive signs of $\langle\overline{\Pi}_{2,3-6}\rangle$ indicate next nearest-neighbor preference for Ga-Ga and Zn-Zn as well as N-N and O-O pairs. The composition dependence of $\langle\overline{\Pi}_{k,m}\rangle$ at $T = 1,123$K is shown in Fig. 3.2. The deviation of $\langle\overline{\Pi}_{k,m}\rangle$ from that of the random alloy increases upon mixing, and yields the largest deviation at $x = 0.5$, where neglect of SRO is worst. To compare the degree of SRO included in SQoS, SQdS and SQS, the corresponding structural correlation functions at $x = 0.5$ are summarized in Table 3.1. In spite of the small size of the supercell, the statistical accuracy is good. The 72-atom SQoS, SQdS and SQS accurately reproduce the ensemble-averaged structural correlation functions obtained with a $12 \times 12 \times 8$ supercell. These special structures are expected to yield an accurate description of the atomic, electronic and vibrational properties of the $(GaN)_{1-x}(ZnO)_x$ alloy.

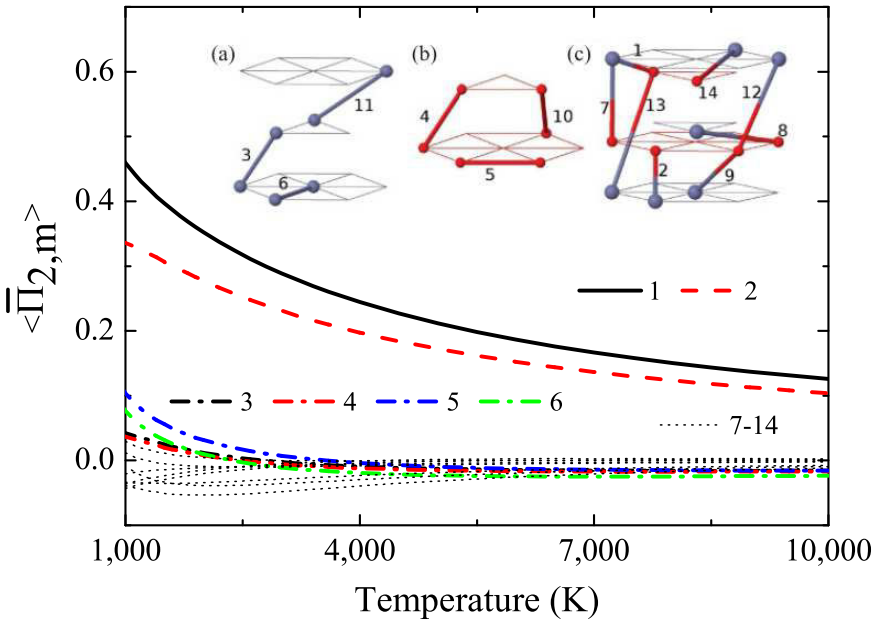

Figure 3.1: Ensemble-averaged pair correlation functions $\langle\overline{\Pi}_{2,m}\rangle$ at $x = 0.5$. Definitions of pair figures $\{2, m\}$ can be found in I. $\{2, 1\text{-}2\}$ and $\{2, 3\text{-}6\}$ stand for nearest-neighbor cation-anion pair figures and next nearest-neighbor cation-cation/anion-anion pair figures respectively. Longer-range pair figures $\{2, 7\text{-}14\}$ are shown by dotted lines.

3.3 Atomic, Electronic and Vibrational Properties

The constructed special structures are fully relaxed with respect to atomic coordinates, volume and shape. Electronic structure calculations are performed using the QUANTUM ESPRESSO package[56] with the PBEsol functional[57]. The pseudopotentials are constructed by means of the projector augmented wave (PAW) method[58, 59] with 60 Ry and 240 Ry cutoff energy for plane-wave basis set and charge density respectively. Ga-3d and Zn-3d states are treated explicitly as valence states. The k-point mesh is chosen to be equivalent to a $6 \times 6 \times 4$ mesh for the 4-atom wurtzite unit cell. To speed the structural relaxations, the input lattice parameters are estimated using Vegard's law[60]. Phonons are calculated using the small displacement method as implemented in the `PHON` code[61]. For each 72-atom primitive cell, a $2 \times 2 \times 2$ supercell is used while a small displacement of 0.02 Åis

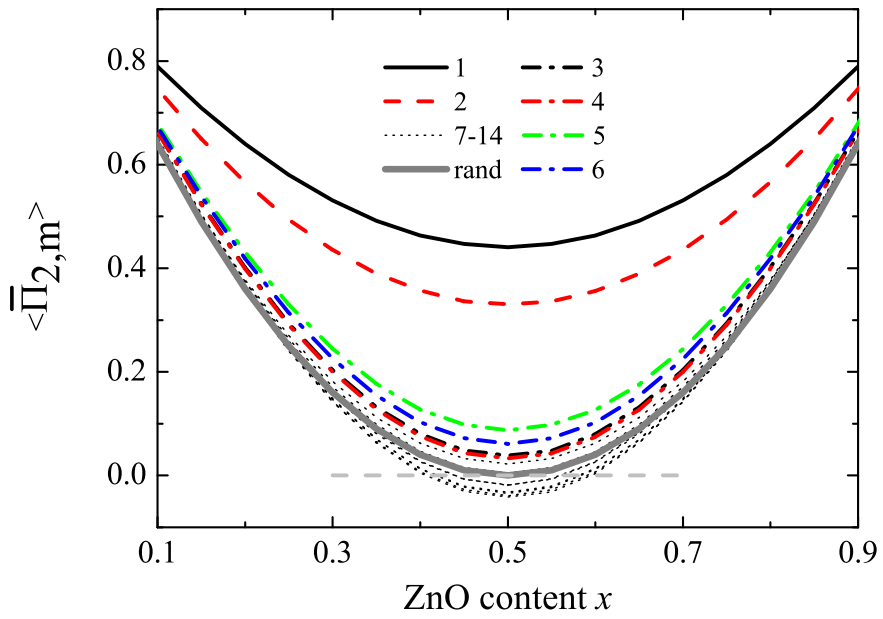

Figure 3.2: Ensemble-averaged pair correlation functions $\langle\overline{\Pi}_{2,m}\rangle$ at $T = 1,123$K. The structural correlations for the random alloy $\langle\overline{\Pi}_{k,m}\rangle_R = (2x-1)^k$ is shown by the solid grey line for comparison.

employed. The force constants are calculated with the SIESTA package[62]. Pseudopotentials for all the atomic species are available from the SIESTA homepage, except for Ga a smaller d-orbital cutoff radius is used[63].

GaN and ZnO have a type-II band alignment[15]. The valence band is composed mainly of N-2p states. DFT with LDA or GGA tends to over-delocalize the semicore Zn-d states and consequently over-hybridize the semicore Zn-d states with the N-p states, resulting in an enhancement of the $p-d$ repulsion. The band gap is therefore severely underestimated due to the artificially large $p-d$ repulsion. In this study U corrections are added to the semicore Ga-d and Zn-d states[64]. The on-site Coulomb interaction parameter $U \sim 3.1$eV is determined by a first-principles method adopted in Ref. [65]. U is approximated as the screened *atomic* on-site Coulomb interaction U^{at}/ϵ_∞, where U^{at} is the Coulomb energy cost of placing two electrons at the same site $U^{at} = E_{at}(d^{n+1}) + E_{at}(d^{n-1}) - 2E_{at}(d^n)$ and ϵ_∞ is the optical (high-frequency) dielectric constant. In this study, d^9 occupancy is taken

Table 3.1: 72-atom SQS at $x = 0.5$.

	$\overline{\Pi}_{2,m}$-SQoS	$\langle\overline{\Pi}_{2,m}\rangle_{1,123K}$	$\overline{\Pi}_{2,m}$-SQdS	$\langle\overline{\Pi}_{2,m}\rangle_{20,000K}$	$\overline{\Pi}_{2,m}$-SQS
$\{2,1\}$	0.444	0.442	0.074	0.070	0
$\{2,2\}$	0.333	0.333	0.000	0.058	0
$\{2,3\}$	0.037	0.041	-0.037	-0.011	0
$\{2,4\}$	0.037	0.036	0.000	-0.012	0
$\{2,5\}$	0.074	0.089	-0.037	-0.012	0
$\{2,6\}$	0.074	0.063	0.000	-0.016	0

as the reference point for d^n. The optical dielectric constant ϵ_∞ is calculated from linear-response theory[50]. A similar approach of screening the exact-exchange by the dielectric constant is shown to improve significantly the performance of the traditional hybrid functionals[66].

The calculated U^{at}, ϵ_∞ and U parameters are listed in Table 3.2. Compared to the experimental values[67], the calculated optical dielectric constant is overestimated due to the band-gap underestimation of DFT. However, since the atomic and electronic structures are not sensitive to the U parameters, the error in the calculated ϵ_∞ (and also the choice of the reference point for d^n) does not affect the main conclusions drawn in this study. The calculated lattice constants and band gaps are listed in Table 3.3. DFT-PBEsol calculations accurately reproduce the lattice constants of GaN and ZnO. The overall improvement compared with LDA of the lattice constants comes at the cost of severely weakening the influence of U corrections on the band gap. The band gap of ZnO is more sensitive to the U correction, due to the strong interaction between the high-lying Zn-3d states and the O-2p states. Subsequent DFT+U calculations are performed on the SQoS, SQdS and SQS in order to obtain accurate electronic structure properties. For comparison, total energy and force calculations on configurations randomly selected from the $T = 1,123K$ ensembles are also performed within the DFT+U methodology. As shown in Fig. 3.3, the constructed SQoS accurately represents the ensemble-averaged energetics of the short-range ordered $(GaN)_{1-x}(ZnO)_x$ alloy. The formation energy of SQoS is significantly lower than that of SQdS. The effect of SRO on the energetics grows upon mixing. Even at $T = 20,000$K, the formation energy of SQdS is still considerably lower than that of SQS due to the non-negligible residual SRO. SRO also

Table 3.2: Calculated U^{at}, ϵ_∞ and the corresponding U parameters for GaN and ZnO. Experimental values are shown in parenthesis. The PBE version[49] of the GGA functional is used instead of PBEsol in obtaining U^{at}, due to its better treatment of free atoms.

	U^{at} (eV)	ϵ_∞	U (eV)
GaN	18.1	5.9 (5.35)	3.1
ZnO	16.1	5.2 (3.71)	3.1

Table 3.3: Calculated lattice constants a and c and band gaps E_g.

	GaN			ZnO		
	a (Å)	c (Å)	E_g	a (Å)	c (Å)	E_g (eV)
PBEsol	3.182	5.187	1.88	3.225	5.207	0.71
PBEsol+U	3.184	5.189	1.89	3.232	5.213	0.92
Expt.	3.189	5.185	3.3	3.250	5.204	3.4

plays an important role in determining the structural properties. Fig. 3.4 compares the lattice constant bowing obtained theoretically and experimentally. Once again the lattice constants of SQoS accurately reproduce the corresponding ensemble-averaged values. With reduced SRO, the disordered alloy shows an expansion as well as a larger bowing compared to the short-range ordered alloy. The experimentally synthesized samples[11, 12] also exhibit moderate bowing, larger than the short-range ordered alloy but smaller than the disordered alloy, indicating the presence of SRO. Fig. 3.5 shows the (nearest-neighbor) bond-length distribution of the short-range ordered (T=1123K) alloy at $x = 0.5$. In the $(GaN)_{1-x}(ZnO)_x$ alloy, the Ga-N bonds shrink while the Zn-O bonds expand. This unusual bond-length distribution is determined by the non-isovalent nature of the alloy. Chapter 4 of this thesis will discuss the prediction and explanation of the bond-length distribution based on the concept of bond valence[6]. For the $(GaN)_{1-x}(ZnO)_x$ alloy, the Zn-N bond-length distribution has crucial importance since it is related to the band-gap reduction through the Zn3d-N2p repulsion. In Fig. 3.6 the dependence of band gap reduction on the ZnO content is shown. The Zn-N bond-length distribution of the short-range ordered alloy shifts to shorter bonds as the ZnO content increases. Shorter Zn-N bond lengths result in stronger Zn3d-N2p repulsion and therefore significantly push up the top of

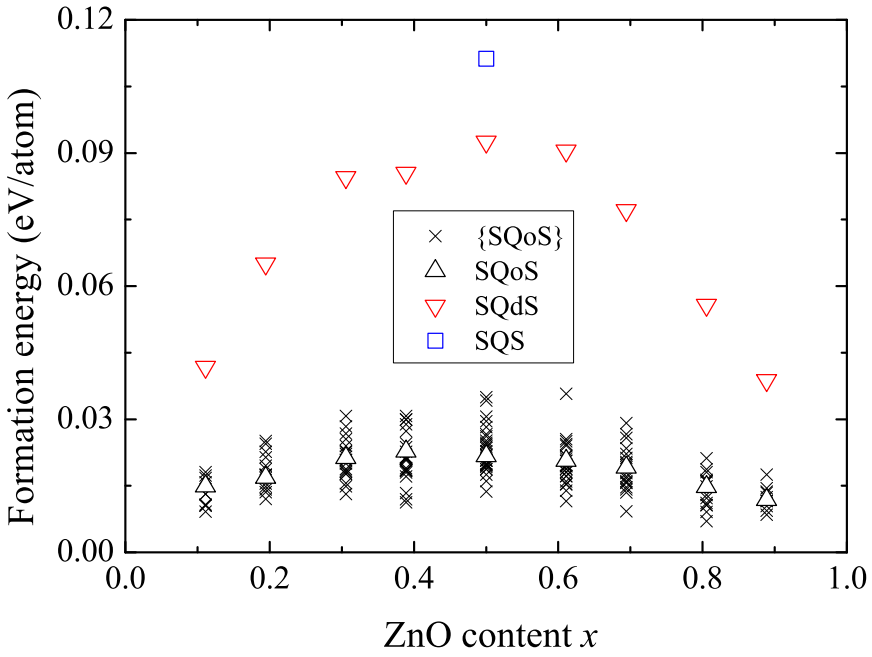

Figure 3.3: DFT-calculated formation energies of SQoS, SQdS and SQS. {SQoS} is a set of configurations randomly selected from the $T = 1,123K$ ensemble.

the valence band. Bond-angle variation is also unusual, namely N-Ga-N and Ga-N-Ga angles expand while O-Zn-O and Zn-O-Zn angles shrink relative to the ideal tetrahedral angle 109.5°. Fig. 3.7 shows the variation of bond angles. For example, the Ga centered bond angle shrinks with increased presence of ligand O atoms. This tendency can also be explained using the concept of bond valence. For Fig. 3.5-3.7, see Chapter 4 of this thesis for a statistically reliable prediction based on the bond valence method.

The atomic and electronic structures of the short-range ordered alloys deviate significantly from those of the disordered alloys. Theoretical atomistic modeling requires explicit inclusion of SRO. Fig. 3.8 shows the calculated band gaps of SQoS and SQdS. Due to the enhanced statistical presence of the Zn-N bonds, the band gap of the disordered alloy is further reduced relative to that of the short-range ordered alloy. The band-gap reduction is asymmetric. For the disordered alloys the band gap bowing is somewhat parabolic,

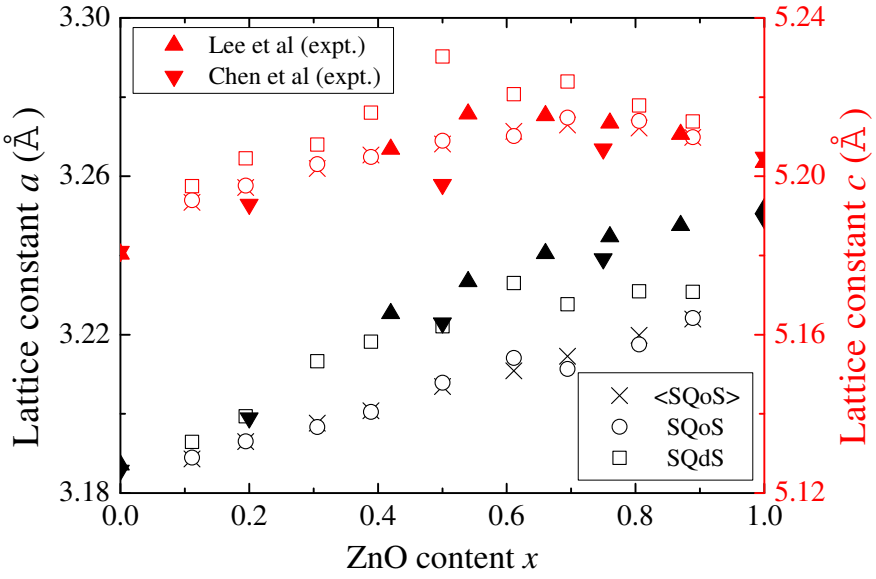

Figure 3.4: DFT-calculated lattice constants of SQoS and SQdS.

while for the short-range ordered alloys the band gap reduces almost linearly with increasing ZnO in the GaN host. The linear band-gap reduction is maintained even for the unrelaxed short-range ordered alloys, indicating the dominating role of configurational SRO. In Fig. 3.8, the linear redshift of the absorption onset with increased ZnO content observed in samples synthesized by nitridation of nanocrystalline $ZnGa_2O_4$ and ZnO precursors[11] is also shown. The linearity is a clear indication of the presence of SRO. Notice that the high-temperature and high-pressure synthesized samples exhibit the minimum gap at $x = 0.5$[12], which is somewhat consistent with the parabolic band gap bowing of the random alloy. The parabolic bowing is attributed to the promoted kinetics of mixing at high-temperature and high-pressure. The contrast in the band gap bowing is a clear indication of the importance of SRO. Since the SRO introduced in the sample is related to the synthesis techniques and the growth conditions, one might therefore consider the opportunity of engineering the band gap $E_g(x, T, \Pi)$ via SRO.

Fig. 3.9 compares the projected density of states (PDOS) of SQoS and SQdS at $x = 0.5$. The main contribution to the bottom of the valence band comes from O-2s states, which are taken as the reference level because they are

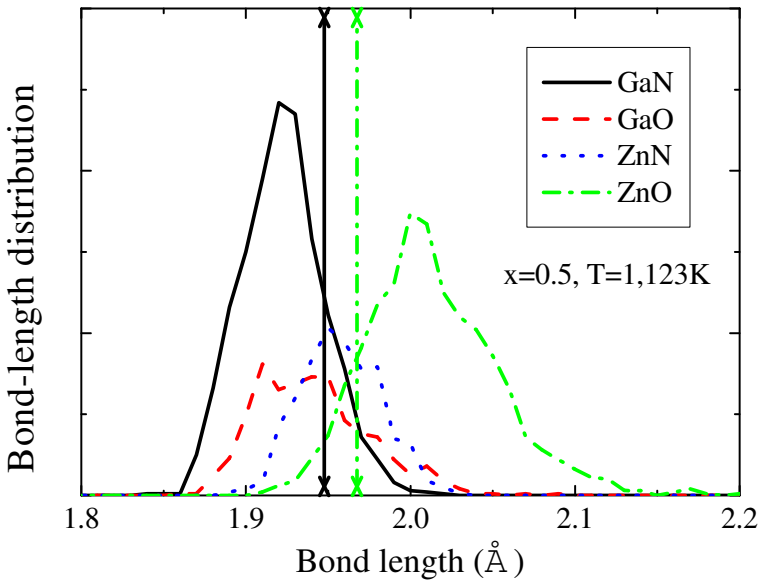

Figure 3.5: DFT-calculated bond-length distribution at $(x = 0.5, T = 1123)$. Thirty 72-atom structures are selected from the corresponding thermodynamic ensemble. The bin interval is set to 0.01Å. The vertical dotted lines mark the bond lengths of the corresponding compounds.

less sensitive to the local chemical environment. The top of the valence band is mainly composed of N-2p states. For the disordered alloy the increased statistical presence of the energetically unfavored Zn-N pairs pushes the band edge upward, resulting in further reduction of the band gap. The N-2p states depend strongly on the local chemical environment. Fig. 3.10 shows the PDOS of N-2p states with the N atoms surrounded by different numbers of Zn atoms. The N-2p states shift upward (dashed lines in Fig. 10) with increased presence of Zn neighbors.

The effect of lattice vibrations is included under the harmonic approximation. The phonon DOS for the SQoS alloys along with those of compound GaN and ZnO are shown in Fig. 3.11. Three mechanisms have been suggested to explain the origin of vibrational entropy differences in alloys[24]: the *bond proportion* effect, the *volume* effect and the *size mismatch* effect. Upon disordering, the *bond proportion* effect is typically associated with a broadening of the phonon DOS due to the statistical presence of bonds with

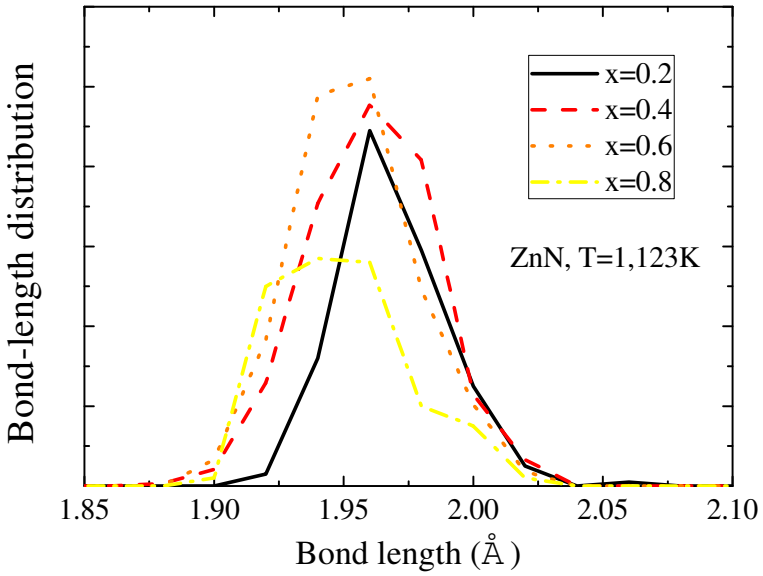

Figure 3.6: DFT-calculated Zn-N bond-length distribution at $T = 1123$K.

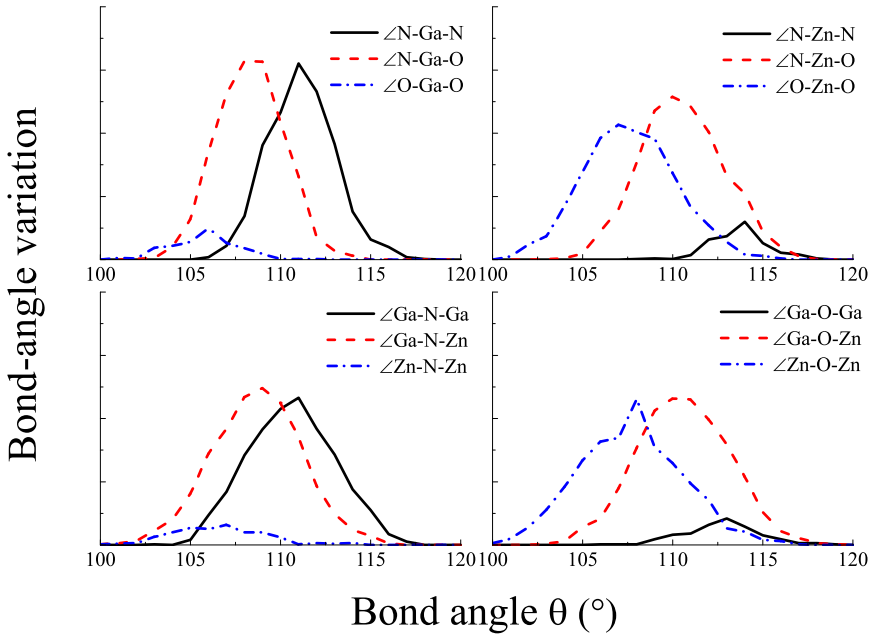

Figure 3.7: DFT-calculated bond-angle variation at $(x = 0.5, T = 1123)$.

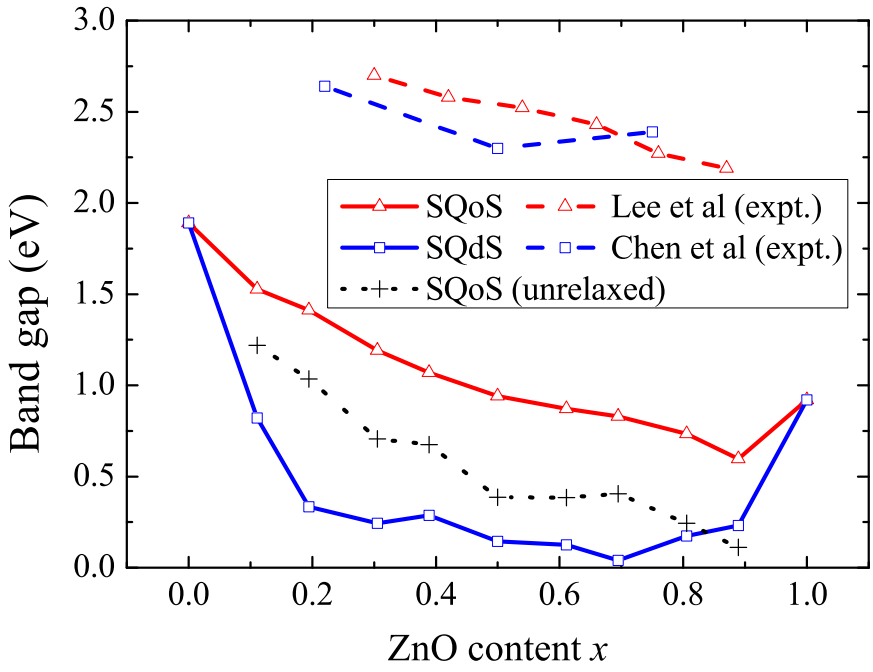

Figure 3.8: DFT-calculated band gaps of SQoS and SQdS. Experimental measurements (Lee et al in Ref. [11] and Chen et al in Ref. [12]) are also shown for comparison.

different stiffness. On the other hand, the *volume* effect is usually characterized by an overall shift of the phonon DOS due to the change in the frequency of all phonon modes. For the $(GaN)_{1-x}(ZnO)_x$ alloy, as the alloy expands with increasing x, the phonon DOS shifts to lower frequencies as the chemical bonds are in general softened. The *volume* effect is magnified by the fact that the "ionic" Zn-O bond is softer than the "covalent" Ga-N bond. The low-frequency phonon DOS could be well represented by the composition weighted average $(1-x)g_{\mathrm{GaN}}(\omega)+xg_{\mathrm{ZnO}}(\omega)$. The significant part of the phonon DOS difference (and therefore the vibrational entropy difference) comes from the high-frequency phonons. The effect of SRO is shown for the $x = 0.5$ case. The high-frequency phonon DOS of the SQdS exhibits a much broader spectrum than that of the SQoS. Consequently the phonon mixing entropy of the SQdS is three times larger than that of the SQoS, as is shown in Fig. 3.12. While the x-dependence of the configurational mixing entropy is symmetric[51], the x-dependence of the phonon mixing entropy is highly

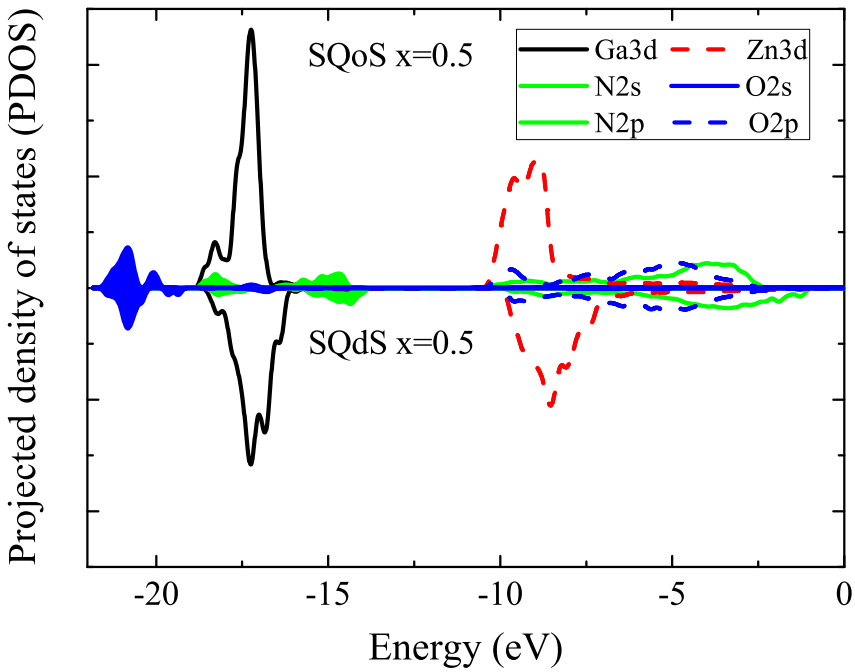

Figure 3.9: Projected density of states (PDOS) of the valence band. The cation-*s* states in the conduction band are not shown. The deep-lying anion-*s* states are shown by the shaded area.

asymmetric, indicating that the inclusion of the vibrational free energy into the alloy thermodynamics could alter the shape of the phase diagram.

3.4 Conclusion

The importance of SRO in atomistic modeling schemes such as the SQS approach is often overlooked. For binary metal alloys or isovalent semiconductor alloys, SRO is usually less important. However, for the non-isovalent semiconductor alloys, the valence-matching driving force induces significant SRO. The SQS approach provides a way of approximating the actual alloy with a DFT-affordable supercell. In order to properly compute the non-isovalent alloy, one needs prior knowledge of SRO. In this study the correlated site occupations are provided by Monte Carlo simulations on a DFT-based cluster

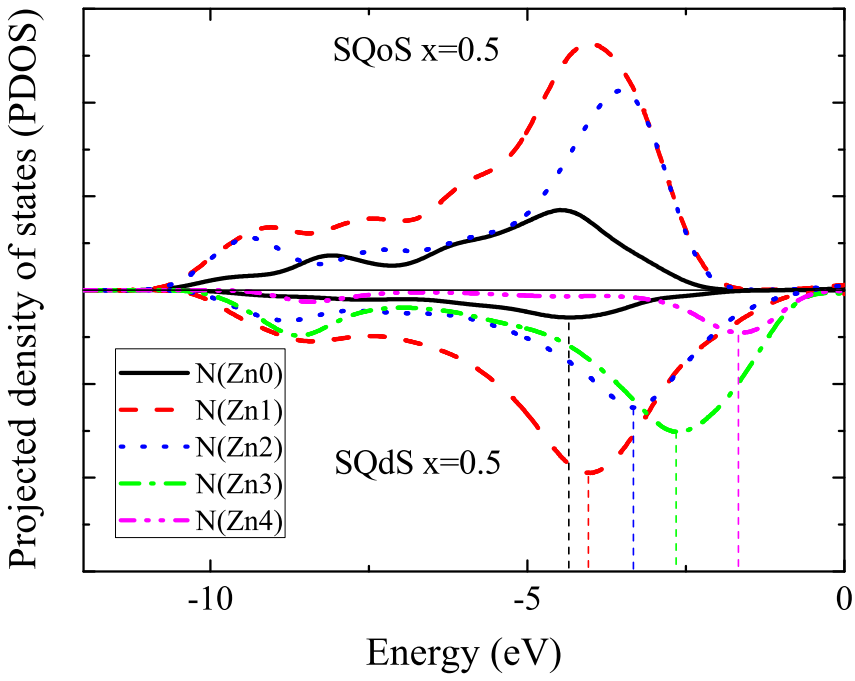

Figure 3.10: PDOS of N-2p with N atoms being surrounded by 0, 1, 2, 3 or 4 Zn neighbors. PDOS is not normalized so that the area under each curve represents the corresponding statistical presence.

expansion model. Exhausted enumeration of all possible site occupations is avoided due to the short-range nature of the $(GaN)_{1-x}(ZnO)_x$ alloy. We seek to match only the cation-anion nearest-neighbor and the cation-cation/anion-anion next nearest-neighbor correlations. The longer-range correlations are optimized to a lesser extent. Since the short-range nature is inherited in the non-isovalency, the construction of SQoS proposed in the present study should also be applicable to other non-isovalent semiconductor alloys. If longer-range correlations come into play, one might apply for example the evolutionary algorithm in order to efficiently search for the optimal SQoS.

In the present study we have revealed the presence of strong SRO in the $(GaN)_{1-x}(ZnO)_x$ alloy. We constructed reliable SQoS and SQdS whose structural correlations reproduce those of the short-range ordered alloys and the disordered alloys respectively. Atomic, electronic and vibrational properties of the short-range ordered alloys deviate significantly from those of the

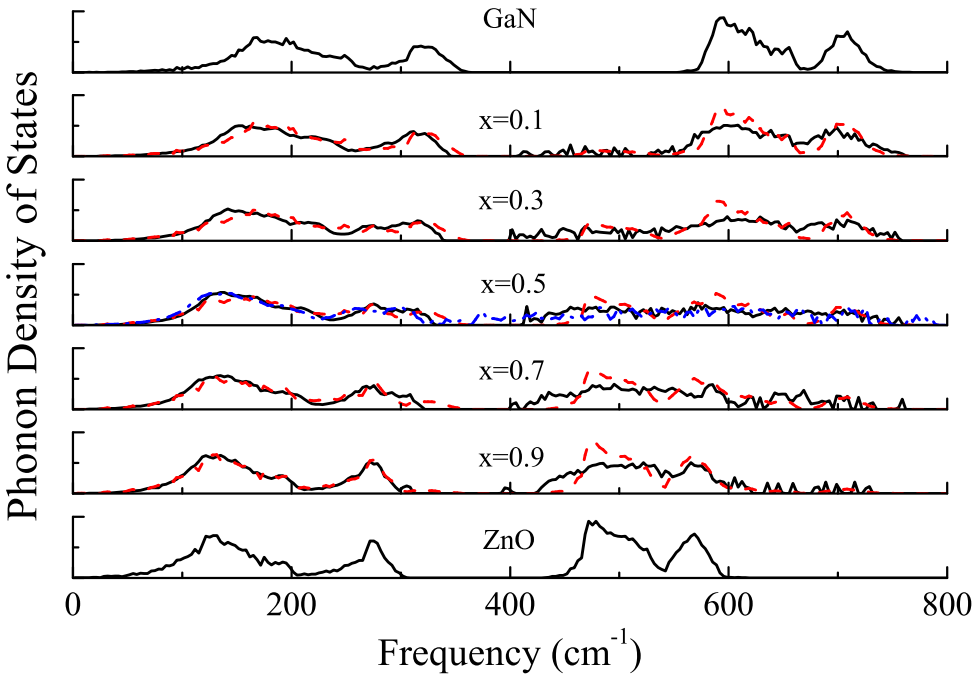

Figure 3.11: Phonon DOS for the SQoS (solid black) ($x = 0.1, 0.3, 0.5, 0.7$ and 0.9) and SQdS (dash-dot blue) ($x = 0.5$) alloys. The dash red lines represent the corresponding average of phonon DOS: $(1-x)g_{\mathrm{GaN}}(\omega)+xg_{\mathrm{ZnO}}(\omega)$.

disordered alloys. The short-range ordered alloys experience smaller lattice bowing than the disordered alloys. We offer a tentative explanation in terms of SRO for the discrepancy of the band gaps found in samples synthesized by different methods. SRO inhibits the nearest-neighbor Zn-N pairs, which affects the strength of the Zn3d-N2p repulsion and consequently the top of the valence band. The dependence of the N-2p states on local chemical environment demonstrates the vital role of SRO in accurately describing the $(\mathrm{GaN})_{1-x}(\mathrm{ZnO})_x$ alloy. Phonon DOS is sensitive to the presence of SRO. Disordered alloys could have much larger vibrational entropy of mixing than short-range ordered alloys.

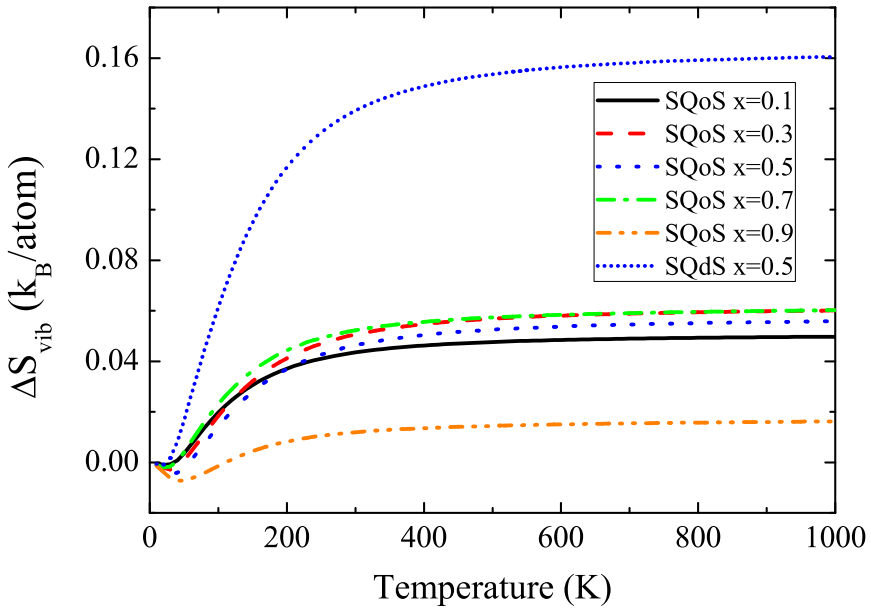

Figure 3.12: x-dependence of the phonon mixing entropy $\Delta S_{vib} = S_{vib}(x) - [(1-x)S_{vib}^{\mathrm{GaN}} + xS_{vib}^{\mathrm{ZnO}}]$.

Chapter 4

4 $(GaN)_{1-x}(ZnO)_x$: Bond Valence Method

4.1 Bond Valence Method

The BVM is extensively discussed in Ref. [68]. Each nearest-neighbor cation-anion bond is assigned a bond valence v_{IJ}. Next nearest-neighbor cation-cation/anion-anion interactions are neglected. The bond valence sum (BVS) of an atom is defined as the sum of the bond valences surrounding the atom. Each atom has an ionic valence equal to its corresponding formal ionic charge. By convention, V(Ga)=+3, V(N)=−3, V(Zn)=+2, V(O)=−2, $v_{IJ} = -v_{JI}$. Of crucial importance for non-isovalent semiconductor alloys are two rules: (1) the *valence sum rule* $V(I) = \sum_J v_{IJ}$, and (2) the *valence loop rule* $\sum_{loop} v_{IJ} = 0$. The *valence loop rule* is also known as the *equal valence rule*, since the zero circulation condition is equivalent to the minimization of $\sum_{I,J} v_{IJ}^2$ (see for example the appendix in Ref. [23]). The solution is a set of $\{v_{IJ}\}$ which minimizes the measure of the total energy $E = \alpha \sum_{I,J} v_{IJ}^2$ (α is the correlation constant) under the constraint of the *valence sum rule*.

The *valence sum rule* is interpreted by assuming the correlation $P_{IJ} \propto v_{IJ}$, where P_{IJ} is the Mulliken overlap population[69, 70]. As for the measure of the total energy, in solid state language, a perturbation expansion of the orbital interaction energy reads

$$E = \sum_{i \in I} \epsilon_i = \sum_{i \in I} \left(\epsilon_i^0 + \sum_{j \in J} \frac{|\langle \phi_i^0 | V | \phi_j^0 \rangle|^2}{\epsilon_i^0 - \epsilon_j^0} \right) \tag{4.1}$$

where ϵ_i^0 and ϕ_i^0 denote for atomic energy and orbital respectively. Capital I, J and lowercase i, j refer to atomic and orbital indices respectively. Assuming the correlation $H_{ij} \propto S_{ij}$ (H_{ij} is the matrix element $\langle \phi_i^0 | V | \phi_j^0 \rangle$ and S_{ij} is the overlap integral $\langle \phi_i^0 | \phi_j^0 \rangle$), the relaxation energy $E - \sum \epsilon_i$ is then proportional to $\alpha_{IJ} \sum_{i \in I, j \in J} S_{ij}^2$, where the denominator $\epsilon_i^0 - \epsilon_j^0$ reduces into the correlation constant α_{IJ}. The overlap integral $S_{ij}(r, \theta, \phi)$ can be

expressed in a separable form $S_{ij}(r)f(\theta,\phi)$[25]. The angular dependence is lifted after summing $\sum_{i\in I,j\in J} f^2(\theta,\phi)$ over all the interacting orbital pairs. The summation over orbital pairs then reduces to the summation over atom pairs. Finally the measure of the total energy $E = \alpha \sum_{I,J} v_{IJ}^2$ is obtained, with the definition of the bond valence $v_{IJ} \sim S_{IJ} = \sqrt{\sum_{i\in I,j\in J} S_{ij}^2}$. In the analogy of the Kirchhoff circuit law, the bond capacitances are all equal[17], which is equivalent to assuming α equal for different types of atomic pairs.

The radial dependence of $S_{ij}(r)$ derives naturally to the empirical exponential correlation between bond valence and bond length

$$v_{IJ} = \exp\left(\left(R_{IJ}^0 - R_{IJ}\right)/b_{IJ}\right) \tag{4.2}$$

where R_{IJ} is the observed bond length while R_{IJ}^0 and b_{IJ} are empirically fitted bond valence parameters for $I-J$ bond. b_{IJ} measures the bond softness and is usually taken as a universal constant of $0.37\mathring{A}$, while R_{IJ}^0 is experimentally determined from structural data of related materials[71]. In the present study, the disordered alloy offers abundant structural data. Therefore R_{IJ}^0 and b_{IJ} are fitted to DFT calculations instead. The bond-angle variation depends on the higher-order terms of orbital interactions in the perturbation expansion. In general the bond bending force is weaker than the bond stretching force. In the present study, an empirical relation[68] is used for the crude prediction of anion-cation-anion angles

$$\theta_{ICJ} = 109.5 + k(v_{CI} + v_{CJ} - V_C/2) \tag{4.3}$$

where k is an empirical constant (equal to 15.3° per valence unit (v.u.) in Ref. [68]), v_{CI} and v_{CJ} are the bond valences of the two ligand bonds, and V_C is the ionic valence of the central cation. The underlying geometrical implication of the linear correlation between bond angle and bond valence is the vectorization of the scalar bond valence[72]. Finally, taking into account the constraints of bond lengths and bond angles, the tetrahedrally coordinated alloy lattice is over-constrained. A cost function can be assigned to the constraints in order to perform the pre-relaxation.

4.2 Examination of BVM

To keep the integrity of this section, relevant computational methods are outlined. A Ising-type model Hamiltonian for the $(GaN)_{1-x}(ZnO)_x$ alloy is first constructed using a DFT-based cluster expansion method[3, 4, 5]. Monte-Carlo simulations are then performed on the constructed cluster expansion model using the *ATAT* package[53, 54, 55]. For each (x, T) of interest, a thermodynamic ensemble of configurations is generated. At this stage only the site occupancies are needed. For each configuration the bond valences can then be determined using BVM. One could in principle minimize the measure of the total energy $E = \alpha \sum_{I,J} v_{IJ}^2$ with respect to the set of bond valences $\{v_{IJ}\}$. Unlike the Ising-type cluster expansion model, BVM model is essentially long-ranged since the set of bond valences $\{v_{IJ}\}$ forms a interactive network. In order to speed the BVM solution, an iterative scheme[73] is used to apply the *equal valence rule*, which generally yields better computational efficiency. Finally the bond-length distribution and bond-angle variation are obtained using the empirical correlations.

For most of the results presented in this section, the Perdew-Burke-Ernzerhof (PBE)[49] version of the exchange-correlation functional is used. Kohn-Sham wavefunctions are expanded in a variationally optimized double-ζ polarized (DZP) basis set, as implemented in the SIESTA package[62]. Ga-3d and Zn-3d electrons are treated explicitly as valence electrons. The k-point mesh is chosen to be equivalent to a $6\times6\times4$ mesh for the 4-atom wurtzite unit cell. Pseudopotentials for all the atomic species are available from the SIESTA homepage[74]. DFT calculations are performed for two reasons: (1) The correlations $P_{IJ} \propto v_{IJ}$, $H_{ij} \propto S_{ij}$ and $v_{IJ} \sim S_{IJ}$ are crucial for the interpretation of BVM and are therefore examined first. (2) The BVM parameters are to be fitted to DFT calculations, after which bond-length distribution and bond-angle variation can be predicted. I construct three representative 432-atom supercells at $x = 0.25$, 0.5 and 0.75 for the former purpose, and use a thermodynamic ensemble equilibrated at the experimental synthesis temperature $T = 1,123$K[1] with 72-atom supercells for the latter purpose.

The *valence sum rule* is an equivalent statement of the principle of local charge neutrality. In Fig. 4.1 the correlations $P_{IJ} \propto v_{IJ}$ for different types of bonds are shown. One should keep in mind that the Mulliken population

has no strict physical sense due to its sensitivity over the projected atomic basis set. Therefore in present study only the qualitative correlation is discussed. The correlation $H_{ij} \propto S_{ij}$ is in reality adopted in the extended Hückel method[75] where the off-diagonal Hamiltonian matrix elements H_{ij} are approximated by the corresponding diagonal Hamiltonian matrix elements and the overlap integral through $H_{ij} = KS_{ij}(H_{ii} + H_{jj})/2$. In Fig. 4.2 the correlations $H_{ij} \propto S_{ij}$ between the first ζ numerical atomic orbitals of different species are shown. Since Ga and O are more electronegative than Zn and N respectively, Ga-4s and O-2p lie deeper in the atomic energy level diagram than Zn-4s and N-2p. Therefore Ga-O has the largest correlation while Zn-N has the smallest correlation. In Fig. 4.3 the correlations $v_{IJ} \sim S_{IJ}$ for different types of bonds are shown. The linearity of the correlations validates the interpretation of BVM proposed in the present study.

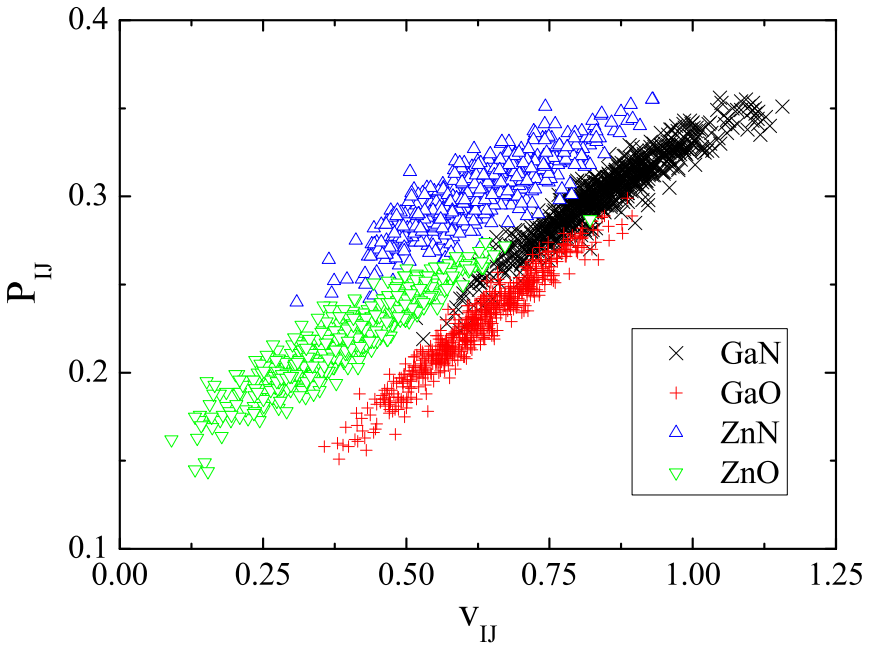

Figure 4.1: The correlation $P_{IJ} \propto v_{IJ}$ for different types of bonds.

The ability of BVM in predicting bond-length distribution relies significantly on the empirical correlation $v_{IJ} = \exp\left(\left(R^0_{IJ} - R_{IJ}\right)/b_{IJ}\right)$, the quality of which should be examined at the first stage. To yield accurate struc-

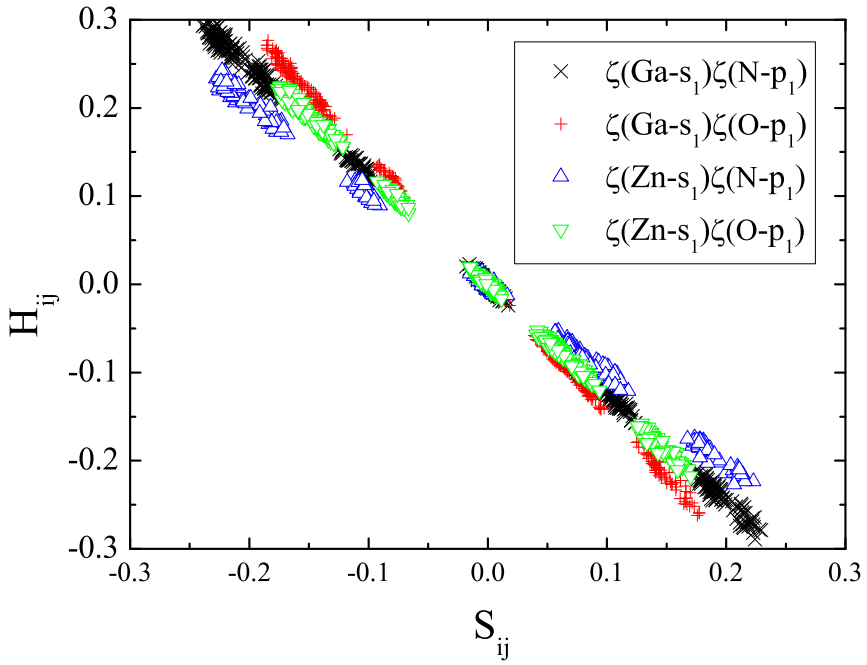

Figure 4.2: The correlation $H_{ij} \propto S_{ij}$ between the first ζ numerical atomic orbitals of different species.

tural properties, DFT calculations are performed using the QUANTUM ESPRESSO package[56] with the PBEsol functional[57]. The lattice constants of GaN and ZnO are well reproduced[76]. In Table 4.1, the original (tabulated in Ref. [71]) and fitted-to-DFT bond valence parameters are listed. As a sanity check, bond lengths of compound GaN and ZnO (labeled as R^0) calculated with the two sets of bond valence parameters are also listed. As the fitting procedure releases the freedom of the bond softness b_{IJ}, an overall improvement is observed for the fitted-to-DFT set of bond valence parameters. Fig. 4.4 shows the correlation between the DFT-calculated bond lengths and the BVM-predicted bond valences. Bond-length distribution is predicted by BVM with good accuracy. The prediction of bond-angle variation is less accurate, as is shown in Fig. 4.5. The fitted bond valence parameters k for Ga and Zn are 18.1°/v.u. and 20.1°/v.u. respectively. In order to perform the pre-relaxation, one can simply add a penalty function to bond-length distribution and bond-angle variation. A large penalty to bond-length distribution is suggested while bond angles are subject to change.

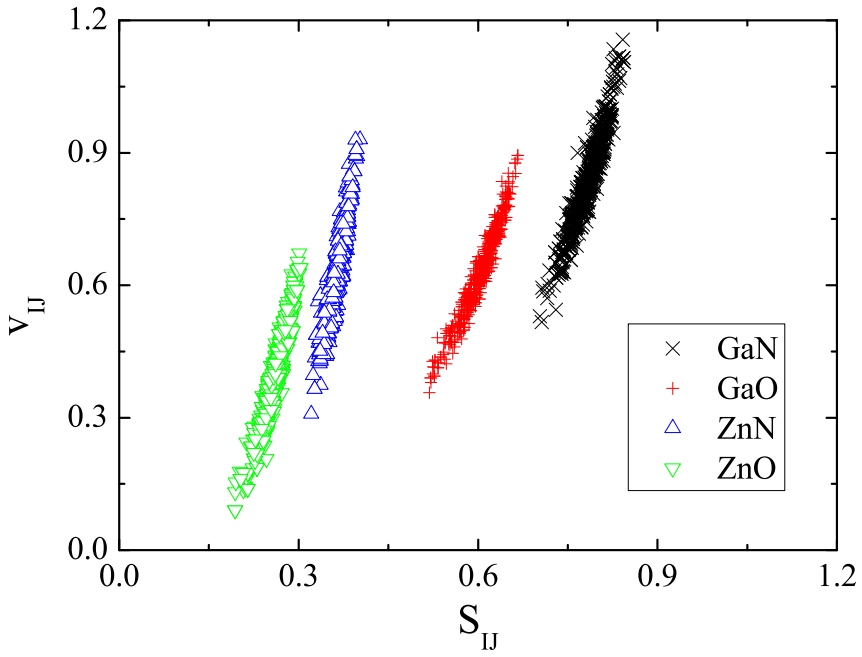

Figure 4.3: The correlation $v_{IJ} \sim S_{IJ}$ for different types of bonds. S_{IJ} is defined as $\sqrt{\sum_{i\in I, j\in J} S_{ij}^2}$.

4.3 Structural Relaxation

To represent the thermodynamic ensembles at (x, T), Monte-Carlo simulations are performed on a DFT-based cluster expansion model. Given the site occupancies of each configuration, bond-length distribution and bond-angle variation are then obtained using the fitted-to-DFT bond valence parameters. In the present study, temperature is interpreted as a measure of the degree of randomness. Temperatures of 1123K, 2000K, 5000K and 20000K represent short-range ordered (SRO), disordered (DIS1 and DIS2) and random (RAN) alloy respectively. Fig. 4.6 shows the bond-length distributions at various temperatures. As the temperature is raised, the peak of bond-length distribution shifts slightly toward shorter bond-length direction. The shift of the peak position is small, and can be easily overwhelmed by other factors such

Table 4.1: Bond valence parameters.

	original BVM[71]				fitted to DFT			
	GaN	GaO	ZnN	ZnO	GaN	GaO	ZnN	ZnO
$R_{ij}^0(\mathring{A})$	1.84	1.73	1.77	1.704	1.844	1.755	1.831	1.756
$b_{ij}(\mathring{A})$		0.37			0.357	0.391	0.268	0.312
R^0 (Å)	1.946	–	–	1.960	1.947	–	–	1.972
Expt. (Å)[67]	1.95	–	–	1.977	1.95	–	–	1.977

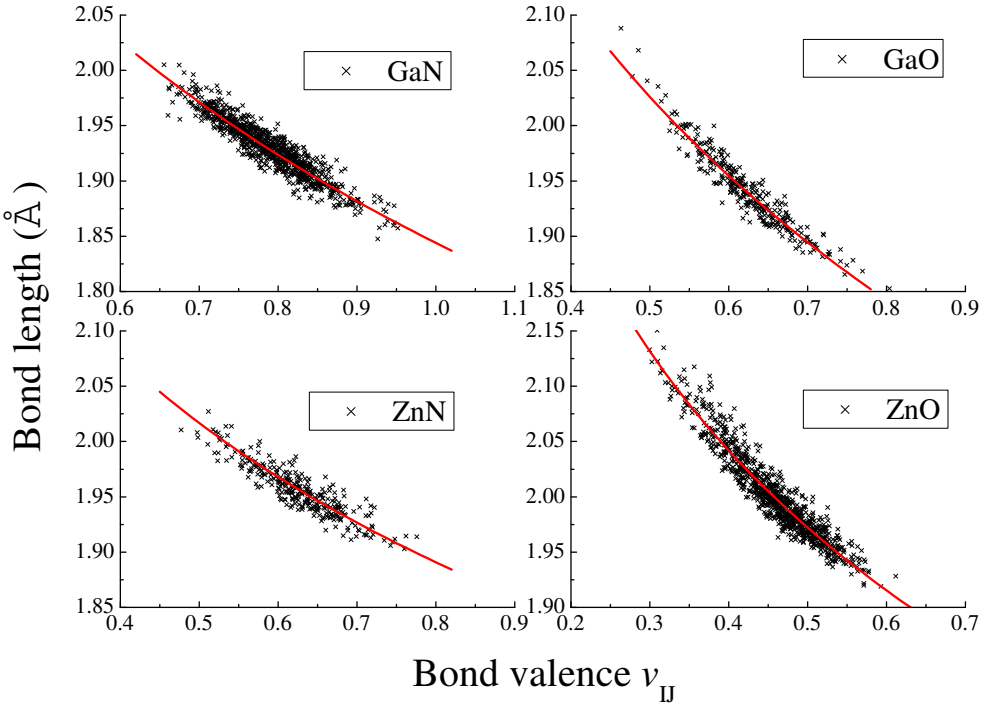

Figure 4.4: Correlations between the DFT-calculated bond lengths and the BVM-predicted bond valences. The solid red lines represent the fitted correlations. In each figure the number of data points drawn is reduced by a factor of ten.

as thermal expansion, which is not considered here. In the meanwhile the width of bond-length distribution becomes broader as increasing the degree of randomness. In Fig. 4.7 bond-length distributions of different types of bonds are shown. Upon mixing the Ga-N bond shrinks while the Zn-O bond

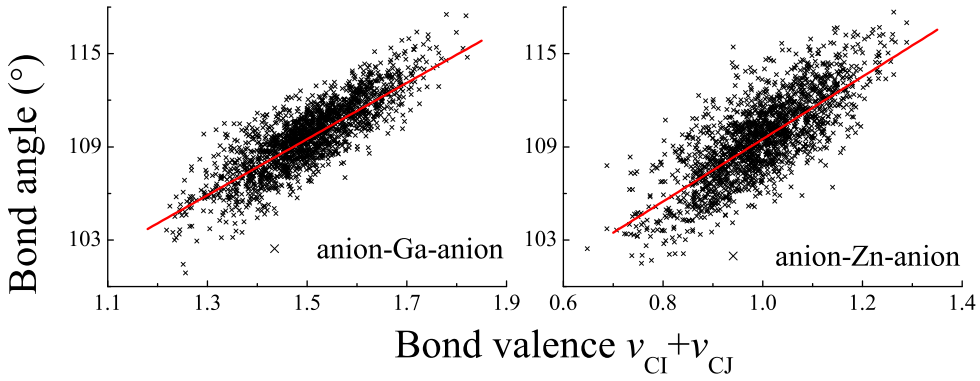

Figure 4.5: Correlations between the DFT-calculated bond angles and the BVM-predicted bond valences. The solid red lines represent the fitted correlations. In each figure the number of data points drawn is reduced by a factor of ten.

expands relative to the bond lengths in the corresponding compounds. From SRO alloy to RAN alloy, the shift is toward shorter bond-length direction for Ga-N, barely temperature-dependent for Ga-O and Zn-N, and is reversed to the longer bond-length direction for Zn-O. This unusual tendency of bond-length distribution is a consequence of the non-isovalent nature of the alloy, and can be easily interpreted in terms of bond valence. One consequence of elevating the degree of randomness is to enhance the statistical presence of the energetically unfavored valence-mismatched Ga-O and Zn-N pairs. In the language of BVM, for a cation-anion pair, enhancing the presence of N(O) neighbors around the cation and Ga(Zn) neighbors around the anion will drain(pour) bond valence from(into) the cation-anion pair and as a result the bond is lengthened(shortened). Of particular importance is the Zn-N bond-length distribution due to the decisive role of Zn3d-N2p repulsion on the top of the valence band. In the previous chapter, a almost linear band gap reduction upon increasing the ZnO content for the short-range ordered alloy is observed. Since the p-d repulsion is inversely proportional to the bond length, upon increasing the ZnO content a shortened Zn-N bond-length distribution is expected, which is confirmed by the BVM prediction shown in Fig. 4.8. The stronger p-d repulsion pushes the top of the valence band pushed, resulting in the linear band gap reduction. Fig. 4.9 shows the anion-cation-anion bond-angle variation of short-range ordered alloy at $x = 0.5$. The N-Ga-N angle expands while the O-Zn-O angle shrinks relative to the

ideal tetrahedral angle 109.5°, which can be explained by noticing that the bond valence of the ligand cation-O bond is generally smaller than that of the ligand cation-N bond. For Fig. 4.7-4.9, see the previous chapter for the DFT-calculated more reliable but less statistical predictions.

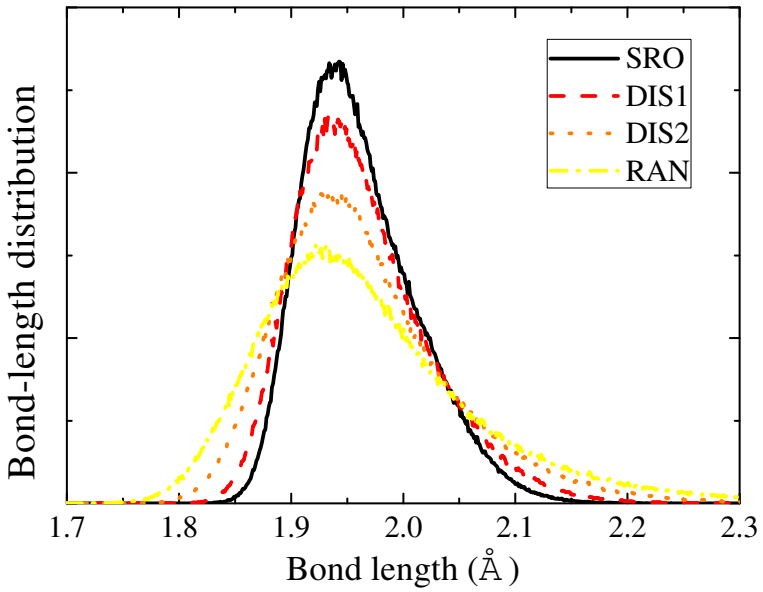

Figure 4.6: Temperature dependence of bond-length distribution at $x = 0.5$.

4.4 Energetics

As for the energetics, DFT total energy calculations are performed on 170 structures selected from the $T = 1,123$K thermodynamic ensemble over the full range of composition. The formation energies are also calculated using the *valence loop rule* (i.e. the measure of energy $E = \alpha \sum_{I,J} v_{IJ}^2$). The results are shown in Fig. 4.10. The fitted parameter $\alpha = 1.07$ is consistent with that of Ref. [22]. The power of BVM is shown by the accurate reproduction of the energetics. However, BVM fails to reproduce the ordered superlattice $(GaN)_1(ZnO)_1$ ground state at $x = 0.5$[2], possibly due to the nearest-neighbor short-range nature of BVM itself, i.e. the wurtzite and zincblende structures are indistinguishable from one another in BVM).

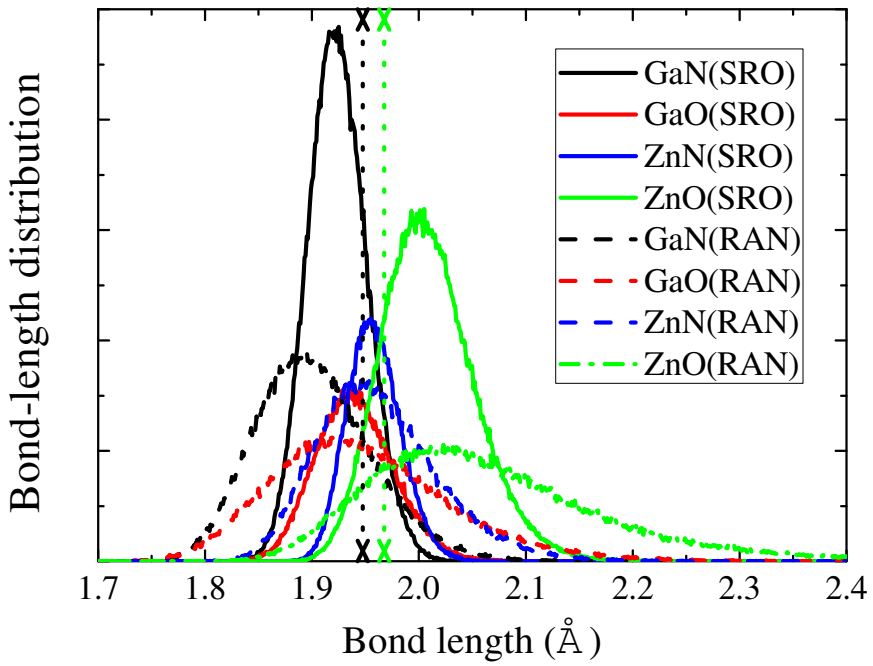

Figure 4.7: Bond-length distributions of short-range ordered alloy and random alloy at $x = 0.5$. The vertical dotted lines mark the bond lengths of the corresponding compounds.

The formation energy of $(GaN)_1(ZnO)_1$ predicted by BVM is positive, while that predicted by DFT is slightly negative[2]. The discrepancy should not affect any conclusion drawn in present study since only the disordered phase is concerned.

Inclusion of vibrational entropy in the first-principles alloy phase diagram calculation is a long-standing challenge. The main difficulty lies in the conflict between the requirement for a large supercell and the expensive computational cost associated with it. The problem is partly alleviated by the SQS approach[43, 77, 76]. Another idea is to use bond-length-dependent transferable force constant[24, 78], where the bond stiffness is predicted from the bond length and the chemical identity of the bond. The present study reveals the strong correlation between bond valence and bond length, which indicates the possibility of using bond valence instead of bond length as a predictor for bond stiffness. Such extension will release the estimation of

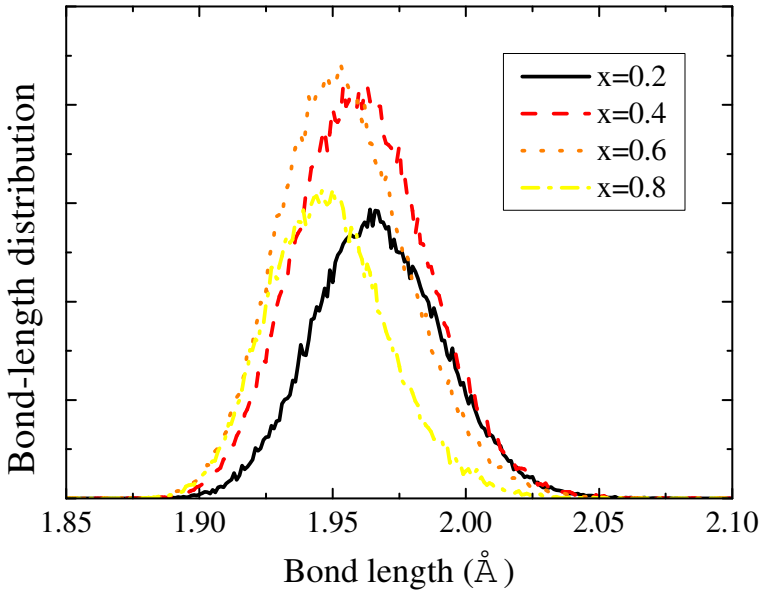

Figure 4.8: Zn-N bond-length distribution at various ZnO content.

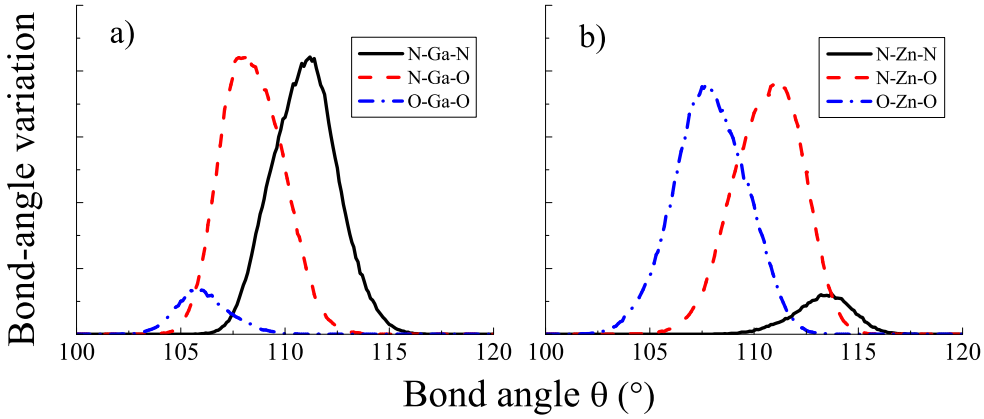

Figure 4.9: The anion-cation-anion bond-angle variation of short-range ordered alloy at $x = 0.5$.

nearest-neighbor force constants from the requirement for the knowledge of the relaxed geometry of a configuration. Fig. 4.11 shows the dependence of stretching bond stiffness $\phi^{II}_{\alpha\alpha}$ and $\phi^{IJ}_{\alpha\alpha}$ on bond length, where α refers to the bond-stretching direction and I, J are nearest neighbors. The bond stiffness calculations are performed on selected 72-atom supercells with a displace-

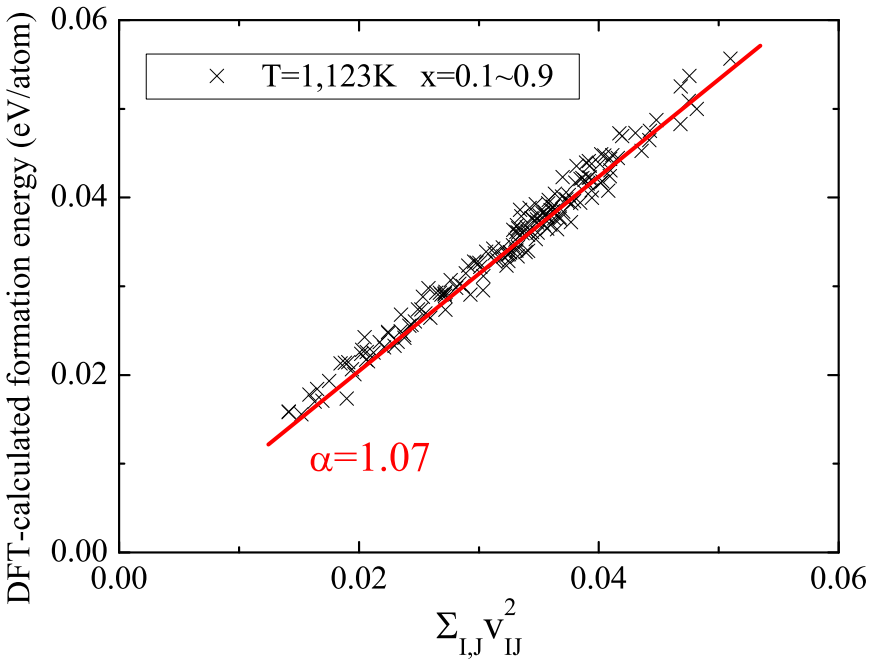

Figure 4.10: Comparison of DFT-calculated formation energies with BVM-predicted formation energies.

ment of 0.02$\mathring{A}$ from the relaxed atomic coordinates along each bond direction. While a linear bond stiffness vs bond length relationship is suggested in bond-length-dependent transferable force constant approach[24, 78], an exponential correlation (similar with that between bond valence and bond length) seems to fit better according to the present study, which is consistent with the interpretation that bond valence measures bond strength. Bond stiffness depends on bond length in a similar manner, regardless of the chemical identity of the bond. The most covalent Ga-N bond is the stiffest, while the most ionic Zn-O bond is the softest.

For isovalent III-V semiconductor alloys, the widely used Keating's valence force field (KVFF) model[79] yields generally good accuracy[80, 81, 82, 83, 84, 16]. In KVFF model the force constants are related to the macroscopic elastic constants and therefore can be accurately determined experimentally. Also the isovalent nature of III-V semiconductor alloys guarantees good transferability from compound semiconductors to the corresponding alloy. For

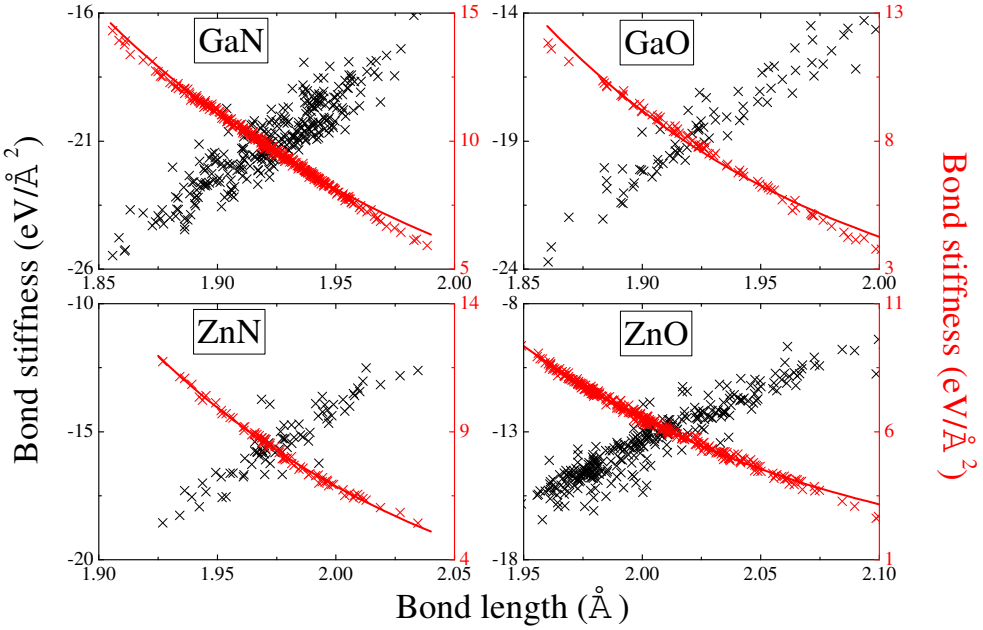

Figure 4.11: Correlation between stretching bond stiffness and bond length. $\phi^{II}_{\alpha\alpha}$ is shown in black, and $\phi^{IJ}_{\alpha\alpha}$ is shown in red.

non-isovalent semiconductor alloys, the transferability no longer holds, for the apparent reason that there exists no wurtzite GaO or ZnN. The present study offers an alternative way of accurately reproducing the energetics of non-isovalent semiconductor alloys with BVM, where only site occupancies are needed. The non-isovalent nature is well captured by the *valence sum rule*. An extension of BVM derives naturally to the modelling of an atomistic potential. In present study, the relaxation energy is assumed to consist of three parts:

$$E_{relax} = \alpha \sum_{I,J} v_{IJ}^2 + \sum_{\mathrm{I=Ga,Zn}} k_I \sum_{J_1,J_2} (\theta_{J_1 I J_2} - \theta_0)^2 + \sum_{\mathrm{I=N,O}} \beta_I \left(\sum_J v_{IJ} - V_{0,I} \right)^2 \tag{4.4}$$

The first term is simply the *valence loop rule*, and the second term is the harmonic angle potential. The third term accounts for large lattice relaxations by penalizing deviations from the bond valence conservation and is important for reliable molecular dynamics simulations[18, 19]. In the fitting procedure each relaxed structure is expanded and contracted by 1%. Fitting

parameters $k_{\mathrm{N,O}}$ and $\beta_{\mathrm{Ga,Zn}}$ are found to be negligible. In Figure 4.12 the comparison between DFT-calculated and BVM-fitted formation energies is shown. The agreement is generally satisfactory. Further studies will involve refinement of the atomistic potential, and anharmonicity effect within quasi-harmonic approximation.

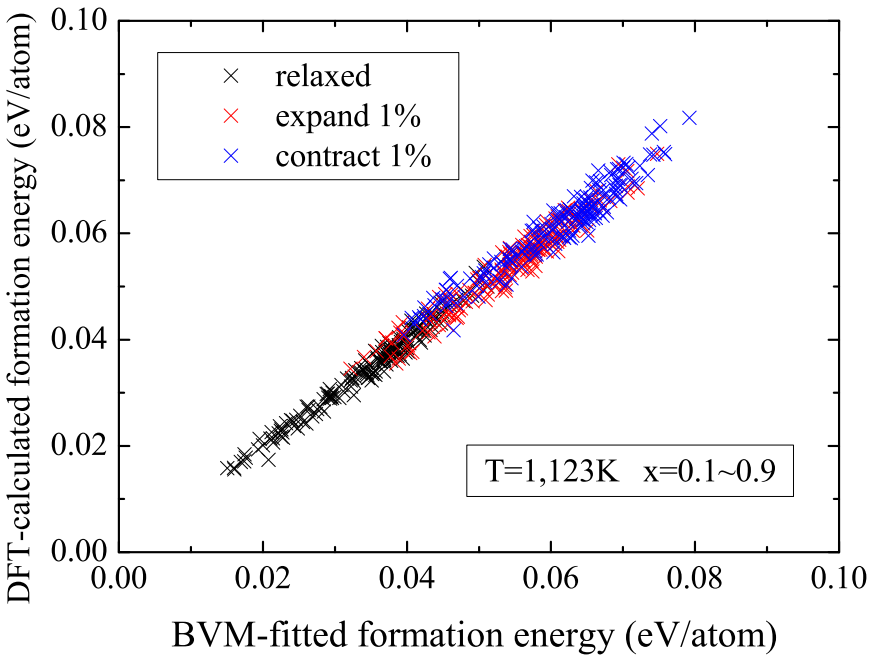

Figure 4.12: Comparison between DFT-calculated and BVM-fitted formation energies.

4.5 Conclusion

A physical interpretation of BVM is discussed from the computational perspective. The underlying assumptions and correlations within BVM are revealed by DFT calculations on the non-isovalent semiconductor alloy $(\mathrm{GaN})_{1-x}(\mathrm{ZnO})_x$. Bond-length distribution and bond-angle variation are predicted by parameter-fitting BVM empirical correlations to reliable DFT-calculated structural data.

The unusual relaxations associated with the non-isovalent nature of the alloy are explained in the language of BVM. Effects of SRO on bond-length distribution and bond-angle variation are also discussed. The energetics is accurately reproduced by BVM. The connection between bond valence and stretching bond-length-dependent transferable force constant is revealed. A tentative improved bond valence potential is proposed. In principle, discussions in the present study should also be applicable for other non-isovalent semiconductor alloys.

Chapter 5

5 Pyroelectricity: Theory and Calculation

5.1 Pyroelectric theory

Crystals have specific free parameters that can vary without altering symmetry. These are external strains and internal strains. The external strains are components of the strain tensor $\epsilon_{\alpha\beta}$ that have full crystalline symmetry ($\Delta V/V$ if cubic, or $\Delta a/a$ and $\Delta c/c$ if hexagonal like wurtzite.) The external strains will be denoted ϵ_i. The internal strains describe degrees of freedom of atoms in the unit cell. An example is the c-axis cation-anion spacing denoted uc in wurtzite, where u is typically close to the "ideal" value 3/8 of perfect stacked tetrahedra, a value not required by symmetry. The internal strains will be denoted u_i. Wurtzite is the highest symmetry structure that can have spontaneous polarization, and has the minimal number of 2 external strains and 1 internal. The polarization is strongly affected by the internal strain[85] u, and pyroelectricity is closely related to its temperature shift du/dT.

It is conventional to separate the total (constant stress, σ) pyroelectric coefficient $p_\sigma(T)$ into two parts[8, 86]: the primary (constant strain, ϵ) $p_\epsilon(T)$ and the secondary $p_2(T)$

$$p_\sigma(T) = \left(\frac{dP_s}{dT}\right)_\sigma = \left(\frac{\partial P_s}{\partial T}\right)_\epsilon + \sum_i \left(\frac{\partial P_s}{\partial \epsilon_i}\right)_T \left(\frac{\partial \epsilon_i}{\partial T}\right)_\sigma = p_\epsilon(T) + p_2(T). \quad (5.1)$$

where $p_\epsilon(T)$ measures the "clamped-lattice" pyroelectricity while $p_2(T)$ accounts for "thermal expansion" pyroelectricity. Here we simplify the notation by assuming that polarization $\vec{P} = P\hat{z}$ occurs along a unique axis. The label z for this axis is dropped when unnecessary. The primary part, $p_\epsilon(T)$, is the "clamped-lattice" pyroelectricity, where external strains are held fixed, but internal strains relax thermally. The secondary part $p_2(T)$ accounts for the changes that occur when external strains are allowed to develop.

Harmonic vibrational normal modes are labeled by $(\vec{q}\lambda)$, wavevector and

branch index. The $\vec{q} = 0$ normal modes of A_1 symmetry (invariant under all point-group operations), labeled $(\vec{0}j)$, are dynamic versions of the internal strains u_j. Lattice anharmonicity allows the amplitudes $Q_{\vec{0}j}$ of these modes to develop static thermal and zero-point internal strains $\langle Q_{\vec{0}j}(T)\rangle$. This is one source of pyroelectric thermal shifts of P_s. The other normal modes $\vec{q}\lambda$ have no allowed first order static effect ($\langle Q_{\vec{q}\lambda}\rangle = 0$), but their second order static mean square amplitude $\langle Q_{\vec{q}\lambda}Q_{-\vec{q}\lambda}\rangle$ increases with T in harmonic approximation. These cause electron-phonon thermal renormalization of P_s even in the absence of internal and external strains, a second source of pyroelectricity. Both effects are mentioned by Born [8] and Szigeti [86]. After Szigeti's work, the electron-phonon part has been generally discounted as less important, and will be ignored in our work. Then to first approximation, the temperature-dependent spontaneous polarization $P_s(T)$ varies linearly with internal strain. To first-order approximation, the temperature-dependent primary spontaneous polarization $P_s(T)$ can be expanded in terms of atomic displacement as

$$P_{s,\epsilon}(T) = P_{s,\epsilon}(0) + \sum_{\kappa\alpha} \frac{\partial P_{s,\epsilon}}{\partial u_{\kappa\alpha}} u_{\kappa\alpha}(\vec{0}j) \tag{5.2}$$

$\vec{0}j$ is the active phonon mode in the long-wavelength limit. In wurtzite, the structure considered in this paper, there is only one relevant mode, the $A_1(TO)$ mode, with opposite displacements $\vec{u}_{\kappa\alpha}$ of anions and cations along the polar c or $\hat{z}$ axis. The connection between static displacement $\langle \vec{u}_\kappa \rangle$ of atom κ in each cell, and normal mode amplitude $\langle Q_{\vec{0}j}\rangle$ is

$$\langle u_{\kappa z}\rangle = \sum_j \langle Q_{\vec{0}j}\rangle \epsilon_{\vec{0}j}(\kappa z)/\sqrt{M_\kappa} \tag{5.3}$$

In the long-wavelength limit $\frac{\partial P_s}{\partial u_{\kappa\alpha}}$ yields the Born effective charge $eZ^{s\alpha}_\kappa$ per unit-cell volume Ω, whose magnitude governs the zone-center LO/TO splitting[50]. The pyroelectric theory of Born [8] and Szigeti [86] recognizes two kinds of contributions to the primary pyroelectric coefficient, a non-rigid term caused by electron-phonon interaction and a rigid term caused by anharmonic internal displacement. Schematically,

$$p_\epsilon(T) = \frac{e}{\Omega}\left[\frac{dZ^*}{dT}u + Z^*\frac{du}{dT}\right]. \tag{5.4}$$

Born and Szigeti present different-looking formulas for the second term. We find that they are equivalent. Neither Born nor Szigeti examines the first term in much detail, but they disagree about whether its power law is T or T^3 at low T. It is clear to all that the second term follows a specfic heat T^3 form. Born cites experimental evidence for $p \propto T$, and therefore favors the first term. More recent evidence (for example, Heiland and Ibach[87] for ZnO) indicates $p \propto T^3$ at low T. It is now generally believed that the second term in Eq.(5.5) dominates. An interesting experiment on ZnO by Albertsson *et al.* [88] measures the internal parameter shift du/dT directly. They find that the second term in Eq.(5.5) matches $p_\sigma(T)$ provided $Z^* = 0.2$ is used. We believe that they have mis-defined Z^* and that the correct definition makes the empirical Z^* larger by 4, or $Z^* = 0.8$. Our results presented below are the first microscopic calculations of thermal shift of internal parameters. Our results for du/dT are smaller than the Albertsson experiment by ≈ 2, and our computed $Z^* = 2.2$ is larger (agreeing with all modern calculations). We are not able to identify the source of the discrepancy, but our results also indicate that the second term dominates. The primary pyroelectric coefficient is then given by

$$p_\beta(T) = \frac{e}{\Omega} \sum_{j,\kappa\alpha} Z_\kappa^{\beta\alpha} \frac{du_{\kappa\alpha}(\vec{0}j)}{dT}. \tag{5.5}$$

This ignores the electron-phonon term. In wurtzite, it simplifies to $p(T) = (2e/\Omega)Z^* d(uc)/dT$, where Z^* is the Born effective charge of the cation (the anion's is opposite by definition), and the factor of 2 recognizes the two molecules per unit cell.

Following Szigeti's derivation[86], the temperature-dependent spontaneous polarization $P_s(T)$ can be expanded in terms of atomic displacement as

$$P_s(T) = P_s(0) + \sum_{\vec{q}\lambda} \frac{\partial P_s}{\partial Q_{\vec{q}\lambda}} Q_{\vec{q}\lambda} + \sum_{\vec{q}\lambda\vec{q}'\lambda'} \frac{\partial^2 P_s}{\partial Q_{\vec{q}\lambda} \partial Q_{\vec{q}'\lambda'}} Q_{\vec{q}\lambda} Q_{\vec{q}'\lambda'} \tag{5.6}$$

where $P_s(0)$ is the spontaneous polarization at $T = 0K$. Under the rigid-ion approximation the second-order expansion term is neglected since the electron cloud follows the ion rigidly without deformation. The atomic displacement is written in terms of the phonon creation and annihilation operators

$$u_{\kappa\alpha}^l = \sum_{\vec{q}\lambda} \sqrt{\frac{\hbar}{2M_\kappa \omega_{\vec{q}\lambda}}} [\hat{a}_{\vec{q}\lambda} + \hat{a}_{-\vec{q}\lambda}^+] \epsilon_{\kappa\alpha}(\vec{q}\lambda) e^{i\vec{q}\cdot\vec{R}_l} \tag{5.7}$$

Only the zone-center phonon term is left after taking the thermodynamic average. The primary pyroelectric coefficient then reads

$$p_\beta(T) = \sum_{j,\kappa\alpha} \frac{eZ_\kappa^{\beta\alpha}}{\Omega} \frac{\partial \langle u_{\kappa\alpha}(\vec{0}j)\rangle}{\partial T} \tag{5.8}$$

In order to evaluate the mean displacement, the potential energy is expanded in terms of atomic displacement to third order

$$V^{(3)} = \frac{1}{3!} \sum_{\vec{q}\vec{q}'\vec{q}''jj'j''} V_3 \begin{pmatrix} \vec{q} & \vec{q}' & \vec{q}'' \\ j & j' & j'' \end{pmatrix} (\hat{a}_{\vec{q}j} + \hat{a}^+_{-\vec{q}j})(\hat{a}_{\vec{q}'j'} + \hat{a}^+_{-\vec{q}'j'})(\hat{a}_{\vec{q}''j''} + \hat{a}^+_{-\vec{q}''j''}) \tag{5.9}$$

Treating the cubic anharmonicity as a perturbation, the perturbed phonon wavefunction reads

$$\phi^{(1)}_{\tilde{n}} = \phi^{(0)}_{\tilde{n}} + \sum_{\tilde{n}'} \frac{\langle \tilde{n}'^{(0)} | V^{(3)} | \tilde{n}^{(0)} \rangle}{E^{(0)}_{\tilde{n}} - E^{(0)}_{\tilde{n}'}} \phi^{(0)}_{\tilde{n}'} \tag{5.10}$$

The atomic displacement is then

$$\langle Q_{\vec{0}j} \rangle = \frac{2 \sum_{\tilde{n}} e^{-\beta(n+\frac{1}{2})\hbar\omega} \sum_{\tilde{n}'} \frac{\langle \tilde{n}^{(0)} | Q_{\vec{0}j} | \tilde{n}'^{(0)} \rangle \langle \tilde{n}'^{(0)} | V^{(3)} | \tilde{n}^{(0)} \rangle}{E^{(0)}_{\tilde{n}} - E^{(0)}_{\tilde{n}'}}}{\sum_{\tilde{n}} e^{-\beta(n+\frac{1}{2})\hbar\omega}} \tag{5.11}$$

The first Dirac bracket is non-zero only for $\tilde{n}' = \tilde{n} \pm 1$. Therefore the second Dirac bracket reduces to terms containing $\hat{a}_{\vec{0}j}\hat{a}_{\vec{q}\lambda}\hat{a}^+_{-\vec{q}\lambda}$, $\hat{a}_{\vec{0}j}\hat{a}^+_{\vec{q}\lambda}\hat{a}_{-\vec{q}\lambda}$, $\hat{a}^+_{\vec{0}j}\hat{a}_{\vec{q}\lambda}\hat{a}^+_{-\vec{q}\lambda}$ and $\hat{a}^+_{\vec{0}j}\hat{a}^+_{\vec{q}\lambda}\hat{a}_{-\vec{q}\lambda}$.

$$\langle Q_{\vec{0}j} \rangle = -\sum_{\vec{q}\lambda} \frac{2n_{\vec{q}\lambda} + 1}{\hbar\omega_{\vec{0}j}} Q_{\vec{0}j} V_3 \begin{pmatrix} \vec{0} & \vec{q} & -\vec{q} \\ j & \lambda & \lambda \end{pmatrix} \tag{5.12}$$

More specifically

$$\langle u_{\kappa\alpha}(\vec{0}j) \rangle = -\sum_{\vec{q}\lambda} \frac{2n_{\vec{q}\lambda} + 1}{\hbar\omega_{\vec{0}j}} \sqrt{\frac{\hbar}{2M_\kappa \omega_{\vec{0}j}}} \epsilon_{\kappa\alpha}(\vec{0}j) V_3 \begin{pmatrix} \vec{0} & \vec{q} & -\vec{q} \\ j & \lambda & \lambda \end{pmatrix} \tag{5.13}$$

where the anharmonic coefficient V is given by the third derivative of the total energy with respect to the atomic displacement as

$$V_3\begin{pmatrix} \vec{0} & \vec{q} & -\vec{q} \\ j & \lambda & \lambda' \end{pmatrix} = \sum_{\kappa_0\kappa_1\kappa_2,\alpha_0\alpha_1\alpha_2} \sqrt{\frac{\hbar^3}{8M_{\kappa_0}M_{\kappa_1}M_{\kappa_2}\omega_{\vec{0}j}\omega_{\vec{q}\lambda}\omega_{-\vec{q}\lambda'}}}\cdot$$
$$\epsilon_{\kappa_0\alpha_0}(\vec{0}j)\epsilon_{\kappa_1\alpha_1}(\vec{q}\lambda)\epsilon_{\kappa_2\alpha_2}(-\vec{q}\lambda')\left(\sum_{l_1l_2}\frac{\partial^3 E}{\partial u^{l_0}_{\kappa_0\alpha_0}\partial u^{l_1}_{\kappa_1\alpha_1}\partial u^{l_2}_{\kappa_2\alpha_2}}e^{i\vec{q}\cdot\left(\tau_{l_1}-\tau_{l_2}\right)}\right) \tag{5.14}$$

The third-order anharmonic coefficient $V(\vec{0}j,\vec{q}\lambda,-\vec{q}\lambda')$ can also be obtained from the derivative of the dynamical matrix $D_{\alpha_1\alpha_2}(\kappa_1\kappa_2,\vec{q})$ with respect to the displacement pattern $Q_{\vec{0}j}$ as

$$V_3\begin{pmatrix} \vec{0} & \vec{q} & -\vec{q} \\ j & \lambda & \lambda' \end{pmatrix} =\sqrt{\frac{\hbar^3}{8\omega_{\vec{0}j}\omega_{\vec{q}\lambda}\omega_{-\vec{q}\lambda'}}}\sum_{\kappa_1\kappa_2,\alpha_1\alpha_2}\epsilon_{\kappa_1\alpha_1}(\vec{q}\lambda)\epsilon_{\kappa_2\alpha_2}(-\vec{q}\lambda')\cdot$$
$$\left(\frac{\partial}{\partial Q_{\vec{0}j}}\sum_{l_1l_2}\frac{1}{\sqrt{M_{\kappa_1}M_{\kappa_2}}}\frac{\partial^2 E}{\partial u^{l_1}_{\kappa_1\alpha_1}\partial u^{l_2}_{\kappa_2\alpha_2}}e^{i\vec{q}\cdot\left(\tau_{l_1}-\tau_{l_2}\right)}\right) \tag{5.15}$$

Through the diagonalization of the dynamical matrix $D_{\alpha_1\alpha_2}(\kappa_1\kappa_2,\vec{q})$ we have

$$\sum_{\kappa_1\kappa_2,\alpha_1\alpha_2}\epsilon_{\kappa_1\alpha_1}(\vec{q}\lambda)\left(\sum_{l_1l_2}\frac{1}{\sqrt{M_{\kappa_1}M_{\kappa_2}}}\frac{\partial^2 E}{\partial u^{l_1}_{\kappa_1\alpha_1}\partial u^{l_2}_{\kappa_2\alpha_2}}e^{i\vec{q}\cdot\left(\tau_{l_1}-\tau_{l_2}\right)}\right)\epsilon_{\kappa_2\alpha_2}(-\vec{q}\lambda')$$
$$=\omega^2_{\vec{q}\lambda}\delta_{\lambda\lambda'} \tag{5.16}$$

The relation between the third-order anharmonic coefficients $V_3(0j,\vec{q}\lambda,-\vec{q}\lambda)$ and the "internal Grüneisen parameter" reads

$$V_3\begin{pmatrix} \vec{0} & \vec{q} & -\vec{q} \\ j & \lambda & \lambda \end{pmatrix} =\sqrt{\frac{\hbar^3}{8\omega_{\vec{0}j}\omega_{\vec{q}\lambda}\omega_{-\vec{q}\lambda}}}\frac{\partial\omega^2_{\vec{q}\lambda}}{\partial Q_{\vec{0}j}} = -\left(\frac{\hbar}{2\omega_{\vec{0}j}}\right)^{1/2}\frac{\hbar\omega_{\vec{q}\lambda}}{2Q_{\vec{0}j}}\gamma_{\vec{q}\lambda}(\vec{0}j) \tag{5.17}$$

The temperature-dependent atomic displacement eventually reduces to

$$\langle Q_{\vec{0}j}\rangle = -\sum_{\vec{q}\lambda}\frac{\hbar}{2}\frac{2n_{\vec{q}\lambda}+1}{\omega^2_{\vec{0}j}}\frac{\partial\omega_{\vec{q}\lambda}}{\partial Q_{\vec{0}j}} \tag{5.18}$$

Equivalently, under the "clamped-lattice" condition, the Born-Oppenheimer potential energy is harmonic with respect to $u_{\kappa\alpha}(\vec{0}j)$:

$$U_{BO} = U_0 + \frac{1}{2}\omega_{\vec{0}j}^2 Q_{\vec{0}j}^2 \tag{5.19}$$

where $Q_{\vec{0}j}$ is the normal coordinate $\sqrt{\sum_{\kappa\alpha} M_\kappa u_{\kappa\alpha}^2(\vec{0}j)}$, and $u_{\kappa\alpha}$ is the atomic displacement of κth atom in α-direction. The Helmholtz free energy reads

$$F = U_{BO} + k_B T \sum_{\vec{q}\lambda} \ln\left(2\sinh\frac{\hbar\omega_{\vec{q}\lambda}}{2k_B T}\right) \tag{5.20}$$

The temperature-dependent atomic displacement $u_{\kappa\alpha}(\vec{0}j)$ shall minimize the Helmholtz free energy F. We then have

$$\omega_{\vec{0}j}^2 Q_{\vec{0}j} = -\sum_{\vec{q}\lambda} \frac{\hbar}{2}\left(2n_{\vec{q}\lambda}+1\right)\frac{\partial\omega_{\vec{q}\lambda}}{\partial Q_{\vec{0}j}} \tag{5.21}$$

Finally, the primary pyroelectric coefficient reads

$$p_{\epsilon,\beta}(T) = \sum_{\kappa\alpha}\sum_{\vec{0}j}\sum_{\vec{q}\lambda} \frac{Z_\kappa^{\beta\alpha}}{\Omega}\frac{2}{\hbar\omega_{\vec{0}j}}\sqrt{\frac{\hbar}{2M_\kappa\omega_{\vec{0}j}}}\epsilon_{\kappa\alpha}(\vec{0}j)V_3\begin{pmatrix}\vec{0} & \vec{q} & -\vec{q}\\ j & \lambda & \lambda\end{pmatrix}\frac{\partial(2n_{\vec{q}\lambda}+1)}{\partial T} \tag{5.22}$$

where β labels the direction of the spontaneous polarization, and V_3 is the third-order anharmonic coefficient for the active mode $\vec{0}j$. $\vec{q}\lambda$ runs over all phonon branches λ in the entire Brillouin zone. The "internal" Grüneisen parameter is defined as $\gamma_{\vec{q}\lambda}(\vec{0}j) = -d\log\omega_{\vec{q}\lambda}/d\log Q_{\vec{0}j}$. This measures the shift of phonon frequency $\omega_{\vec{q}\lambda}$ per unit change in the amplitude $Q_{\vec{0}j}$ of the active mode. It has been defined previously by Gibbons[89]. In wurtzite structure, the active A_1 mode is split. When $\vec{q}$ approaches 0 along the c or $\hat{z}$ axis, it is a high frequency longitudinal branch denoted A_1(LO). When $\vec{q}$ approaches 0 along lines in the xy plane, it is an intermediate frequency transverse branch labeled A_1(TO). The rule is to use the TO frequency, which corresponds to a pyroelectric distortion in zero electric field. In this work we only address the "rigid" primary pyroelectricity arising from atomic anharmonic displacements. The influence of external strains (the "secondary" effect) will be added later using measured external strains $\epsilon_i(T)$ and computed piezoelectric coefficients. The challenge of the "non-rigid" electron-phonon interaction

part, which give rises to the temperature dependence of the Born effective charges, is left open.

5.2 Pyroelectricity of GaN and ZnO

Electronic structure calculations are performed within the local density approximation (LDA)[48] using the QUANTUM ESPRESSO package[56]. We use norm-conserving Martin-Troulliers pseudopotentials[90] in our calculations. The electronic wave-functions are expanded in a plane-wave basis with a kinetic energy cutoff of 180 Ry. Ga-3d and Zn-3d states are treated explicitly as valence states. We use a $6 \times 6 \times 4$ k-point mesh for Brillouin-zone sampling. Phonons are calculated using density-functional perturbation theory (DFPT)[50]. The third-order anharmonic coefficients $V_3(0j, \vec{q}\lambda, -\vec{q}\lambda)$ are computed on an $8 \times 8 \times 6$ q-point mesh through the finite difference of the dynamical matrix by displacing atoms along the displacement pattern $u_{\kappa\alpha}(\vec{0}j)$. The quasiharmonic internal shift $\langle Q_{\vec{0}j} \rangle$, derived from the "internal" Grüneisen parameter $\gamma_{\vec{q}\lambda}(\vec{0}j)$, involves only diagonal components ($\vec{q}\lambda = -\vec{q}\lambda'$). The secondary pyroelectric coefficient is calculated from the linear thermal expansion coefficients and the piezoelectric constants.

Computed properties of GaN and ZnO are summarized in Table 5.1. In harmonic approximation, the mean displacement of an atom is zero (the mean position coincides with the equilibrium position). Inclusion of the third-order anharmonicity causes the mean displacement of cations and anions to deviate along the polar c-axis in opposite directions. The Born effective charges on cations and anions are equal and opposite. The net effect is a temperature-dependent shift of the spontaneous polarization. In Figs. 5.1-5.2 we show the calculated primary pyroelectric coefficients $p_\epsilon(T)$ and the experimental total pyroelectric coefficient $p_\sigma(T)$ for GaN[29, 30] and ZnO[87] respectively. The secondary pyroelectric coefficients $p_2(T)$ are calculated from $2e_{31}\alpha_1 + e_{33}\alpha_3$ using the experimental linear thermal expansion coefficients α_1, α_3[91] and the calculated piezoelectric stress constants e_{31}, e_{33}[7]. However, it is reported that for GaN and ZnO the computed piezoelectric constants are uncertain by as much as 30%[92, 93]. Therefore the calculated $p_2(T)$ shown in Figs. 5.1-5.2 should be considered rough estimates. As shown in Figs. 5.1-5.2, for GaN

Table 5.1: The calculated lattice constants, Born effective charge and long-wavelength A_1(TO) phonon frequency for GaN and ZnO. Experimental values are shown in parentheses except for Born effective charge where theoretical values are shown instead.

	a(Å)	c(Å)	$Z^{33}(e)$	$\omega_{TO}(\mathrm{cm}^{-1})$
GaN	3.182 (3.187[1])	5.189 (5.186[1])	2.77 (2.72[2])	534 (533.8[3])
ZnO	3.219 (3.25[1])	5.195 (5.207[1])	2.28 (2.11[2])	390 (378[4])

[1]Ref. [91], X-ray powder diffractometry at 300K.
[2]Ref. [7], first-principles calculations in the local density approximation.
[3]Ref. [94], Raman spectra at 6K.
[4]Ref. [95], inelastic neutron scattering spectra at 10K.

and ZnO above room temperature the secondary pyroelectric effect is comparable with the primary effect. This differs from ferroelectric pyroelectrics, where the primary pyroelectricity dominates[31]. For GaN, disagreement in the experimentally measured pyroelectric coefficients is reported[29, 30], possibly due to the piezoelectric contribution from the strain introduced by the substrates. For ZnO, our calculated total pyroelectricity is about 20% lower than the experimental data, indicating the possible contribution from the electron-phonon interaction term, which is left out in our first-principles calculations.

Yan *et al*. conjecture a temperature dependence of the primary pyroelectric coefficient $p_\epsilon(T)$ of GaN as a sum of Debye and Einstein functions[96]. In Fig. 5.3 we show for ZnO our calculated contributions from acoustic and optic branches respectively. At low temperatures, only the acoustic phonon modes are sufficiently excited, while at high temperatures, contributions from the optic phonon modes become important. Our calculations indicate that for wurtzite ZnO, contributions from acoustic and optic branches are more complicated than Debye and Einstein functions, especially at low temperatures. In Fig. 5.4, we show for ZnO the vibrational density of states $D(\omega)$, together with the frequency-distributed internal Grüneisen parameter $\gamma_u(\omega)$ defined as

$$\gamma_u(\omega)D(\omega) = \sum_{\vec{q}\lambda} \gamma_{\vec{q}\lambda}(\vec{0}j)\delta(\omega - \omega_{\vec{q}\lambda}). \tag{5.23}$$

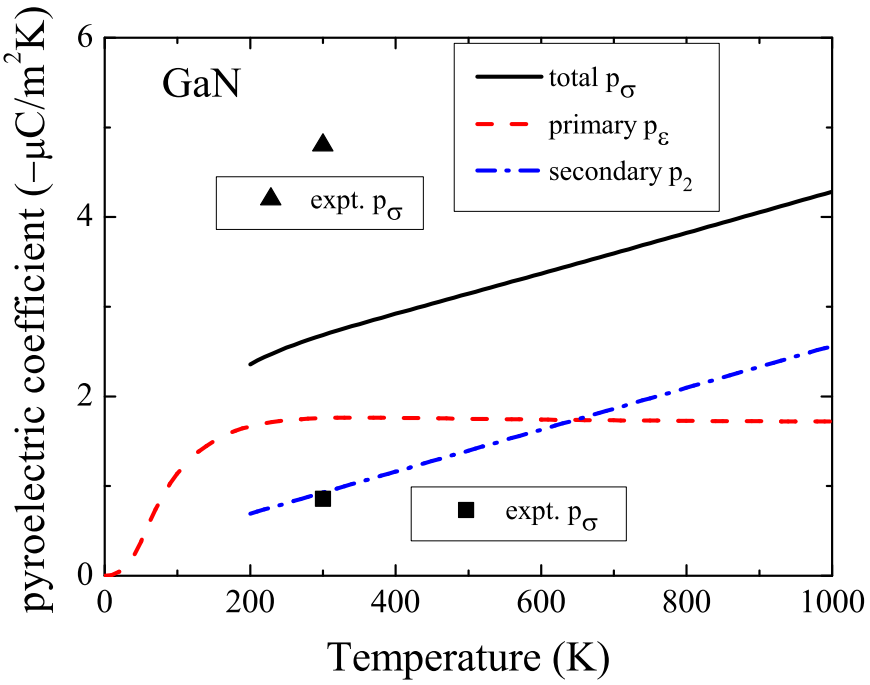

Figure 5.1: The pyroelectric coefficient of GaN.

As an example of the use of this definition, the pyroelectric coefficient is

$$p(T) = \frac{eZ^*}{2M_{\rm red}\omega_0^2 cu} \iint_0^\infty d\omega D(\omega)\gamma(\omega)C(\omega), \tag{5.24}$$

where $C(\omega)$ is the harmonic specific heat of a mode of frequency ω, $\hbar\omega(dn/dT)/\Omega$. The total contribution to $p(T)$ is a complicated mix of contributions of both signs from acoustic and optic branches.

Figure 5.5 shows the predicted and the experimentally measured values of the internal parameter u of ZnO. The theory for pyroelectricity also generates a formula for the internal strain $u(T)$ which is closely parallel to the Grüneisen quasiharmonic theory of volume expansion,

$$\frac{\Delta u}{u} = \frac{1}{2M_{\rm red}\omega_0^2 c^2 u^2} \sum_{\vec{q}j} \left(n_{\vec{q}j} + \frac{1}{2} \right) \hbar\omega_{\vec{q}j}\gamma_{\vec{q}j}(0) \tag{5.25}$$

where the label 0 on ω_0 and $\gamma_{\vec{Q}j}(0)$ indicates the A_1(TO) mode. This formula gives only the part of $u(T)$ that occurs when external strains are absent. The

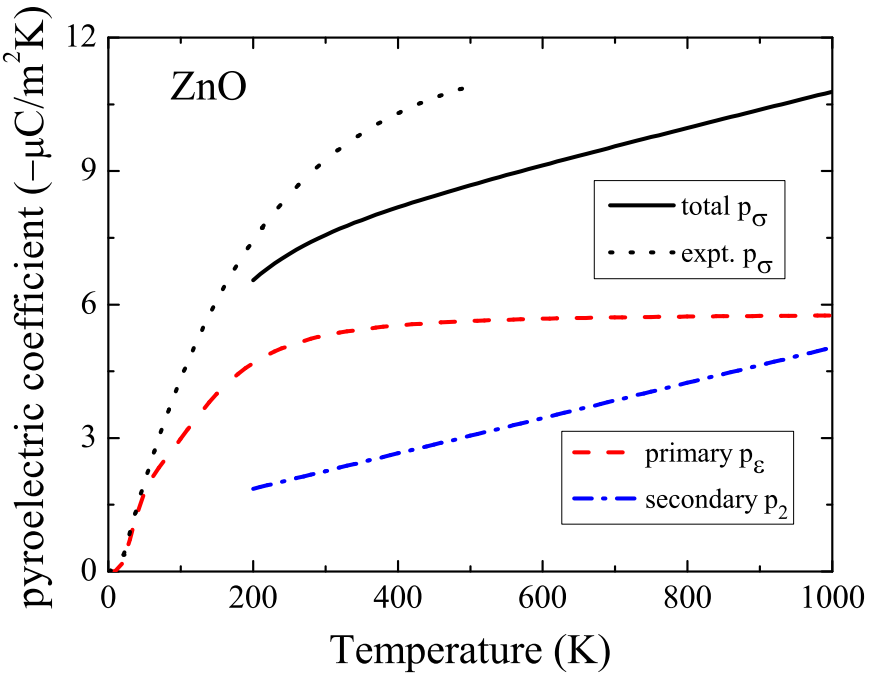

Figure 5.2: The pyroelectric coefficient of ZnO.

full result is

$$u(T) = u(0)+[\Delta u(T)-\Delta u(0)]+\left(\frac{\partial u}{\partial a}\right)_{\rm BO}[a(T)-a(0)]+\left(\frac{\partial u}{\partial c}\right)_{\rm BO}[c(T)-c(0)] \tag{5.26}$$

The value $u(0)$ from experiment contains all zero-point shifts. The factor $[\Delta u(T) - \Delta u(0)]$ comes from the theory of Eq.(5.25), and the factors $[a(T) - a(0)]$ and $[c(T) - c(0)]$ come from experiment [91]. For ZnO, the theoretical values of $\partial u/\partial a$ and $\partial u/\partial c$ are $0.083\mathring{A}^{-1}$ and $-0.051\mathring{A}^{-1}$ respectively, coming from our DFT Born-Oppenheimer calculations. Our calculated thermal displacement increases monotonically with increasing temperature, while experimentally $u(T)$ remains unchanged between 20 and 300 K. Except for this discrepancy at low-T, the overall agreement is satisfactory.

We also calculate the pyroelectric coefficients for AlN, BeO and CdS, as shown in Figs. 5.6-5.8. While for GaN and ZnO the secondary effect becomes important only at high-T, for AlN and BeO the primary effect completely dominates. There is also disagreement found in the experimentally mea-

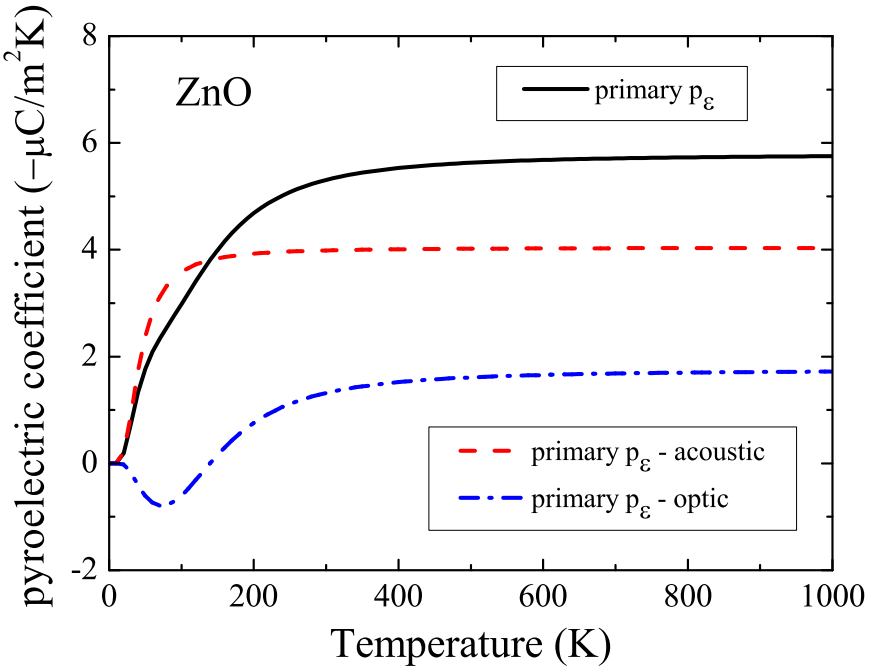

Figure 5.3: The primary pyroelectric coefficient of ZnO: acoustic and optic branches.

sured pyroelectric coefficients for AlN[99, 100]. For AlN, the uncertainty in the computed piezoelectric constants is about 20%[92, 7]. For BeO, the piezoelectric constants e_{31} and e_{33} are predicted to be -0.02 and 0.02 respectively from the calculation of Bernardini *et al.*[7], while a subsequent comparative calculation predicts -0.3 and 0.55 otherwise. The large sensitivity in the piezoelectric tensor results in a large uncertainty in the calculated secondary effect. Accurate piezoelectric constants are needed before we could come to a reliable calculation of the secondary pyroelectricity.

5.3 Raman linewidth of A_1(TO) phonon

The last subsection of this chapter is devoted to a preliminary first-principles study on the Raman linewidth of A_1(TO) phonon in III-V/II-VI wurtzite semiconductors. Through the anharmonic three-phonon process, the zone-center A_1(TO) phonon $\vec{0}j$ decays into two phonons with opposite wave vec-

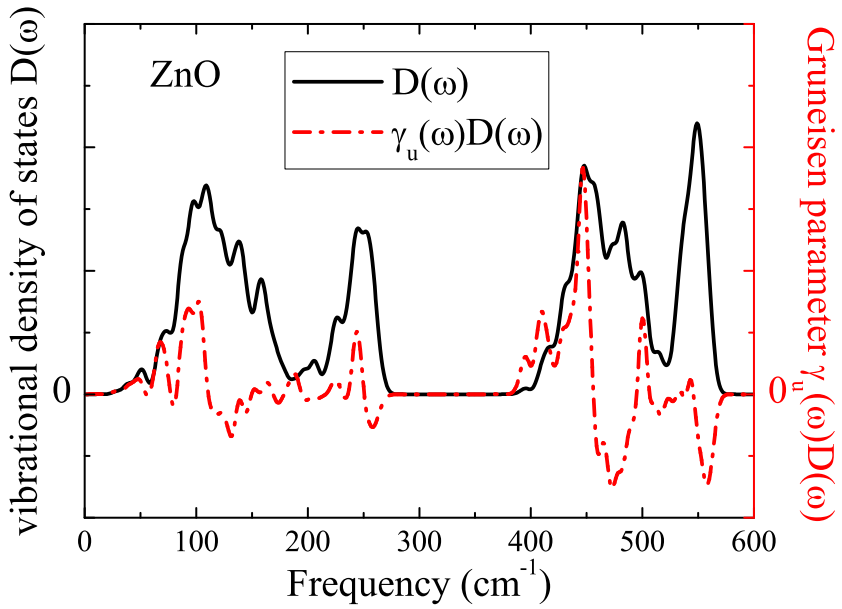

Figure 5.4: Vibrational density of states $D(\omega)$ and internal grüneisen parameter $\gamma_u(\omega)$ of ZnO.

tors $\pm\vec{q}$ whose frequencies sum up to $\omega_{\vec{0}j}$. To the lowest order terms in the perturbative expansion, only the bubble diagram has an imaginary component of the phonon self-energy, resulting in an anharmonic contribution to the linewidth[102]:

$$\Pi^{(B)}_{\vec{0}j}(\omega) = -\frac{1}{2N\hbar^2}\sum_{\vec{q},j_1,j_2}\left|V_3(\vec{0}j,\vec{q}j_1,-\vec{q}j_2)\right|^2 \left(\frac{2(\omega_{\vec{q}j_1}+\omega_{\vec{q}j_2})(n_{\vec{q}j_1}+n_{\vec{q}j_2}+1)}{(\omega_{\vec{q}j_1}+\omega_{\vec{q}j_2})^2-(\omega+i\delta)^2}+\frac{2(\omega_{\vec{q}j_1}-\omega_{\vec{q}j_2})(n_{\vec{q}j_2}-n_{\vec{q}j_1})}{(\omega_{\vec{q}j_1}-\omega_{\vec{q}j_2})^2-(\omega+i\delta)^2}\right) \tag{5.27}$$

The third-order anharmonic coefficient $V_3(\vec{0}j,\vec{q}j_1,-\vec{q}j_2)$ is readily obtained through the finite difference of the dynamical matrix by displacing atoms along the displacement pattern $u_{\kappa\alpha}(\vec{0}j)$.

Experimentally, the temperature dependence of the Raman linewidth $\Gamma(T)$ is frequently fitted as

$$\Gamma(T) = \Gamma_0 + 2C(n_1+n_2+1) \tag{5.28}$$

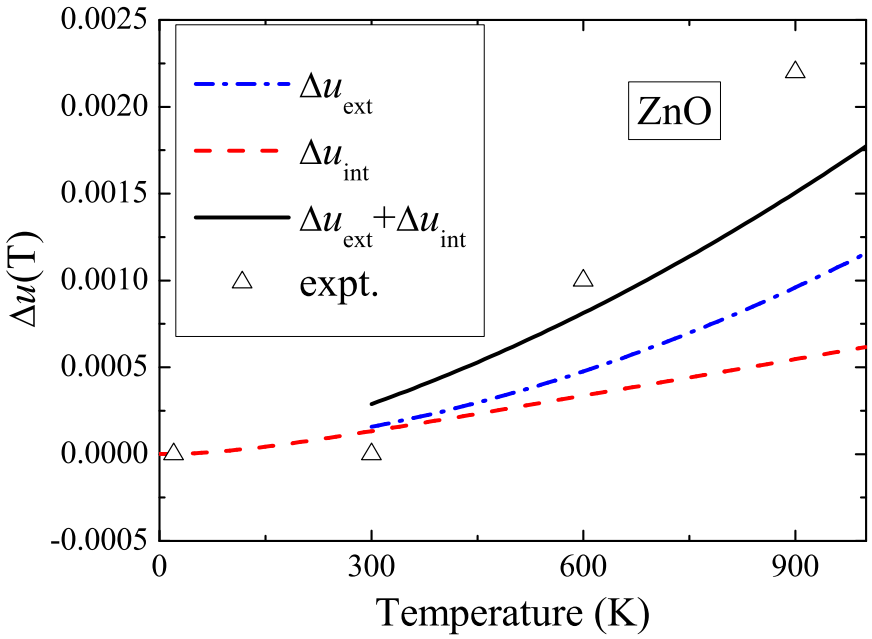

Figure 5.5: Thermal shift of the ZnO internal parameter u. The measured zero temperature value is 0.382 [97, 98], close to the "ideal" value of 3/8. Experimental values are from Ref. [88].

where Γ_0 accounts for impurity and defect scatterings, and $n_{1,2}$ describes the phonon population of the two participating phonons with opposite wave vectors $\pm\vec{q}$. To the best of my knowledge, there are no first-principles calculations on $\Gamma(T)$ for the III-V/II-VI wurtzite semiconductors. While in principle $\Gamma(T)$ can be calculated from first principles, $V_3(\vec{0}j, \vec{q}j_1, -\vec{q}j_2)$ is related to the third derivative of the total energy with respect to the atomic displacement, which involves hundreds of total energy and force calculations in the supercell approach. Therefore most researchers consider $V_3(\vec{0}j, \vec{q}j_1, -\vec{q}j_2)$ as adjustable parameters which are fitted to the experimental data. Our scheme is computationally more efficient in the way that the necessity of a supercell is reduced into the calculation of $\pm\vec{q}$ phonons along the displacement pattern $u_{\kappa\alpha}(\vec{0}j)$ within the unit cell. This scheme can be readily applied to other zone-center transverse-optic phonons.

The calculated Raman linewidth for several III-V/II-VI wurtzite semiconductors (AlN, GaN, BeO and ZnO) are shown in Figs. 5.9-5.11. In Fig.

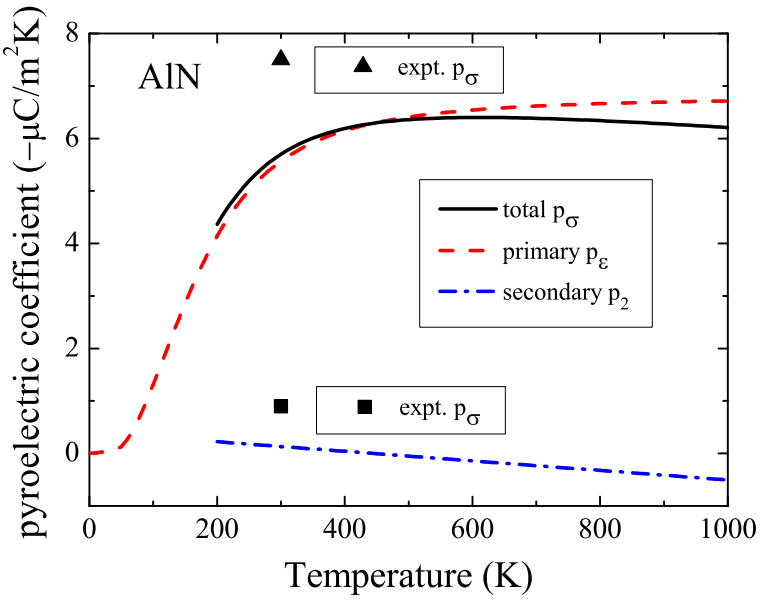

Figure 5.6: The pyroelectric coefficient of AlN.

5.9, the difference in the measured $\Gamma(0)$ for AlN is attributed to the scattering from the impurities in the samples. While experimental measurement is sensitive over the quality of the semiconductor film, our first-principles calculations treat exactly the three-phonon process. For AlN and GaN, the calculated temperature dependence of the Raman linewidth agree well with the experimental data at low-T. For GaN, at high-T the deviation becomes large, possibly due to higher-order phonon-phonon interactions which are not included in our first-principles calculations. For BeO and ZnO, to our best knowledge, no experimental measurement exists for the $A_1(TO)$ phonon. Our calculations provide predictions at the first-principles level.

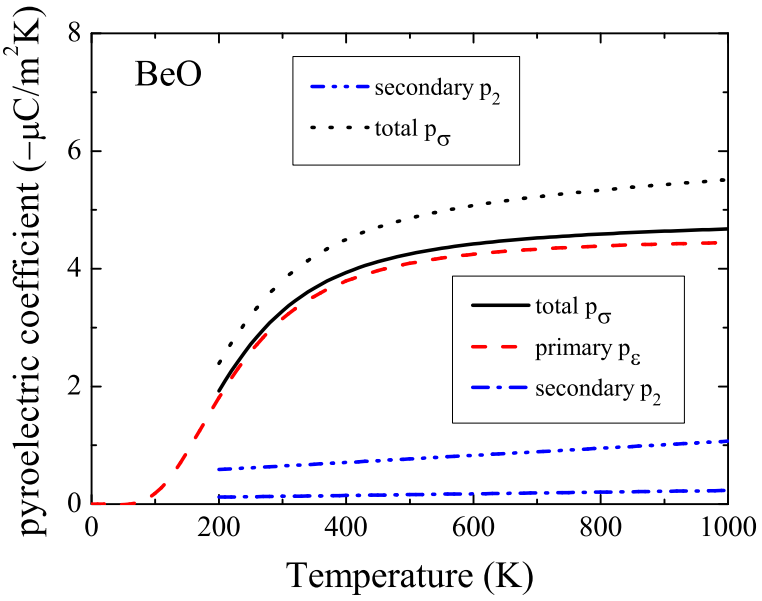

Figure 5.7: The pyroelectric coefficient of BeO. Dash dot: piezoelectric constants from Ref. [7]. Dash dot dot: piezoelectric constants from Ref. [93].

5.4 Conclusion

We have calculated the primary pyroelectric coefficients for wurtzite GaN and ZnO from first-principles. For wurtzite crystals the pyroelectricity was attributed to the anharmonic atomic displacements of the Born effective charges on the cations and anions. A good agreement was found between our first-principles calculations and the experimental data. We have shown that the primary pyroelectricity contributes to the major part of the total pyroelectricity at low temperatures, while the secondary pyroelectricity becomes comparable with the primary pyroelectricity at high temperatures. The primary pyroelectric coefficient could be separated into two parts: contributions from the acoustic and the optic phonon modes, which were moderately well described by Debye and Einstein functions respectively. The present study offers evidence that theory and computation can predict pyroelectricity with some reliability over a wide range of temperatures.

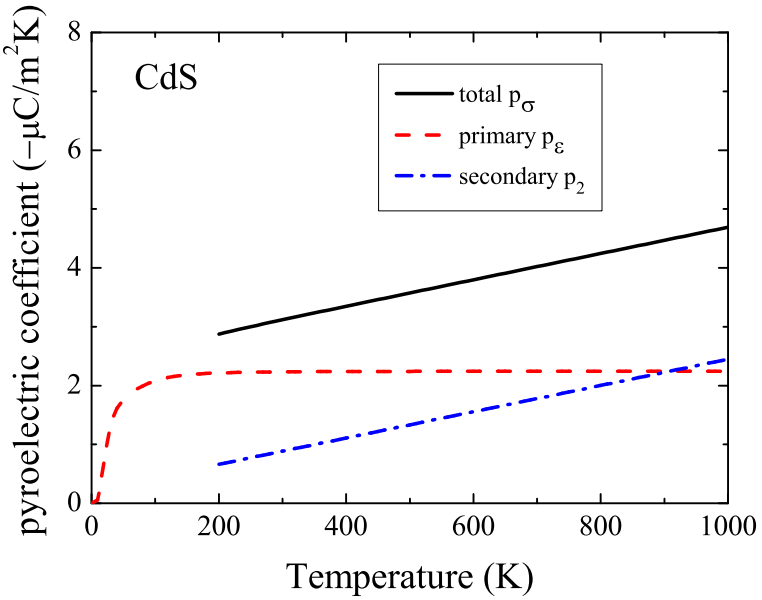

Figure 5.8: The pyroelectric coefficient of CdS. The piezoelectric constants are taken from Ref. [101].

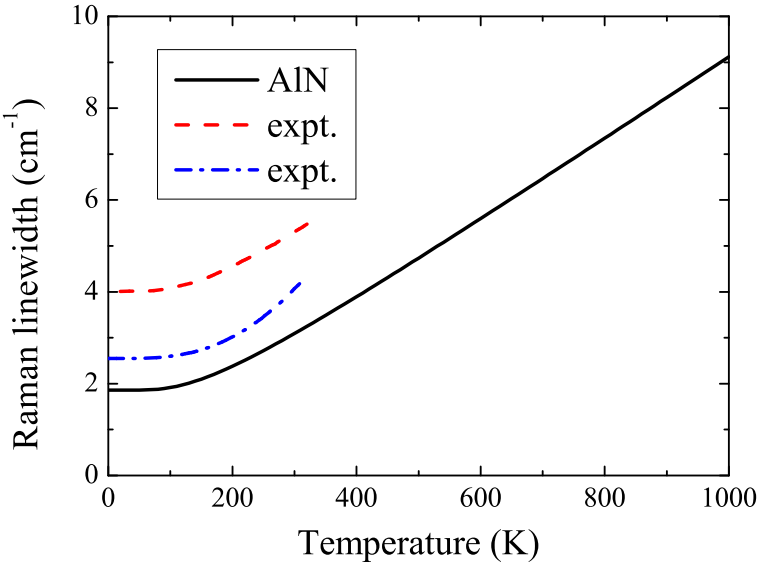

Figure 5.9: Raman linewidth of AlN. Dash: expt. from Ref. [103]. Dash dot: expt. from Ref. [104].

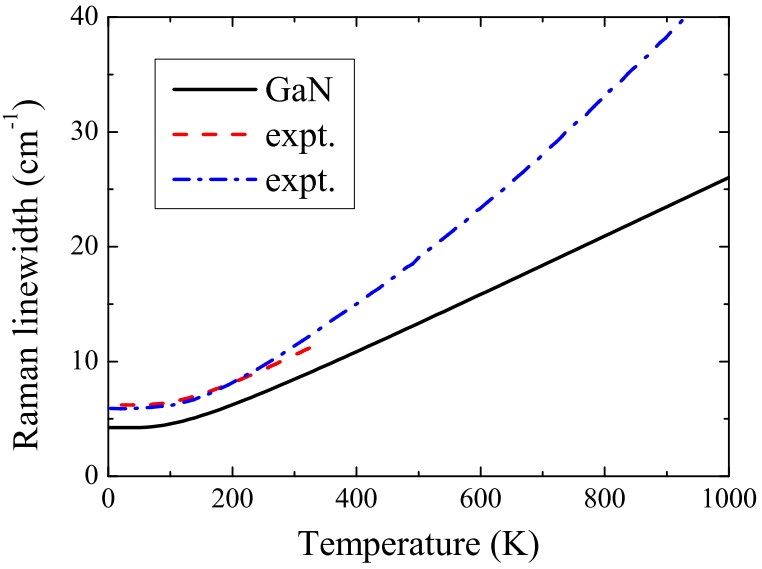

Figure 5.10: Raman linewidth of GaN. Dash: expt. from Ref. [105]. Dash dot: expt. from Ref. [106].

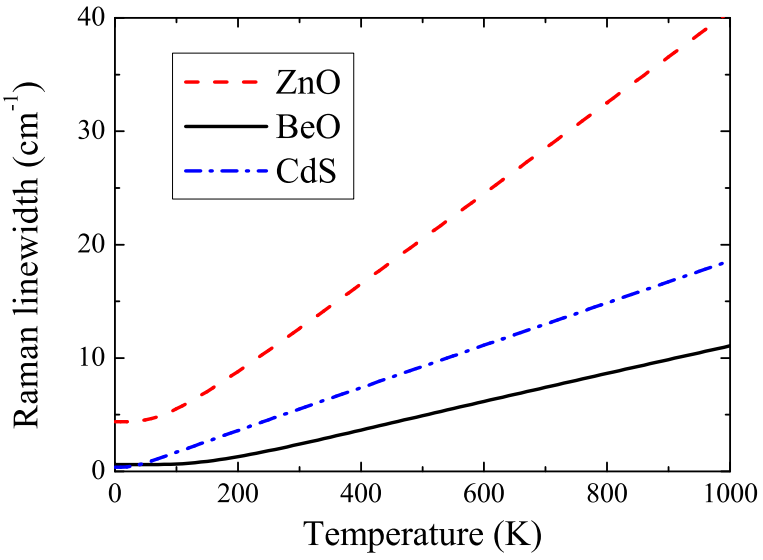

Figure 5.11: Raman linewidth of BeO, ZnO and CdS.

Chapter 6

6 $Ga_{1-x}In_xN$: Electron-phonon Interaction

6.1 Background

In the recent past, the temperature dependence of the band gaps $E_g(T)$ of semiconductors have attracted increasing attentions[107, 108, 109, 110, 111, 112, 113, 114]. Experimentally, this temperature dependence has to be determined by photoluminescence (PL) or optical absorption spectroscopy with caution. For example, it is at first reported that in InN the PL peak energy increases monotonically with increasing temperature[115]. A subsequent study yields normal redshift of optical absorption peak with increasing temperature, and attributes the anomalous blueshift of PL peak with increasing temperature to the fact that the PL peak is strongly affected by the localized states[116]. For semiconductor alloys, theoretical study on the temperature dependence of the band gap is rather at its preliminary stage. Attempt has been made to fit the experimental $E_g(x,T)$ based on the Varshni equation[117]. To our best knowledge, first-principles calculations on $E_g(T)$ for GaN, InN and $E_g(x,T)$ for their alloy $Ga_{1-x}In_xN$ are still lacking. Of particular importance for the first-principles band structure calculations is the zero-point motion renormalization (ZPR), while the composition dependence of the Varshni parameter is crucial for the extrapolation of high-temperature $E_g(T)$ from the experimental low-temperature values. The present study aims at throwing some light on the application of VCA in the first-principles calculations of the temperature dependence of the band gap.

6.2 $Ga_{1-x}In_xN$: $E_g(x,T)$

First-principles calculations are performed using the ABINIT program[118, 119]. In VCA, the potential of each atom in the alloy is replaced by a composition-weighted average of the potentials of its components. We employ the VCA provided by the ABINIT program. The pseudopotentials are

generated using the fhi98PP code[120]. The Ga-3d and In-4d electrons are explicitly included in the valence. The electronic wave-functions are expanded in a plane-wave basis with a kinetic energy cutoff of 50 Hartree. We use a $6 \times 6 \times 4$ k-point mesh for Brillouin-zone sampling. Phonons are calculated using density-functional perturbation theory (DFPT)[50] on a $8 \times 8 \times 6$ q-point mesh. It is well known that the band gap calculated from LDA is severely underestimated. In the present study we apply the recently proposed TB09 functional[121] (a modified version of the Becke-Johnson exchange[122] part combined with a LDA PW92 correlation[48] part). It allows us to improve the band gap prediction with a computational cost only slightly heavier than that of LDA. The electron-phonon matrix elements are calculated on a $8 \times 8 \times 6$ q-point grid in the adiabatic rigid-ion approximation[114]. An imaginary shift ($i\delta$) of 0.1 eV is used in the perturbation denominator of the sum-over-states to avoid numerical instability. The most common empirical relation for the variation of the band gap with temperature in semiconductors is the so-called Varshni relation[123]:

$$E_g = E_0 - \alpha T^2/(T + \beta) \tag{6.1}$$

where E_0 is the band gap at 0 K and α,β are fitting parameters. Although the Varshni relation bears no physical resemblance and incorrectly predicts a quadratic temperature dependence for $T \to 0$[124], it fits the experimental data remarkably well. In present study, we continue to use the Varshni relation for its significant popularity in applications.

The calculated lattice constants and band gaps of GaN and InN with the TB09 functional are summarized in Table 6.1. While LDA severely underestimates the band gap for GaN and even incorrectly predicts a metallic state for InN, the TB09 functional yields band gaps close to the experiments. Our VCA calculations show that the dependence of a and c on the In content x clearly deviate from the Vegard's law[60]. In Fig. 6.1 we show the calculated and experimental band gaps. To study the effect of local environment relaxations (which VCA lacks) on the band gaps, we also perform calculations using the TB09 functional on fully relaxed SQSs. Firstly, the TB09 functional corrects for the LDA band gaps independently on x, which further confirms the applicability of LDA in calculating the band gap bowing parameter for $Ga_{1-x}In_xN$ alloy[36, 37]. Secondly, our VCA calculations show that the band gap bowing at low In content is larger than that at high In content. Therefore one single composition-independent bowing parameter may

Table 6.1: Lattice constants and band gaps of GaN and InN calculated with the TB09 functional. Experimental data are taken from Ref. [67] and are shown in parentheses.

	a(Å)	c(Å)	E_g(eV)
GaN	3.216 (3.189)	5.239 (5.185)	2.93 (3.51)
InN	3.521 (3.545)	5.692 (5.703)	0.57 (0.78)

not be adequate for accurate description of the nonlinear band gap bowing. If we enforce the composition-independent bowing, the corresponding bowing parameter reads 3.85 eV by a least-square fitting. Thirdly, the band gap bowing of SQS alloy is much smaller than that of VCA alloy. The tendency accidentally corresponds to the effect of In clustering where the band gap bowing ranges from 2.1 eV for the uniform case to 3.9 eV for the clustering case[39]. The calculated phonon density of states (DOS) is shown in Fig. 6.2. The peak of phonon DOS shifts to lower frequency while the shape of phonon DOS remains unchanged as In content x is increased. Compared with 32-atom SQS calculations[43], VCA succeeds in capturing the shift of phonon DOS, but fails in describing the broadening of the phonon spectra, since the broadening of phonon DOS upon alloying is associated with local environment disorder.

The temperature dependence of the band gap ΔE_g(T) can be decomposed into two parts: the electron-phonon interaction (EPI) term and the thermal expansion (TE) term. While the EPI contribution to the temperature dependence of the band gap of GaN is calculated from first-principles, the TE contribution[124] is calculated from $-B(\frac{\partial E_g}{\partial p})_T \int_0^T [2\alpha_a(T') + \alpha_c(T')]dT'$. The bulk modulus B is taken from *ab initio* calculatoins[125], while the pressure coefficient of band gap $(\frac{\partial E_g}{\partial p})_T$ is taken from low-temperature PL measurement[126]. The linear thermal expansion coefficient $\alpha(T)$ over the entire temperature range is described by the experimentally determined Debye model[127]. Our calculations agree well with the experimental data[128], as is shown in Fig. 6.3. The ZPR is as large as -0.15 eV. The main contribution to the temperature dependence of the band gap comes from the EPI term, which is almost three times of the TE term. The fitted Varshni parameters (for only the EPI term) α and β reads 0.51 meV/K and 745

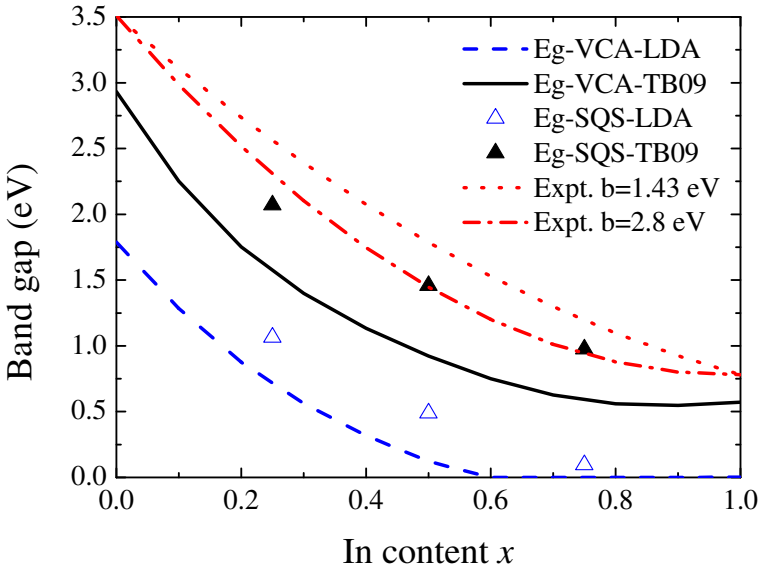

Figure 6.1: Band gaps of $Ga_{1-x}In_xN$. Zero band gaps represent the incorrect metallic states predicted by LDA. SQSs are taken from Ref. [43]. Experimental bowing parameters are taken from Ref. [34] ($b = 1.43$ eV) and Ref. [35] ($b = 2.8$ eV).

K respectively. A simple average of the diverse experimental data suggests α=0.91 meV/K and β=830 K[129], while a more recent measurement yields α in the range of 0.54-0.63 meV/K and β in the range of 700-745K.

The calculated (x, T) dependence of the band gap is shown in Fig. 6.4. Due to the LDA band gap problem (see Fig. 6.1), we focus on the Ga-rich ($x \leq$0.5) contents. The ZPR and the Varshni parameter α decrease in magnitude as x is increased because of the larger atomic mass of In, indicating a decrease in the strength of EPI. We describe the deviation of the composition dependence from linearity by a bowing term $-bx(1-x)$, as is shown in Fig. 6.5. The bowing parameter for the ZPR is -0.1 eV, which should be taken into account in the calculated band gap bowing parameter (in present study 3.85 eV). The extrapolated ZPR for InN is -0.036 eV, considerably smaller than that for GaN. The extrapolated α for InN is 0.096 meV/K, while the experimentally measured value reads 0.414 meV/K[116]. The large difference indicates a significant role of TE in the $E_g(T)$ of InN, contrary to the

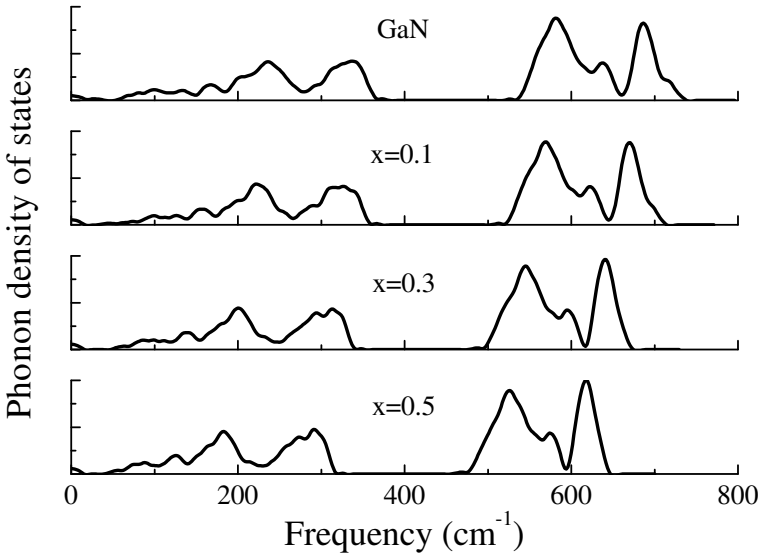

Figure 6.2: Phonon density of states of $Ga_{1-x}In_xN$.

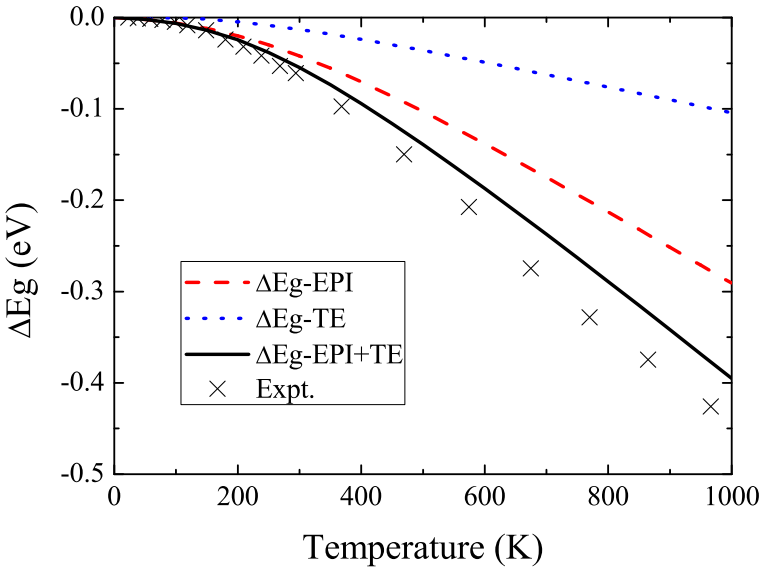

Figure 6.3: Temperature dependence of the band gap (referenced to zero) of GaN. Experimental data are taken from Ref. [128].

situation for GaN where EPI dominates over TE.

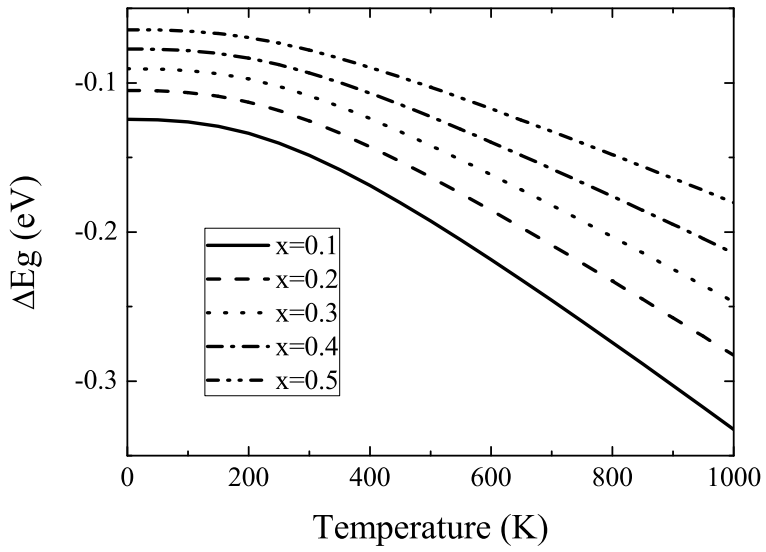

Figure 6.4: Temperature dependence of the band gaps of $Ga_{1-x}In_xN$ alloy at $x \leq 0.5$.

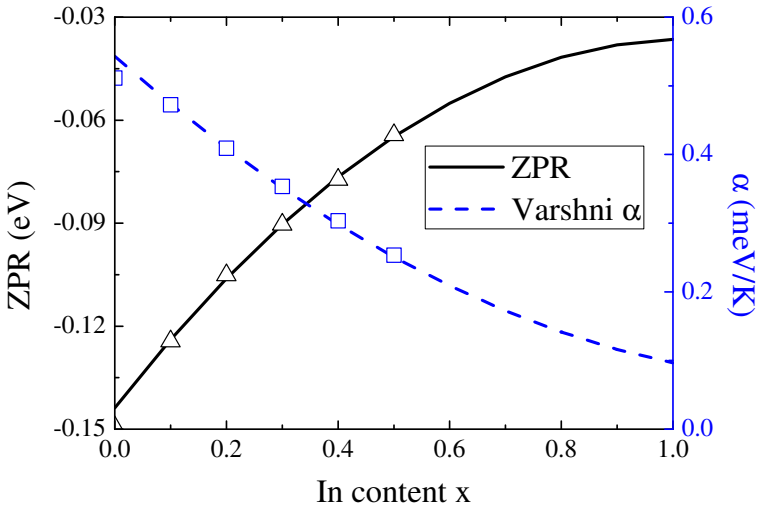

Figure 6.5: Composition dependence of the ZPR and the Varshni α.

6.3 Conclusion

In conclusion, we have studied the structural, electronic and vibrational properties of the $Ga_{1-x}In_xN$ alloy using VCA from first-principles. We obtain a

band gap bowing parameter of 3.85 eV with the TB09 functional. VCA succeeds in capturing the shift of phonon DOS, but fails in describing the broadening of the phonon spectra. We have also studied the role of EPI in the temperature dependence of the band gaps for GaN, InN and their alloy $Ga_{1-x}In_xN$. For GaN EPI plays the dominant role, while for InN TE could contribute significantly. The calculated ZPR is important for modifying theoretical zero-temperature band gap, while the fitted Varshni parameter α is crucial for extrapolating high-temperature band gap experimentally.

References

[1] K. Maeda, T. Takata, M. Hara, N. Saito, Y. Inoue, H. Kobayashi, and K. Domen. GaN:ZnO solid solution as a photocatalyst for visible-light-driven overall water splitting. *J. Am. Chem. Soc.*, 127(23):8286, 2005.

[2] L. Li, J. T. Muckerman, M. S. Hybertsen, and P. B. Allen. Phase diagram, structure, and electronic properties of $(Ga_{1-x}Zn_x)(N_{1-x}O_x)$ solid solutions from DFT-based simulations. *Phys. Rev. B*, 83:134202, 2011.

[3] J.M. Sanchez, F. Ducastelle, and D. Gratias. Generalized cluster description of multicomponent systems. *Physica A*, 128(12):334, 1984.

[4] J. W. D. Connolly and A. R. Williams. Density-functional theory applied to phase transformations in transition-metal alloys. *Phys. Rev. B*, 27:5169, 1983.

[5] D. De Fontaine. Cluster approach to order-disorder transformations in alloys. In Henry Ehrenreich and David Turnbull, editors, *Solid State Physics*, volume 47, page 33. Academic Press, 1994.

[6] I. D. Brown. Recent developments in the methods and applications of the bond valence model. *Chem. Rev.*, 109(12):6858, 2009.

[7] F. Bernardini, V. Fiorentini, and D. Vanderbilt. Spontaneous polarization and piezoelectric constants of III-V nitrides. *Phys. Rev. B*, 56:R10024, 1997.

[8] M. Born. On the quantum theory of pyroelectricity. *Rev. Mod. Phys.*, 17:245, 1945.

[9] B. P. Burton, S. Demers, and A. van de Walle. First principles phase diagram calculations for the wurtzite-structure quasibinary systems SiC-AlN, SiC-GaN and SiC-InN. *J. Appl. Phys.*, 110(2):023507, 2011.

[10] J. Ma, H.-X. Deng, J.-W. Luo, and S.-H. Wei. Origin of the failed ensemble average rule for the band gaps of disordered nonisovalent semiconductor alloys. *Phys. Rev. B*, 90:115201, 2014.

[11] K. Lee, B. M. Tienes, M. B. Wilker, K. J. Schnitzenbaumer, and G. Dukovic. $(Ga_{1-x}Zn_x)(N_{1-x}O_x)$ nanocrystals: Visible absorbers with tunable composition and absorption spectra. *Nano Lett.*, 12(6):3268, 2012.

[12] H. Chen, L. Wang, J. Bai, J. C. Hanson, J. B. Warren, J. T. Muckerman, E. Fujita, and J. A. Rodriguez. In Situ XRD studies of ZnO/GaN mixtures at high pressure and high temperature: Synthesis of Zn-rich $(Ga_{1-x}Zn_x)(N_{1-x}O_x)$ photocatalysts. *J. Phys. Chem. C*, 114(4):1809, 2010.

[13] L. L. Jensen, J. T. Muckerman, and M. D. Newton. First-principles studies of the structural and electronic properties of the $(Ga_{1-x}Zn_x)(N_{1-x}O_x)$ solid solution photocatalyst. *J. Phys. Chem. C*, 112(9):3439, 2008.

[14] C. Di Valentin. Electronic structure of $(Ga_{1-x}Zn_x)(N_{1-x}O_x)$ photocatalyst for water splitting by hybrid hartree-fock density functional theory methods. *J. Phys. Chem. C*, 114(15):7054, 2010.

[15] M. N. Huda, Y. Yan, S. H. Wei, and M. M. Al-Jassim. Electronic structure of ZnO:GaN compounds: Asymmetric bandgap engineering. *Phys. Rev. B*, 78:195204, 2008.

[16] M. Łopuszyński and J. A. Majewski. Ordering in ternary nitride semiconducting alloys. *Phys. Rev. B*, 85:035211, 2012.

[17] I. D. Brown. Recent developments in the methods and applications of the bond valence model. *Chem. Rev.*, 109(12):6858, 2009.

[18] S. Liu, I. Grinberg, H. Takenaka, and A. M. Rappe. Reinterpretation of the bond-valence model with bond-order formalism: An improved bond-valence-based interatomic potential for $PbTiO_3$. *Phys. Rev. B*, 88:104102, 2013.

[19] S. Liu, I. Grinberg, and A. M. Rappe. Development of a bond-valence based interatomic potential for $BiFeO_3$ for accurate molecular dynamics simulations. *J. Phys.: Condens. Matter*, 25(10):102202, 2013.

[20] T. Hiemstra, P. Venema, and W. H. Van Riemsdijk. Intrinsic proton affinity of reactive surface groups of metal (hydr)oxides: The bond valence principle. *J. Colloid Interface Sci.*, 184(2):680, 1996.

[21] B. R. Bickmore, C. J. Tadanier, K. M. Rosso, W. D. Monn, and D. L. Eggett. Bond-valence methods for pKa prediction: critical reanalysis and a new approach. *Geochim. Cosmochim. Acta*, 68(9):2025, 2004.

[22] S. Wang and L.-W. Wang. Atomic and electronic structures of GaN/ZnO alloys. *Phys. Rev. Lett.*, 104:065501, 2010.

[23] S. Wang and L.-W. Wang. Charge flow model for atomic ordering in nonisovalent alloys. *Phys. Rev. B*, 83:115208, 2011.

[24] A. van de Walle and G. Ceder. First-principles computation of the vibrational entropy of ordered and disordered Pd_3V. *Phys. Rev. B*, 61:5972, 2000.

[25] J. K. Burdett and F. C. Hawthorne. An orbital approach to the theory of bond valence. *Am. Mineral.*, 78(9-10):884, 1993.

[26] I. Mayer. Towards a "Chemical" Hamiltonian. *Int. J. Quant. Chem.*, 23(2):341, 1983.

[27] R. Resta. Electrical polarization and orbital magnetization: the modern theories. *Journal of Physics: Condensed Matter*, 22(12):123201, 2010.

[28] S. B. Lang. Pyroelectricity: from ancient curiosity to modern imaging tool. *Phys. Today*, 58(8):31, 2005.

[29] K. Matocha, V. Tilak, and G. Dunne. Comparison of metal-oxide-semiconductor capacitors on *c*- and *m*-plane gallium nitride. *Appl. Phys. Lett.*, 90(12):123511, 2007.

[30] A. D. Bykhovski, V. V. Kaminski, M. S. Shur, Q. C. Chen, and M. A. Khan. Pyroelectricity in gallium nitride thin films. *Applied Physics Letters*, 69(21):3254, 1996.

[31] Q. Peng and R. E. Cohen. Origin of pyroelectricity in $LiNbO_3$. *Phys. Rev. B*, 83:220103, 2011.

[32] J. D. Zook and S. T. Liu. Pyroelectric effects in thin film. *J. Appl. Phys.*, 49(8):4604, 1978.

[33] J. Li, J. Y. Lin, and H. X. Jiang. Direct hydrogen gas generation by using InGaN epilayers as working electrodes. *Applied Physics Letters*, 93(16):162107, 2008.

[34] J. Wu, W. Walukiewicz, K. M. Yu, J. W. Ager, E. E. Haller, H. Lu, and W. J. Schaff. Small band gap bowing in $In_{1-x}Ga_xN$ alloys. *Applied Physics Letters*, 80(25):4741, 2002.

[35] M. Moret, B. Gil, S. Ruffenach, O. Briot, Ch. Giesen, M. Heuken, S. Rushworth, T. Leese, and M. Succi. Optical, structural investigations and band-gap bowing parameter of GaInN alloys. *Journal of Crystal Growth*, 311(10):2795, 2009.

[36] P. G. Moses, M. Miao, Q. Yan, and C. G. Van de Walle. Hybrid functional investigations of band gaps and band alignments for AlN, GaN, InN, and InGaN. *The Journal of Chemical Physics*, 134(8):084703, 2011.

[37] R. R. Pel, C. Caetano, M. Marques, L. G. Ferreira, J. Furthmller, and L. K. Teles. Accurate band gaps of AlGaN, InGaN, and AlInN alloys calculations based on LDA-1/2 approach. *Applied Physics Letters*, 98(15):151907, 2011.

[38] M. Csar, Y. Ke, W. Ji, H. Guo, and Z. Mi. Band gap of $In_xGa_{1-x}N$: A first principles analysis. *Applied Physics Letters*, 98(20):202107, 2011.

[39] I. Gorczyca, S. P. Łepkowski, T. Suski, N. E. Christensen, and A. Svane. Influence of indium clustering on the band structure of semiconducting ternary and quaternary nitride alloys. *Phys. Rev. B*, 80:075202, 2009.

[40] L. C. de Carvalho, A. Schleife, J. Furthmüller, and F. Bechstedt. Distribution of cations in wurtzite $In_xGa_{1-x}N$ and $In_xAl_{1-x}N$ alloys: Consequences for energetics and quasiparticle electronic structures. *Phys. Rev. B*, 85:115121, 2012.

[41] L. Bellaiche and D. Vanderbilt. Virtual crystal approximation revisited: Application to dielectric and piezoelectric properties of perovskites. *Phys. Rev. B*, 61:7877, 2000.

[42] N. J. Ramer and A. M. Rappe. Virtual-crystal approximation that works: Locating a compositional phase boundary in $Pb(Zr_{1-x}Ti_x)O_3$. *Phys. Rev. B*, 62:R743, 2000.

[43] C. K. Gan, Y. P. Feng, and D. J. Srolovitz. First-principles calculation of the thermodynamics of $In_xGa_{1-x}N$ alloys: Effect of lattice vibrations. *Phys. Rev. B*, 73:235214, 2006.

[44] P. Hohenberg and W. Kohn. Inhomogeneous electron gas. *Phys. Rev.*, 136:B864, 1964.

[45] W. Kohn and L. J. Sham. Self-consistent equations including exchange and correlation effects. *Phys. Rev.*, 140:A1133, 1965.

[46] R. M. Martin. *Electronic Structure*. Cambridge University Press, 2004.

[47] J. P. Perdew and A. Zunger. Self-interaction correction to density-functional approximations for many-electron systems. *Phys. Rev. B*, 23:5048, 1981.

[48] J. P. Perdew and Y. Wang. Accurate and simple analytic representation of the electron-gas correlation energy. *Phys. Rev. B*, 45:13244, 1992.

[49] J. P. Perdew, K. Burke, and M. Ernzerhof. Generalized gradient approximation made simple. *Phys. Rev. Lett.*, 77:3865, 1996.

[50] S. Baroni, S. de Gironcoli, A. Dal Corso, and P. Giannozzi. Phonons and related crystal properties from density-functional perturbation theory. *Rev. Mod. Phys.*, 73:515, 2001.

[51] J. Liu, L. S. Pedroza, C. Misch, M. V. Fernndez-Serra, and P. B. Allen. Temperature and composition dependence of short-range order and entropy, and statistics of bond length: the semiconductor alloy $(Ga_{1-x}Zn_x)(N_{1-x}O_x)$. *J. Phys.: Condens. Matter*, 26(27):274204, 2014.

[52] S.-H. Wei, L. G. Ferreira, J. E. Bernard, and A. Zunger. Electronic properties of random alloys: Special quasirandom structures. *Phys. Rev. B*, 42:9622, 1990.

[53] A. van de Walle and M. Asta. Self-driven lattice-model Monte Carlo simulations of alloy thermodynamic properties and phase diagrams. *Modell. Simul. Mater. Sci. Eng.*, 10(5):521, 2002.

[54] A. van de Walle, M. Asta, and G. Ceder. The alloy theoretic automated toolkit: A user guide. *Calphad*, 26(4):539, 2002.

[55] A. van de Walle and G. Ceder. Automating first-principles phase diagram calculations. *J. Phase Equilib.*, 23(4):348, 2002.

[56] P. Giannozzi, S. Baroni, N. Bonini, M. Calandra, R. Car, C. Cavazzoni, D. Ceresoli, G. L. Chiarotti, M. Cococcioni, I. Dabo, A. Dal Corso, S. de Gironcoli, S. Fabris, G. Fratesi, R. Gebauer, U. Gerstmann, C. Gougoussis, A. Kokalj, M. Lazzeri, L. Martin-Samos, N. Marzari, F. Mauri, R. Mazzarello, S. Paolini, A. Pasquarello, L. Paulatto, C. Sbraccia, S. Scandolo, G. Sclauzero, A. P. Seitsonen, A. Smogunov, P. Umari, and R. M. Wentzcovitch. QUANTUM ESPRESSO: a modular and open-source software project for quantum simulations of materials. *J. Phys.: Condens. Matter*, 21(39):395502, 2009.

[57] J. P. Perdew, A. Ruzsinszky, G. I. Csonka, O. A. Vydrov, G. E. Scuseria, L. A. Constantin, X. Zhou, and K. Burke. Restoring the density-gradient expansion for exchange in solids and surfaces. *Phys. Rev. Lett.*, 100:136406, 2008.

[58] P. E. Blöchl. Projector augmented-wave method. *Phys. Rev. B*, 50:17953, 1994.

[59] A. Dal Corso. Pseudopotentials periodic table: From H to Pu. *Computational Materials Science*, 95:337, 2014.

[60] A. R. Denton and N. W. Ashcroft. Vegard's law. *Phys. Rev. A*, 43:3161, 1991.

[61] D. Alf. PHON: A program to calculate phonons using the small displacement method. *Comput. Phys. Commun.*, 180(12):2622, 2009.

[62] J. M. Soler, E. Artacho, J. D. Gale, A. García, J. Junquera, P. Ordejón, and D. Sánchez-Portal. The SIESTA method for ab initio order-N materials simulation. *J. Phys.: Condens. Matter*, 14(11):2745, 2002.

[63] R. Agrawal and H. D. Espinosa. Giant piezoelectric size effects in zinc oxide and gallium nitride nanowires. a first principles investigation. *Nano Lett.*, 11(2):786, 2011.

[64] S. L. Dudarev, G. A. Botton, S. Y. Savrasov, C. J. Humphreys, and A. P. Sutton. Electron-energy-loss spectra and the structural stability of nickel oxide: An LSDA+U study. *Phys. Rev. B*, 57:1505, 1998.

[65] A. Janotti, D. Segev, and C. G. Van de Walle. Effects of cation d states on the structural and electronic properties of III-nitride and II-oxide wide-band-gap semiconductors. *Phys. Rev. B*, 74:045202, 2006.

[66] M. A. L. Marques, J. Vidal, M. J. T. Oliveira, L. Reining, and S. Botti. Density-based mixing parameter for hybrid functionals. *Phys. Rev. B*, 83:035119, 2011.

[67] T. Hanada. Basic properties of ZnO, GaN, and related materials. In Takafumi Yao and Soon-Ku Hong, editors, *Oxide and Nitride Semiconductors*, volume 12 of *Advances in Materials Research*, pages 1–19. Springer Berlin Heidelberg, 2009.

[68] I. D. Brown. *The chemical bond in inorganic chemistry*. Oxford University Press, 2006.

[69] R. S. Mulliken. Electronic population analysis on LCAO-MO molecular wave functions. I. *J. Chem. Phys.*, 23(10):1833, 1955.

[70] R. S. Mulliken. Electronic population analysis on LCAO-MO molecular wave functions. II. Overlap populations, bond orders, and covalent bond energies. *J. Chem. Phys.*, 23(10):1841, 1955.

[71] N. E. Brese and M. O'Keeffe. Bond-valence parameters for solids. *Acta Crystallogr. Sect. B*, 47(2):192, 1991.

[72] M. A. Harvey, S. Baggio, and R. Baggio. A new simplifying approach to molecular geometry description: the vectorial bond-valence model. *Acta Crystallogr. Sect. B*, 62(6):1038, 2006.

[73] I. D. Brown. Predicting bond lengths in inorganic crystals. *Acta Crystallogr. Sect. B*, 33(5):1305, 1977.

[74] http://www.icmab.es/siesta/.

[75] M. Wolfsberg and L. Helmholz. The spectra and electronic structure of the tetrahedral ions MnO_4^-, CrO_4^{--}, and ClO_4^-. *J. Chem. Phys.*, 20(5):837, 1952.

[76] Jian Liu, Maria V Fernndez-Serra, and Philip B Allen. Submitted.

[77] Y. Wang, C. L. Zacherl, S. Shang, L.-Q. Chen, and Z.-K. Liu. Phonon dispersions in random alloys: a method based on special quasi-random structure force constants. *J. Phys.: Condens. Matter*, 23(48):485403, 2011.

[78] B. P. Burton, A. van de Walle, and U. Kattner. First principles phase diagram calculations for the wurtzite-structure systems AlN-GaN, GaN-InN, and AlN-InN. *J. Appl. Phys.*, 100(11):113528, 2006.

[79] P. N. Keating. Effect of invariance requirements on the elastic strain energy of crystals with application to the diamond structure. *Phys. Rev.*, 145:637, 1966.

[80] A. Silverman, A. Zunger, R. Kalish, and J. Adler. Atomic-scale structure of disordered $Ga_{1-x}In_xP$ alloys. *Phys. Rev. B*, 51:10795, 1995.

[81] F. Grosse and J. Neugebauer. Limits and accuracy of valence force field models for $In_xGa_{1-x}P$ alloys. *Phys. Rev. B*, 63:085207, 2001.

[82] K. Biswas, A. Franceschetti, and S. Lany. Generalized valence-force-field model of (Ga,In)(N,P) ternary alloys. *Phys. Rev. B*, 78:085212, 2008.

[83] T. Saito and Y. Arakawa. Atomic structure and phase stability of $In_xGa_{1-x}P$ random alloys calculated using a valence-force-field method. *Phys. Rev. B*, 60:1701, 1999.

[84] M. Łopuszyński and J. A. Majewski. Computational study of structural and elastic properties of random $Al_xGa_yIn_{1-x-y}N$ alloys. *J. Phys.: Condens. Matter*, 22(20):205801, 2010.

[85] A. Belabbes, J. Furthmüller, and F. Bechstedt. Relation between spontaneous polarization and crystal field from first principles. *Phys. Rev. B*, 87:035305, 2013.

[86] B. Szigeti. Temperature dependence of pyroelectricity. *Phys. Rev. Lett.*, 35:1532, 1975.

[87] G. Heiland and H. Ibach. Pyroelectricity of zinc oxide. *Solid State Commun.*, 4(7):353, 1966.

[88] J. Albertsson, S. C. Abrahams, and Å. Kvick. Atomic displacement, anharmonic thermal vibration, expansivity and pyroelectric coefficient thermal dependences in ZnO. *Acta Crystallogr. Sect. B-Struct. Sci.*, 45(1):34, 1989.

[89] T. G. Gibbons. Calculation of the thermal expansion for a quasiharmonic model of tellurium. *Phys. Rev. B*, 7:1410, 1973.

[90] N. Troullier and J. Martins. Efficient pseudopotentials for plane-wave calculations. *Phys. Rev. B*, 43:1993, 1991.

[91] H. Iwanaga, A. Kunishige, and S. Takeuchi. Anisotropic thermal expansion in wurtzite-type crystals. *J. Mater. Sci.*, 35(10):2451, 2000.

[92] A. Zoroddu, F. Bernardini, P. Ruggerone, and V. Fiorentini. First-principles prediction of structure, energetics, formation enthalpy, elastic constants, polarization, and piezoelectric constants of AlN, GaN, and InN: Comparison of local and gradient-corrected density-functional theory. *Phys. Rev. B*, 64:045208, 2001.

[93] Y. Noel, M. Llunell, R. Orlando, P. D'Arco, and R. Dovesi. Performance of various hamiltonians in the study of the piezoelectric properties of crystalline compounds: The case of BeO and ZnO. *Phys. Rev. B*, 66:214107, 2002.

[94] V. Yu. Davydov, Yu. E. Kitaev, I. N. Goncharuk, A. N. Smirnov, J. Graul, O. Semchinova, D. Uffmann, M. B. Smirnov, A. P. Mirgorodsky, and R. A. Evarestov. Phonon dispersion and Raman scattering in hexagonal GaN and AlN. *Phys. Rev. B*, 58:12899, 1998.

[95] J. Serrano, F. J. Manjón, A. H. Romero, A. Ivanov, M. Cardona, R. Lauck, A. Bosak, and M. Krisch. Phonon dispersion relations of zinc oxide: Inelastic neutron scattering and *ab initio* calculations. *Phys. Rev. B*, 81:174304, 2010.

[96] W. S. Yan, R. Zhang, Z. L. Xie, X. Q. Xiu, Y. D. Zheng, Z. G. Liu, S. Xu, and Z. H. He. The contributions of the acoustic modes and optical modes to the primary pyroelectric coefficient of GaN. *Appl. Phys. Lett.*, 94(24):242111, 2009.

[97] H. Karzel, W. Potzel, M. Köfferlein, W. Schiessl, M. Steiner, U. Hiller, G. M. Kalvius, D. W. Mitchell, T. P. Das, P. Blaha, K. Schwarz, and M. P. Pasternak. Lattice dynamics and hyperfine interactions in ZnO and ZnSe at high external pressures. *Phys. Rev. B*, 53:11425, 1996.

[98] E. H. Kisi and M. M. Elcombe. u parameters for the wurtzite structure of ZnS and ZnO using powder neutron diffraction. *Acta Crystallographica Section C*, 45(12):1867, 1989.

[99] M.-A. Dubois and P. Muralt. Properties of aluminum nitride thin films for piezoelectric transducers and microwave filter applications. *Applied Physics Letters*, 74(20):3032, 1999.

[100] O. Ambacher, J. Majewski, C. Miskys, A. Link, M. Hermann, M. Eickhoff, M. Stutzmann, F. Bernardini, V. Fiorentini, V. Tilak, B. Schaff, and L. F. Eastman. Pyroelectric properties of Al(In)GaN/GaN hetero- and quantum well structures. *Journal of Physics: Condensed Matter*, 14(13):3399, 2002.

[101] Don Berlincourt, Hans Jaffe, and L. R. Shiozawa. Electroelastic properties of the sulfides, selenides, and tellurides of zinc and cadmium. *Phys. Rev.*, 129:1009, 1963.

[102] M. Lazzeri, M. Calandra, and F. Mauri. Anharmonic phonon frequency shift in MgB_2. *Phys. Rev. B*, 68:220509, 2003.

[103] P. Pandit, D. Y. Song, and M. Holtz. Decay of zone-center phonons in AlN with A1, E1, and E2 symmetries. *Journal of Applied Physics*, 102(11):113510, 2007.

[104] M. Kazan, Ch. Zgheib, E. Moussaed, and P. Masri. Temperature dependence of Raman-active modes in AlN. *Diamond and Related Materials*, 15(48):1169, 2006.

[105] D. Y. Song, S. A. Nikishin, M. Holtz, V. Soukhoveev, A. Usikov, and V. Dmitriev. Decay of zone-center phonons in GaN with A1, E1, and E2 symmetries. *Journal of Applied Physics*, 101(5):053535, 2007.

[106] W. S. Li, Z. X. Shen, Z. C. Feng, and S. J. Chua. Temperature dependence of Raman scattering in hexagonal gallium nitride films. *Journal of Applied Physics*, 87(7):3332, 2000.

[107] D. Olguin, M. Cardona, and A. Cantarero. Electronphonon effects on the direct band gap in semiconductors: {LCAO} calculations. *Solid State Communications*, 122(11):575, 2002.

[108] F. Giustino, M. L. Cohen, and S. G. Louie. Electron-phonon interaction using Wannier functions. *Phys. Rev. B*, 76:165108, 2007.

[109] A. Marini. *Ab Initio* finite-temperature excitons. *Phys. Rev. Lett.*, 101:106405, 2008.

[110] F. Giustino, S. G. Louie, and M. L. Cohen. Electron-phonon renormalization of the direct band gap of diamond. *Phys. Rev. Lett.*, 105:265501, 2010.

[111] J. Noffsinger, E. Kioupakis, C. G. Van de Walle, S. G. Louie, and M. L. Cohen. Phonon-assisted optical absorption in silicon from first principles. *Phys. Rev. Lett.*, 108:167402, 2012.

[112] C. E. Patrick and F. Giustino. Unified theory of electron-phonon renormalization and phonon-assisted optical absorption. *Journal of Physics: Condensed Matter*, 26(36):365503, 2014.

[113] S. Poncé, G. Antonius, Y. Gillet, P. Boulanger, J. L. Janssen, A. Marini, M. Côté, and X. Gonze. Temperature dependence of electronic eigenenergies in the adiabatic harmonic approximation. *Phys. Rev. B*, 90:214304, 2014.

[114] S. Ponc, Y. Gillet, J. L. Janssen, A. Marini, M. Verstraete, and X. Gonze. Temperature dependence of the electronic structure of semiconductors and insulators. *The Journal of Chemical Physics*, 143(10):102813, 2015.

[115] J. Wu, W. Walukiewicz, K. M. Yu, J. W. Ager, E. E. Haller, H. Lu, W. J. Schaff, Y. Saito, and Y. Nanishi. Unusual properties of the fundamental band gap of InN. *Applied Physics Letters*, 80(21):3967, 2002.

[116] J. Wu, W. Walukiewicz, W. Shan, K. M. Yu, J. W. Ager, S. X. Li, E. E. Haller, H. Lu, and W. J. Schaff. Temperature dependence of the fundamental band gap of InN. *Journal of Applied Physics*, 94(7):4457, 2003.

[117] U. Tisch, B. Meyler, O. Katz, E. Finkman, and J. Salzman. Dependence of the refractive index of $Al_xGa_{1-x}N$ on temperature and composition at elevated temperatures. *Journal of Applied Physics*, 89(5):2676, 2001.

[118] X. Gonze, J.-M. Beuken, R. Caracas, F. Detraux, M. Fuchs, G.-M. Rignanese, L. Sindic, M. Verstraete, G. Zerah, F. Jollet, M. Torrent, A. Roy, M. Mikami, Ph. Ghosez, J.-Y. Raty, and D. C. Allan. First-principles computation of material properties: the ABINIT software project. *Computational Materials Science*, 25(3):478, 2002.

[119] X. Gonze, B. Amadon, P.-M. Anglade, J.-M. Beuken, F. Bottin, P. Boulanger, F. Bruneval, D. Caliste, R. Caracas, M. Cote, T. Deutsch, L. Genovese, Ph. Ghosez, M. Giantomassi, S. Goedecker, D.R. Hamann, P. Hermet, F. Jollet, G. Jomard, S. Leroux, M. Mancini, S. Mazevet, M. J. T. Oliveira, G. Onida, Y. Pouillon, T. Rangel, G.-M. Rignanese, D. Sangalli, R. Shaltaf, M. Torrent, M. J. Verstraete, G. Zerah, and J. W. Zwanziger. Abinit: First-principles approach to material and nanosystem properties. *Computer Physics Communications*, 180(12):2582, 2009.

[120] M. Fuchs and M. Scheffler. Ab initio pseudopotentials for electronic structure calculations of poly-atomic systems using density-functional theory. *Computer Physics Communications*, 119(1):67, 1999.

[121] F. Tran and P. Blaha. Accurate band gaps of semiconductors and insulators with a semilocal exchange-correlation potential. *Phys. Rev. Lett.*, 102:226401, 2009.

[122] A. D. Becke and E. R. Johnson. A simple effective potential for exchange. *The Journal of Chemical Physics*, 124(22):221101, 2006.

[123] Y. P. Varshni. Temperature dependence of the energy gap in semiconductors. *Physica*, 34(1):149, 1967.

[124] M. Cardona and R. K. Kremer. Temperature dependence of the electronic gaps of semiconductors. *Thin Solid Films*, 571:680, 2014.

[125] J.-M. Wagner and F. Bechstedt. Properties of strained wurtzite GaN and AlN: *Ab initio* studies. *Phys. Rev. B*, 66:115202, 2002.

[126] W. Shan, J. J. Song, Z. C. Feng, M. Schurman, and R. A. Stall. Pressure-dependent photoluminescence study of $In_xGa_{1-x}N$. *Applied Physics Letters*, 71(17):2433, 1997.

[127] C. Roder, S. Einfeldt, S. Figge, and D. Hommel. Temperature dependence of the thermal expansion of GaN. *Phys. Rev. B*, 72:085218, 2005.

[128] F. J. Manjn, M. A. Hernndez-Fenollosa, B. Mar, S. F. Li, C. D. Poweleit, A. Bell, J. Menndez, and M. Cardona. Effect of N isotopic mass on the photoluminescence and cathodoluminescence spectra of gallium nitride. *The European Physical Journal B - Condensed Matter and Complex Systems*, 40(4):453, 2004.

[129] I. Vurgaftman, J. R. Meyer, and L. R. Ram-Mohan. Band parameters for IIIV compound semiconductors and their alloys. *Journal of Applied Physics*, 89(11):5815, 2001.